

1N-02-TM

4609/

p.142

AN EXPERIMENTAL INVESTIGATION OF A SUPERSONIC
VORTICAL FLOW

By

Brian S. Levey

Bachelor of Science, 1989

Boston University

(NASA-TM-105102) AN EXPERIMENTAL
INVESTIGATION OF A SUPERSONIC VORTICAL FLOW
M.S. Thesis - George Washington Univ.
(NASA) 142 P

N91-32085

CSCD 01A

63/02 0046091
Unclas

A Thesis submitted to
the Faculty of

The School of Engineering and Applied Science
of The George Washington University

in partial satisfaction of the requirements
for the degree of Master of Science

September 1991

ABSTRACT

A considerable amount of research has been devoted to subsonic vortical flows; however, the current understanding of supersonic vortical flows is limited. Therefore, the objective of this work was to characterize the effect of adding swirl to a supersonic jet. The motivation for this investigation is the desire to enhance supersonic mixing in order to provide more efficient fuel injectors for supersonic combustion (scramjet) engines.

The vortical flow was created by tangential injection into a swirl chamber ahead of a converging-diverging nozzle. The amount of swirl was varied by changing the number of tangential injection holes and with the removal of the end piece, the jet could be run without swirl. The exit area to throat area ratio of the nozzle was 2 (nozzle exit was 1" in diameter), which provided a Mach 2.2 jet when run without swirl. The flow exited as a free jet into the laboratory.

Shadowgraphy, conventional schlieren, and focusing schlieren were used to obtain a qualitative understanding of the jet flow structure. The vertical and horizontal knife edge orientations were both used with the conventional and focusing schlieren systems. It was determined that an increase in swirl produced an increase in the shear layer growth. More quantitative results were obtained at a height of 5/16" above the nozzle exit using a five hole pressure probe, a static pressure probe, and a total temperature probe. The probes were calibrated in the no swirl case and the flow angles, pitot pressure, static pressure, and total temperature were measured directly. These data were employed to calculate various flowfield properties, such as Mach number, total pressure, and static density. The probe data were compared with theoretical calculations, which assumed steady state, isentropic, axisymmetric, quasi-one-dimensional (radial velocity is zero) flow in the nozzle and Rayleigh scattering from a laser light sheet results. The probe data compared favorably with the theoretical calculations, except in the viscous core where viscous effects were not considered negligible. These results verified that a supersonic vortical flow was being created with a maximum helix angle of 33°.

ACKNOWLEDGEMENT

There are many people to whom I owe thanks and gratitude. I would first like to thank Scott Kjelgaard for all of his assistance. I am indebted to Dr. G. Burton Northam, for his valuable guidance throughout my stay here at NASA LaRC. I would also like to thank Steve Jones, David Rhodes, Dr. Leonard Weinstein, and Nick Lagen for their help on various aspects. I am grateful to Clinton Reese and Reggie Rose for their help and support of "The SWIRLJET." There are many other people who have provided me with assistance and to them I am grateful.

I would like to thank my officemate, Dean Eklund, for all those thought provoking and intellectual discussions. I am also grateful to Scott Stouffer for all his late night advice.

I am indebted to my friends, who always listened to me complain about the bad times and reminded me of the good times. However, without the support of my parents, Sandy and Kurt, and brother, Kevin, this thesis would not have been possible. Thank you for having faith in me and it is to you, that I dedicate this thesis.

TABLE OF CONTENTS

	Page
ABSTRACT	ii
ACKNOWLEDGEMENT	iii
TABLE OF CONTENTS	iv
LIST OF FIGURES	vi
LIST OF TABLES	xii
LIST OF SYMBOLS	xiii
 Chapter	
1.0 INTRODUCTION	1
2.0 BACKGROUND	4
2.1 Vortical Flow Investigations	4
2.1.1 Low Axial Speed Compressible Vortices ...	4
2.1.2 High Axial Speed Compressible Vortices ..	6
3.0 VORTICAL FLOW APPARATUS	10
4.0 FLOW VISUALIZATION TECHNIQUES	12
4.1 Experimental Method	12
4.1.1 Shadowgraphy	12
4.1.2 Conventional Schlieren	14
4.1.3 Focusing Schlieren	15
4.2 Results	17
4.2.1 Matched Exit Pressure	18
4.2.2 Effect of Mismatched Exit Pressure	21
5.0 INTRUSIVE MEASUREMENT TECHNIQUES	24
5.1 Experimental Method	24
5.1.1 Five Hole Pressure Probe	24
5.1.2 Static Pressure Probe	26
5.1.3 Total Temperature Probe	28
5.1.4 Data Aquisition System	30
5.1.5 Data Analysis	31
5.2 Probe Calibrations and Check Out	33
5.2.1 Five Hole Pressure Probe	34

5.2.2	Static Pressure Probe	35
5.2.3	Total Temperature Probe	36
5.3	Results	36
5.3.1	Five Hole Pressure Probe	37
5.3.2	Static Pressure Probe	38
5.3.3	Total Temperature Probe	39
5.3.4	Derived Results	40
6.0	SUMMARY AND CONCLUSIONS	43
7.0	RECOMMENDATIONS	45
8.0	APPENDICES	47
A.	Theoretical Calculations	47
	REFERENCES	51
	FIGURES	56
	TABLES	141

LIST OF FIGURES

Figure	Page
1.1 Artist's Conception of Single-Stage-to-Orbit Vehicle .	56
1.2 Operating Range for Various Propulsion Alternatives ..	57
1.3 Airframe-Integrated Scramjet Model	58
3.1 Coordinate System for Vortical Flow Apparatus	59
3.2 Vortical Flow Apparatus	60
3.3 Nozzle Contour	61
3.4 Measured Pressures Compared with Theoretical Pressures	62
4.1 Rayleigh Scattering from a Laser Light Sheet System ..	63
4.2 a) Shadowgraphy System	64
b) Conventional Schlieren System	65
4.3 Focusing Schlieren System	
a) Complete View	66
b) Detailed View	67
4.4 Shadowgraphs for Overexpanded Condition	
a) Medium Swirl: $P_e = 10.7$ psia	68
b) High Swirl: $P_e = 9.9$ psia	68
4.5 Shadowgraphs for Matched Condition	
a) No Swirl: $P_e = 16.3$ psia	69
b) Medium Swirl: $P_e = 14.2$ psia	69
c) High Swirl: $P_e = 15.1$ psia	69
4.6 Shadowgraphs for Underexpanded Condition	
a) No Swirl: $P_e = 22.7$ psia	70
b) Medium Swirl: $P_e = 27.5$ psia	70
4.7 Conventional Schlieren with a Vertical Knife Edge for Overexpanded Condition	
a) Medium Swirl: $P_e = 10.4$ psia	71
b) High Swirl: $P_e = 9.6$ psia	71
4.8 Conventional Schlieren with a Vertical Knife Edge for Matched Condition	

a)	No Swirl: $P_e = 15.9$ psia	72
b)	Medium Swirl: $P_e = 14.3$ psia	72
c)	High Swirl: $P_e = 15.0$ psia	72
4.9	Conventional Schlieren with a Vertical Knife Edge for Underexpanded Condition	
a)	No Swirl: $P_e = 25.9$ psia	73
b)	Medium Swirl: $P_e = 25.9$ psia	73
4.10	Conventional Schlieren with a Horizontal Knife Edge for Overexpanded Condition	
a)	Medium Swirl: $P_e = 10.3$ psia	74
b)	High Swirl: $P_e = 9.8$ psia	74
4.11	Conventional Schlieren with a Horizontal Knife Edge for Matched Condition	
a)	No Swirl: $P_e = 16.6$ psia	75
b)	Medium Swirl: $P_e = 14.4$ psia	75
c)	High Swirl: $P_e = 14.8$ psia	75
4.12	Conventional Schlieren with a Horizontal Knife Edge for Underexpanded Condition	
a)	No Swirl: $P_e = 38.6$ psia	76
b)	Medium Swirl: $P_e = 27.2$ psia	76
4.13	Focusing Schlieren with a Vertical Knife Edge for Overexpanded Condition	
a)	Medium Swirl: $P_e = 9.9$ psia	77
b)	High Swirl: $P_e = 9.9$ psia	77
4.14	Focusing Schlieren with a Vertical Knife Edge for Matched Condition	
a)	No Swirl: $P_e = 14.7$ psia	78
b)	Medium Swirl: $P_e = 14.4$ psia	78
c)	High Swirl: $P_e = 14.7$ psia	78
4.15	Focusing Schlieren with a Vertical Knife Edge for Underexpanded Condition	
a)	No Swirl: $P_e = 38.1$ psia	79
b)	Medium Swirl: $P_e = 27.9$ psia	79

4.16	Focusing Schlieren with a Horizontal Knife Edge for Overexpanded Condition	
a)	Medium Swirl: $P_e = 9.5$ psia	80
b)	High Swirl: $P_e = 9.9$ psia	80
4.17	Focusing Schlieren with a Horizontal Knife Edge for Matched Condition	
a)	No Swirl: $P_e = 14.2$ psia	81
b)	Medium Swirl: $P_e = 14.4$ psia	81
c)	High Swirl: $P_e = 14.8$ psia	81
4.18	Focusing Schlieren with a Horizontal Knife Edge for Underexpanded Condition	
a)	No Swirl: $P_e = 38.1$ psia	82
b)	Medium Swirl: $P_e = 27.7$ psia	82
4.19	Focusing Schlieren with a Horizontal Knife Edge for Matched Condition at Low Swirl ($P_e = 15.1$ psia)	83
4.20	Rayleigh Scattering from a Laser Light Sheet Showing Condensation in the Shear Layer for Matched Condition	
a)	No Swirl: $P_e = 14.7$ psia	84
b)	Low Swirl: $P_e = 14.7$ psia	84
c)	High Swirl: $P_e = 14.7$ psia	84
4.21	Normalized Shear Layer Growth Rate as a Function of Calculated Convective Mach Number	85
4.22	Shear Layer Growth Rate as a Function of Helix Angle Extrapolated to the Edge of the Jet	86
4.23	Hypothetical Flow Model of Vortex Breakdown at Supersonic Speeds	87
5.1	Illustration of Five Hole Pressure Probe	
a)	Side View of Tip	88
b)	Top View of Tip	89
5.2	Illustration of Static Pressure Probe	90
5.3	Illustration of Total Temperature Probe	91
5.4	Block Diagram of Data Aquisition System	92

5.5	Photograph of Vortical Flow Apparatus with Probe	93
5.6	P_j/P_o as a Function of Yaw Angle at $r = 0$ for No Swirl	94
5.7	Static Pressure as a Function of Yaw Angle at $r = 0$ for No Swirl	95
5.8	Total Temperature as a Function of Yaw Angle at Various Radial Distances for No Swirl	96
5.9	Helix Angle as a Function of Radial Distance for No Swirl	97
5.10	Helix Angle as a Function of Radial Distance for Low Swirl	98
5.11	Helix Angle as a Function of Radial Distance for Medium Swirl	99
5.12	Helix Angle as a Function of Radial Distance for High Swirl	100
5.13	Radial Angle as a Function of Radial Distance for No Swirl	101
5.14	Radial Angle as a Function of Radial Distance for Low Swirl	102
5.15	Radial Angle as a Function of Radial Distance for Medium Swirl	103
5.16	Radial Angle as a Function of Radial Distance for High Swirl	104
5.17	Pitot Pressure as a Function of Radial Distance for No Swirl	105
5.18	Pitot Pressure as a Function of Radial Distance for Low Swirl	106
5.19	Pitot Pressure as a Function of Radial Distance for Medium Swirl	107
5.20	Pitot Pressure as a Function of Radial Distance for High Swirl	108
5.21	Static Pressure as a Function of Radial Distance for No Swirl	109

5.22	Static Pressure as a Function of Radial Distance for Low Swirl	110
5.23	Static Pressure as a Function of Radial Distance for Medium Swirl	111
5.24	Static Pressure as a Function of Radial Distance for High Swirl	112
5.25	Total Temperature as a Function of Radial Distance for No Swirl	113
5.26	Total Temperature as a Function of Radial Distance for Low Swirl	114
5.27	Total Temperature as a Function of Radial Distance for Medium Swirl	115
5.28	Total Temperature as a Function of Radial Distance for High Swirl	116
5.29	Mach Number as a Function of Radial Distance for No Swirl	117
5.30	Mach Number as a Function of Radial Distance for Low Swirl	118
5.31	Mach Number as a Function of Radial Distance for Medium Swirl	119
5.32	Mach Number as a Function of Radial Distance for High Swirl	120
5.33	Total Pressure as a Function of Radial Distance for No Swirl	121
5.34	Total Pressure as a Function of Radial Distance for Low Swirl	122
5.35	Total Pressure as a Function of Radial Distance for Medium Swirl	123
5.36	Total Pressure as a Function of Radial Distance for High Swirl	124
5.37	Axial Velocity as a Function of Radial Distance for No Swirl	125

5.38	Axial Velocity as a Function of Radial Distance for Low Swirl	126
5.39	Axial Velocity as a Function of Radial Distance for Medium Swirl	127
5.40	Axial Velocity as a Function of Radial Distance for High Swirl	128
5.41	Tangential Velocity as a Function of Radial Distance for Low Swirl	129
5.42	Tangential Velocity as a Function of Radial Distance for Medium Swirl	130
5.43	Tangential Velocity as a Function of Radial Distance for High Swirl	131
5.44	Static Temperature as a Function of Radial Distance for No Swirl	132
5.45	Static Temperature as a Function of Radial Distance for Low Swirl	133
5.46	Static Temperature as a Function of Radial Distance for Medium Swirl	134
5.47	Static Temperature as a Function of Radial Distance for High Swirl	135
5.48	Static Density as a Function of Radial Distance for No Swirl	136
5.49	Static Density as a Function of Radial Distance for Low Swirl	137
5.50	Static Density as a Function of Radial Distance for Medium Swirl	138
5.51	Static Density as a Function of Radial Distance for High Swirl	139
A.1	Calculated Vortex Streamtube Diameter as a Function of Axial Velocity	140

LIST OF TABLES

Table		Page
3.1	Geometric and Calculated Flow Parameters of the Nozzle for the Investigated Swirl Cases	141
5.1	Average Total Property Values at the Plenum Chamber ..	142

LIST OF SYMBOLS

a	speed of sound, $= \sqrt{\gamma RT}$, (ft/s)
A	clear aperture of focusing lens, (in)
A ₃	distance above knife edge to edge of focusing lens in conventional schlieren, (in)
A _n	tangential injection area, (in ²)
b	cutoff image slit height in focusing schlieren, (in)
C _p	constant pressure specific heat, (ft ² /(s ² °R))
d	nozzle diameter, (in)
DS	depth of sharp focus, (in)
DU	depth of unsharp focus, (in)
h	light source image height above cutoff, (in)
l	distance from flowfield object to mirror or lens, (in)
l'	distance from mirror or lens to final image location, (in)
L	distance from source grid to lens in focusing schlieren, (in)
L'	distance from mirror or lens to cutoff location, (in)
m	magnification of image, $= \frac{l'}{l}$
m _f	mass flow rate, (slug/s ²)
M	Mach number
M _c	convective Mach number
P	pressure, (lbs/in ²)
r	distance in radial direction, (in)
r'	recovery factor
R	specific gas constant, (ft ² /(s ² °R))
R'	$= \frac{1}{A}$
T	temperature, (°R)
x	distance in axial direction, (in)
U	velocity in axial direction, (ft/s)
U _c	convective velocity, (ft/s)
V	velocity in tangential direction, (ft/s)

w	diffraction limited resolution referred to flowfield for focusing schlieren, (in)
w'	diffraction limited resolution referred to flowfield for conventional schlieren, (in)
y	coordinate axis in radial direction on five hole pressure probe
z	coordinate axis in tangential direction on five hole pressure probe

Greek Symbols

γ	ratio of specific heats
δ	shear layer visual thickness, (in)
ϵ_{\min}	angle change causing 10% brightness change in image for focusing schlieren, (arcsec)
ϵ'_{\min}	angle change causing 10% brightness change in image for conventional schlieren, (arcsec)
η	$= \frac{r}{r^*}$
θ	yaw or helix angle, (degrees)
λ	wavelength of light, (in)
ρ	density, (slug/ft ³)
ϕ	radial angle, (degrees)
Φ	non-dimensional mass flow rate

Subscripts

1-5	holes on five hole pressure probe
a	theoretical
c	streamtube where $M \rightarrow \infty$
e	exit
h	high-speed stream

i	incompressible properties
j	five hole pressure probe holes, 1-5
l	low-speed stream
n	tangential injection holes
o	total properties at plenum chamber
o1	local total properties
o2	total properties behind the normal shock
s1	station #1
t	throat
x	axial component
w	nozzle wall
θ	tangential component

Superscripts

*	sonic conditions
---	------------------

1.0 INTRODUCTION

Even though man has conquered the perils of flight, he continues to push its limitations. Today, he desires to fly faster, farther, and higher than ever before. Currently, this goal is the motivation behind the National Aero-Space Plane (NASP), designated the X-30. This single-stage-to-orbit (SSTO) aircraft would be capable of cruising for substantial periods of time at hypersonic speeds (Mach number greater than 5) and horizontal take-offs and landings. The current design calls for the vehicle to be hydrogen fueled.¹ An artist's conception of this aircraft is shown in figure 1.1.

The development of the X-30 is restricted by a variety of parameters, such as the availability of various materials and fuels, structural concerns, and aerodynamic considerations. However, the Hypersonic Propulsion and Experimental Methods Branches at NASA's Langley Research Center (LaRC) are primarily concerned with the propulsion element. Turbojets and rockets are two types of propulsion systems used in today's vehicles. It is believed though, that the X-30 will employ a supersonic combustion (scramjet) ramjet as its propulsion system. As early as 1960, engineers realized that the scramjet would be a possible propulsion system for a hypersonic vehicle, which is easily understood by considering figure 1.2.² Up to speeds of about Mach 3, the turbojet is the most efficient system. In the Mach 2 to 6 range, a hydrogen-powered ramjet will operate satisfactorily. However at higher flight Mach numbers, if the engine's internal flow speed is reduced to the subsonic regime, large losses in total pressure will occur and there would also be an accompanying increase in the static pressure. Therefore, a scramjet will provide lower static pressures and temperatures, which are beneficial from a thermal and structural standpoint.

In the mid 1960's, NASA began the Hypersonics Research Engine Project (HRE). Its main objective was to examine the scramjet and determine if it was a viable method of propulsion for a manned vehicle. This scramjet was

to be tested on the X-15 research airplane. However since the X-15 project was cancelled in 1968, the HRE never reached the flight test stage.^{3,4}

As a result of HRE and recent progress, the X-30 features an airframe-integrated scramjet, shown in figure 1.3. This concept allows for the scramjet to capture all of the compressed air behind the bow shock, which forms at the nose of the aircraft. This is necessary to obtain the required thrust at higher flight Mach numbers. In this case, the aft surface can be used as a nozzle for the expansion and the forebody for the inlet compression.⁴

Due to its high energy content and ability to absorb large amounts of heat per unit mass of fuel from the engine and airframe, hydrogen is the fuel being considered for the X-30. Large fuel tanks would be required, since hydrogen has such a low density. Therefore, it has been proposed that slush hydrogen, 50% solid and 50% liquid, be used.⁵ In scramjets operating at high Mach numbers, the energy content of the fuel recovered from the cooling of the aircraft is a large fraction of the net thrust. To obtain the maximum thrust, it is desired to use parallel fuel injection.⁶ However, at high speeds the mixing between coflowing jets, air and hydrogen in this case, has been shown to be poor.⁷ For this reason, there is a desire to both control and enhance mixing for scramjet combustion.

One method of mixing enhancement under investigation for wall-mounted parallel injection involves the use of swept and unswept ramps.⁸ The trailing edges of the swept ramp configuration generated a higher degree of vorticity and entrainment, which produced an increase in mixing. It has also been proposed that the mixing between the hydrogen jet and coflowing supersonic air could be increased by introduction of a swirling component into the hydrogen jet. This theory was first proposed by Swithenbank and Chigier,⁹ who realized that the added kinetic energy provided by the tangential velocity component might increase the turbulent intensity of the swirling jet in the downstream direction. During this study, they also outlined the characteristics of what is now known as vortex breakdown. They reasoned that a region of reverse axial flow along the axis of the vortex could be formed by the axial and radial pressure gradients that

resulted from the tangential velocity component. Subsonic vortical flows and their associated phenomenon, such as breakdown, are better understood as compared with the supersonic regime.¹⁰ However, what little data is available on supersonic vortical mixing flows is inconclusive at this point.^{11,12}

Therefore, a basic and fundamental understanding of supersonic vortical flows is needed. For this reason, a supersonic vortical flow apparatus has been constructed. Tangential injection was used to create the vortical flow. The apparatus was designed, such that the swirl strength could be varied and the flow examined in a supersonic jet with an exit area to throat area ratio of 2. Since this investigation was a basic fluid mechanics study, air was used as the working fluid.

Various flow visualization techniques, such as shadowgraphy, conventional schlieren, and focusing schlieren were used to examine the supersonic jet. Results are shown for the overexpanded, matched, and underexpanded conditions of the various swirl cases. These tests produced results that were primarily qualitative. Therefore, miniature probes were used to obtain quantitative results which could be compared with theoretical calculations and Rayleigh scattering from a laser light sheet.¹³ A movable five hole pressure probe, static pressure probe, and total temperature probe were used to obtain data for the matched exit condition. These data were employed to calculate other valuable flowfield properties, such as Mach number, total pressure, and static density.

2.0 BACKGROUND

2.1 Vortical Flow Investigations

The following discussion is limited to compressible vortical flows. This does include vortical flows with low axial velocity, such as those which occur in Ranque-Hilsch tubes. Longitudinal vortices with a high axial velocity, such as those found in supersonic wind tunnels and jets, are also reviewed. A variety of authors, such as Leibovich¹⁰, have reviewed low speed vortical flows and vortex breakdown.

2.1.1 Low Axial Speed Compressible Vortices

In 1933 Ranque¹⁴ created a subsonic vortical flow in a 0.47" diameter cylinder. This vortical flow was produced by permitting compressed air to enter the cylinder through a tangential nozzle. A turbulent rotating flow exited through both ends of the cylinder. A diaphragm at one end permitted only air from the inner region to escape through the diaphragm, while at the other end of the cylinder the tube was throttled, permitting only the outer region of the vortex to escape. This vortical flow had higher pressure and temperature values at its outer region (throttled end) and lower values at the inner region (diaphragm end). The highest obtained temperature difference was 158°F for 6 psig compressed air at 68°F. The lowest measured inner region temperature was 10°F.

Then in 1946, Hilsch¹⁵ constructed a vortex tube for the purpose of obtaining a cooling process of maximum efficiency. Hilsch was able to show that by varying the temperature, pressure, and flow rate of the compressed air, the temperature of the inner and outer regions of the vortex could also be varied.

At the University of Minnesota, Hartnett and Eckert¹⁶ expanded on Ranque and Hilsch's ideas and designed a vortex that was large enough so that the intrusion of probes would not disturb the flow. The vortex had a radius of 1.5". The majority of the data were obtained outside a radius of

0.5", since inside this region ($r < 0.5$ ") the probe caused erratic results. The cold end (diaphragm end) of the vortex tube was closed during their entire investigation. The study included taking measurements at various radial and axial positions. They determined that the flow angles were not affected by inlet pressure changes. The velocity and total temperature measurements were largest at the outer region. The minimum total temperature measurements occurred at the center of the flow and the minimum velocity measurements were located at a radial distance of 0.25" (no data were obtained inside $r < 0.25$ "). Reverse axial flow was indicated in the vicinity of a 0.75" radius. They compared the energy separation of the vortex with a boundary layer and determined that the vortex flow value was significantly larger. For an inlet pressure of 20 psig and a maximum velocity of 800 ft/s, the total temperature difference in the vortex was 80°F. However, for a flow at 800 ft/s over a flat plate, the total temperature difference was 11°F for the laminar boundary layer and 7°F for the turbulent boundary layer.

Lay¹⁷ in the late 1950's, undertook an experimental and analytical study of compressible flow in a vortex tube. The cold end of his 2" diameter vortex tube was also closed for the entire investigation. Lay's objective was to obtain a basic understanding of the pressure, temperature, and velocity distributions of the vortex. A key difference in this study was that the vortex tube was made out of Lucite for the explicit purpose of obtaining flow visualization results. However, the smoke flow visualization was good only at low speeds. Lay verified and obtained many results key to the understanding of vortical flows. The flow angle was found to be independent of the inlet pressure. Tangential velocities were found to be large and the maximum was located towards the center of the vortex. When compared with tangential velocities, the axial velocities were considered small and concentrated near the wall in a small annular region. Magnitudes of the velocity vector as high as 900 ft/s were obtained. Towards the center of the vortex, the velocity results indicated a region of reverse axial flow.

Also in the late 1950's, Savino and Ragsdale¹⁸ designed two vortex chambers. The uniqueness of their experiment was that the vortical flow was accomplished by the use of swirl vanes. One of the vortex generators created a compressible vortical flow. This generator operated at atmospheric pressure in the inlet chamber and exited into a vacuum. The results showed an axial variation in the total temperature; however, the primary variation was in the radial direction. Therefore, these results showed that the energy separation was either diminished or unaffected by the confined axial flow channels and that the energy separation resulted from and occurred in the initial portion of the vortex. This realization meant that the temperature separation found in a confined vortex could be created without the Ranque-Hilsch method.

Mandella and Bershader¹⁹ studied a compressible vortex and its interaction with airfoils. The purpose of this experiment was to understand the aerodynamics of rotary-wing aircraft at high angles of attack. An understanding of the generation and structure of the vortex interaction was obtained by the method of pulsed holographic interferometry. The vortex generator was a NACA 0018 airfoil at a 30° angle of attack. The velocity of the vortex was held constant at 590 ft/s. The static radial pressure distribution showed a sharp drop, up to a factor of 3, at the center of the vortex. The static density also exhibited this same trend. However by use of the perfect gas law, the static temperature variations were shown to be smaller than the static pressure and density variations. The static density of the inner region was found to increase at downstream axial locations and was accompanied by a moderate increase in spreading.

A detailed bibliography of the work done on the vortex tube from 1931 to 1953 is given by Westley.²⁰

2.1 High Axial Speed Compressible Vortices

Gostintsev, et al.,²¹ studied underexpanded supersonic jets exiting from a sonic (convergent only) nozzle. The swirl was created by use of a swirl generator, similar to a centrifugal injector with a tangential inlet,

immediately ahead of the nozzle. They were able to verify that the rotation effect on the shock structure of the jet was similar to the effect of a reduction in the overpressure ratio. The shock structure of a jet is governed by the difference between the pressure at the exit of the jet and the pressure of the surrounding region. If this difference is small, then a limited shock wave is formed. An increase in the jet pressure causes the shock wave to intersect the flow axis. If the jet pressure is again increased, an X-shaped shock formed. Another increase in pressure causes a disk-like compression shock to form perpendicular to the jet axis.

Their results showed that if the stagnation pressure was held constant and the swirl magnitude was increased, the following occurred. At low swirl rates, the straight jet configuration was maintained with the disk-shaped shock moving closer to the nozzle. An increase in the swirl rate caused a further weakening of the disk-shaped shock and a X-shaped shock appeared as regular reflection. This X-shaped shock degenerated into a weak shock wave of limited extent at the edge of the jet. Finally, they verified the existence of a region of reverse axial flow with a velocity of up to 328 ft/s. This observation was accomplished by taking photographs of the motion of a luminous plasma filament created by breakdown between needles of a spark gap.

At Virginia Polytechnic Institute and State University's Gas Dynamics Laboratory, Swanson and Schetz¹¹ examined the effects of swirl on the mixing of a jet injected into a parallel stream. The injectant was at subsonic speeds and the freestream Mach number was 3.5. The swirling flow was created using tangential injection and it represented 50% of the injectant mass flow. The other 50% of the injectant mass flow was straight (nonswirling) flow. In order to prove that swirl was being produced by tangential injection, helium was used as an injectant. Tests were then run with no external flow for both the swirl and no swirl cases. The spread angle of the jet for the swirl case showed an increase, so it was decided that swirl was being produced.

The total pressure and Mach number distributions for various axial locations all showed Gaussian distributions. Schetz and Swanson argued

that the total temperature was constant throughout the entire jet, by placing the total temperature probe at the axial station $x = 10d$ on the centerline and determining that the total temperature at this location was the same as the settling chamber total temperature.

The schlieren photographs and the pitot pressure distributions showed little change between the straight and swirling jets. Therefore, they decided that swirl was ineffective as a mixing aid. However, the jet velocity profiles at the point of injection were not measured, and the helix angles may not have been very large. Also, the swirling flow had a low axial Mach number, when compared with the freestream Mach number of 3.5.

Délery, et al.,²² studied and compared subsonic and supersonic vortices. A high axial speed compressible vortex was created by using a wing with a swept leading edge. The angle of attack could be varied, which would change the vortex strength. The wing was placed in front of a converging-diverging nozzle. Therefore, a vortex was created and then accelerated through the nozzle. For various freestream Mach numbers, nearly axisymmetric vortices were obtained. Using the ratio of the maximum tangential velocity and the axial velocity on the outer edge of the vortex, the helix angle was calculated. A maximum helix angle of 20° was obtained with an upstream Mach number of 1.75 compared with 13° for an upstream Mach number of 2.28.

The interaction of the high axial speed compressible vortices with a shock was also examined. It was determined that vortex breakdown could be induced by the shock. A five hole pressure probe and Laser Doppler Velocimetry (LDV) were used to examine the flow. The theoretical inviscid calculations, which were used to predict breakdown, compared favorably with the experimental results.

An investigation examining the structure and effect of supersonic vortices is on-going at The Pennsylvania State University.^{12,23} In their first test,²³ the wind tunnel and vortex generator were both run at Mach 3. The swirl was obtained by use of guide vanes. They used a variety of intrusive and nonintrusive techniques to characterize the interaction. The

tangential Mach number results showed a well defined vortex with a distinct core. The static and total pressure decreased at the core of the vortex.

Metwally, Settles, and Horstman¹² continued the research to include a vortex of Mach numbers 2.2, 3.0, and 3.5 injected into a Mach 2.0 flow. They found that as the swirl rate was increased, changes in the structure of the flow were noticeable. For the case of a Mach number of 3.0 and 93° guide vanes, a vortex with a maximum helix angle of 15° was created. The interaction between the vortex and a shock produced changes in the static pressure, tangential Mach number, and axial Mach number of the vortex. After the interaction, all measured core values were approximately equal to their respective freestream values. Finally, the experimental results were compared with computational data and showed that improvements were needed in the computational method.

The current investigation was an extension on the results presented by Cutler and Levey.¹³ In their study, the supersonic jet was primarily visualized using Rayleigh scattering from a laser light sheet. Their results suggested that the vortical flow apparatus was functioning as designed. Results were also presented, which showed an increase in the shear layer growth with an increase in swirl. The presence of vortex breakdown was suggested for the high swirl case at the overexpanded condition, because on the vortical flow axis condensation penetrated upstream towards the jet exit.

As previously noted, there are a variety of ways to create a vortical flow. The current desire to enhance mixing has accelerated the need to understand all types of compressible vortical flows. Therefore, even though other studies are already underway that examine high axial speed compressible vortical flows,²³ this investigation was initiated. It is believed that the method used in this investigation, tangential injection ahead of a converging-diverging nozzle, would be superior in creating supersonic vortex flows with high helix angles when compared with other methods, such as guide vanes and delta wings.

3.0 VORTICAL FLOW APPARATUS

A supersonic vortical flow can be created in a variety of ways. One technique is to place guide vanes in a converging-diverging nozzle. This method was not used, because if the guide vanes were placed in the supersonic region of the nozzle, they would produce a complex shock structure and high flow angles would be difficult to obtain if the guide vanes were placed in the subsonic region of the nozzle. Therefore, this investigation used tangential injection into a chamber ahead of a converging-diverging nozzle to create a high axial speed compressible vortical flow. This method was used by Escudier, Bornstein, and Zehnder²⁴ in their study of vortex breakdown at low speeds.

The design of the vortical flow apparatus was not part of this thesis; however, a description of the calculations that were used in the design of this apparatus is given in Appendix A. A description of the vortical flow apparatus is provided below.

The coordinate system of the vortical flow apparatus is shown in figure 3.1. The vortical flow apparatus and nozzle contour are illustrated in figures 3.2 and 3.3, respectively. Table 3.1 has the geometric and calculated flow parameters for all the test cases. The vortical flow apparatus was placed on the plenum chamber, which was part of an already existing facility in building 1221C at NASA LaRC. The plenum chamber was attached to a large air tank which could be pressurized to 600 psia. The total pressure of the plenum chamber was controlled by a valve on the airline between the plenum chamber and the 600 psia air tank and by varying the air tank pressure. The air was injected at low speeds ($M < 0.2$) from the plenum chamber into the swirl chamber through the exposed tangentially drilled holes. Thus, a subsonic vortical flow was created and then accelerated through the converging-diverging nozzle. The flow exited as a free jet into the laboratory. The run time with this configuration was unlimited, since the air tank could be filled as fast as the flow to the jet emptied it.

The number of exposed injection holes was varied by changing the inserts of the swirl chamber. An increase in the tangential velocity of injection occurred when the number of exposed injection holes was decreased. This resulted in an increase in vortex circulation. The apparatus could be run without swirl, if there was no insert in the swirl chamber.

The nozzle was designed with an exit area to throat area ratio of 2. It is important to note that the diameter of the nozzle exit was only 1.0". This was a factor in the design of the focusing schlieren system and miniature probes. According to isentropic, quasi-one-dimensional flow theory, a Mach number of 2.2 in the axial direction would be obtained in the no swirl case. The apparatus had four pressure taps that were located at the exit and throat of the nozzle, in the swirl chamber (1.75" from the axis), and in the plenum chamber. To verify that the apparatus was functioning as designed, measurements at the pressure taps were compared with the theoretical calculations and are shown in figure 3.4. The theoretical calculations are explained in Appendix A and the experimental techniques are described in Section 5.1.4. Based on the favorable comparison, it was concluded that the apparatus was functioning properly.

4.0 FLOW VISUALIZATION TECHNIQUES

The most common and simplest way to investigate a complex flowfield is to employ one of the many flow visualization techniques. Shadowgraphy, conventional schlieren, and focusing schlieren were used in this investigation. The vertical and horizontal knife edge orientations were both used with the conventional and focusing schlieren systems. These methods provided primarily qualitative results.

4.1 Experimental Method

Rayleigh scattering from a laser light sheet was used by Cutler and Levey¹³ to obtain qualitative and quantitative results. The system used in their investigation is illustrated in figure 4.1. Rayleigh scattering is the elastic scattering of light off of molecules. During their investigation condensation formed in the shear layer, due to the mixing of the cold dry jet air with the warm damp ambient air. In order to obtain static density measurements, the nozzle was modified and a concentric nozzle, which provided a low speed coflowing jet, was added. Condensation was therefore absent from the shear layer until approximately 1" from the nozzle exit. The results from Cutler and Levey¹³ are used for comparison with the results obtained in this investigation.

A brief historical overview of shadowgraphy, conventional schlieren, and focusing schlieren is given below. Each overview is followed by a detailed description of the experimental set up used in this investigation.

4.1.1 Shadowgraphy

Shadowgraphy is one of the oldest and simplest flow visualization techniques. It was first discovered in 1880 by Dvorak. Shadowgraphy can be seen in a variety of day-to-day observations. For instance, dark lines and bands appear with the shadow of a window on a sunny day. However, if

the window is opened the bands disappear. These lines and bands make-up a shadowgraph and are due to the heterogeneities in the window.²⁵

This can easily be reproduced in a laboratory experiment. As light passes through a medium of varying density, it is deflected in proportion to the density gradient. If the density gradient is constant, the light intensity at the film will be constant, because all of the light rays will be deflected the same distance. However, if the density gradient is not constant, the light intensity at the film will vary due to the variation in the deflection of the light rays. If the density gradient is decreasing, the light rays will converge and cause an increase in illumination at the corresponding location on the film. Whereas if the density gradient is increasing, the light rays will diverge and cause a decrease in illumination at the corresponding location on the film.

Shadowgraphy is an excellent way to observe general trends of a flow. However, there are a few shortcomings with this technique. Quantitative measurements of density are rarely obtainable. Since shadowgraphy shows the double derivative of density, it is likely error would be obtained in executing the double integral. Shadowgraphy also suppresses the finer details of the flow, because the image of the flow is defocussed as a consequence of the deflections of the light rays. This is a brief description of shadowgraphy and more information is available in a variety of references.²⁵⁻³⁰

The shadowgraphy system used for this experiment is shown in figure 4.2a. This particular set up was chosen due to the proximity of the jet to the wall and other laboratory equipment. The light source was an air gap spark with a 1 mm source. Both mirrors used in this system had a 6" diameter and 48" focal length. A Hasselblad 500 EL camera with a 17.5" focal length was used to capture the image. Kodak 70 mm Tri-X film which came in 15 ft rolls was used. A 4.25" by 3" field of view was available with this arrangement.

4.1.2 Conventional Schlieren

Schliere is a German word which refers to a local inhomogeneity in a transparent medium, which causes an irregular light deflection. Therefore, a conventional schlieren system intercepts deflected light, and produces an image which has lighter and darker points. This set up was first discovered by Foucault (1859) and Toepler (1864).

The set up is similar to shadowgraphy. Light, collected in a parallel beam, is directed towards and passes through the test section. The light source should be a point source or a narrow slit parallel to the knife edge. The parallel light is then focused onto a screen. Where the density varies in the test section, the parallel light rays will be deflected and not pass through the focal point. At the focal point, a knife edge is placed to eliminate the deflected light rays. Without the deflected rays, the obtained image has a variation in illumination that is proportional to the deflection and consequently the density gradients.

The major qualities of a conventional schlieren system are the sensitivity and resolution. The sensitivity is defined as the angle change causing a 10% change in the image brightness and is given by³¹:

$$\epsilon'_{\min} = \frac{20,626h}{L'} \text{ arcsec} \quad (4.1)$$

The resolution for a conventional schlieren system is defined as the distance, which must separate two points in order to make them distinguishable and is limited by the aperture diffraction of the focusing lens.

Therefore, the resolution is given by³¹:

$$w' = \frac{1.22(l' - L')\lambda}{m\lambda_3} \quad (4.2)$$

The resolution can also be affected by other factors, such as the film quality.

It is possible to obtain the density gradient in any direction by properly rotating the source and knife edge. It is most common to obtain the density gradients that are parallel and normal to the flow. A more

detailed description of the conventional schlieren technique has been given by a variety of authors.²⁵⁻³¹

The conventional schlieren system used in the current investigation was identical to the shadowgraphy system except for the knife edge. The knife edge was 6" in front of the camera lens as shown in figure 4.2b. The primary characteristics of this set up were the sensitivity, resolution, and field of view. The sensitivity was 8 arcsec and the resolution was 0.006". The maximum obtainable image was the same as the shadowgraphy system, 4.25" by 3". The knife edge was used to obtain density gradients both normal (vertical) and parallel (horizontal) to the flow.

4.1.3 Focusing Schlieren

Weinstein³¹ has recently rediscovered the focusing schlieren system. A better understanding of focusing schlieren can be obtained by examining single and multiple images. The field of view is small and the beam is not collimated if light comes from one point at the source. However, if a closely spaced planar distribution of source points is used, each point in the flowfield will be illuminated by light from the several source points. Multiple overlapping images, one for each source point, will construct the final image. One focus position exists for each flowfield distance which will cause the flow features to be focused at the image plane. Changing the image plane location causes different regions of the flowfield to be focused.

The three main qualities of a focusing schlieren system are sensitivity, resolution, and depth of focus. The sensitivity is defined in Section 4.1.2, but for a focusing schlieren system it is given by³¹:

$$\epsilon_{\min} = \frac{20,626hL}{L'(L-1)} \text{ arcsec} \quad (4.3)$$

The resolution is defined in Section 4.1.2 and for a focusing schlieren it is limited by the diffraction of the cutoff grid. Therefore, the resolution is given by³¹:

$$w = \frac{2(l' - L')\lambda}{mb} \quad (4.4)$$

The resolution can also be affected by the imaging lens and quality of the film. The angle subtended by the effective aperture to the flowfield is the governing factor for the depth of focus. The difference in the depth of focus between focusing and conventional schlieren is in the definition of the effective aperture. For conventional schlieren the effective aperture is defined as the image of the source; whereas, for focusing schlieren it is defined as the imaging lens aperture. A depth of sharp focus is defined as the depth at which the resolution of the optical set up and film is exceeded by the loss of resolution due to being out of focus. A depth of sharp focus is consequently given by³¹:

$$DS = 2R'w \quad (4.5)$$

A depth of unsharp focus is defined as the depth at which a selected threshold (smallest desired detail in flowfield) is exceeded by the loss of resolution due to being out of focus. Since 0.079" was chosen as the effective size for unsharp features, the depth of unsharp focus is given by³¹:

$$DU = (0.157R')'' \quad (4.6)$$

Once the characteristics of the focusing schlieren system have been decided upon, the proper equipment needs to be chosen. Trade-offs are necessary between such characteristics as: sensitivity, resolution, depth of focus, and field of view. The lens is chosen, such that it provides the desired characteristics of the focusing schlieren system. The cutoff grid selection is a little more difficult. The cutoff grid has to meet three requirements: sufficient sensitivity to examine desired flows, produce a smooth image, and provide sufficient resolution. In addition, fine adjustments in focus and cutoff have to be made, so the receiving optical components have to be adjustable.

The small depth of focus desired was the limiting quality in choosing the components for the current focusing schlieren system. Since the jet

diameter was only 1", a narrow depth of focus was needed to make this technique useful. If the depth of focus is not small enough, there will be little distinction between the conventional and focusing schlieren results.

A variety of set ups were tried; however, the desired results were not obtained until the system shown in figure 4.3 was used. The Quantel YG 581 (frequency doubled and Q-Switched Nd-Yag) laser was chosen as the light source. The pulses were short (10 ns) green pulses. The energy of a pulse was attenuated to 5 mJ to give a good exposure. The diffuser and Fresnel lens #1 (8.5" focal length) were chosen so that the proper amount of light was directed over the field of view. A source grid was made with clear lines 0.025" wide and dark lines 0.075" wide. A video projection lens (18" focal length with 4.5" clear aperture) was used in this set up. Fresnel lens #2 (8.2" focal length) was located beyond the direct image and was used to refocus the light reaching the direct image. This combination served as a reducing relay system. An 80 mm f/2.8 lens with a +4 close-up lens on a Hasselblad camera was used to capture the image. Kodak Tri-X 70 mm film on 15 ft rolls was used.

The sensitivity for the focusing schlieren system was 16 arcsec, which was double the angle for conventional schlieren system. This value was selected to give a larger dynamic range than the conventional schlieren system. The resolution was 0.003". The depth of sharp focus was 0.04" and the depth of unsharp focus was approximately 1", which was the minimum usable depth for the current test. This set up produced a field of view of 3" by 3". The focusing schlieren system was able to meet the requirement, such that the depth of focus was smaller than the diameter of the jet, so as to show interior details.

4.2 Results

Shadowgraphy, conventional schlieren, and focusing schlieren results are presented in figures 4.4-4.18. The results are presented by the flow visualization technique and exit condition. For example, the shadowgraphs for the matched condition of the various swirl cases are shown in figure

4.5. Only the no, medium, and high swirl cases (refer to table 3.1) are presented. These results show the trends of the flow and the presentation of other swirl cases would not add to the discussion.

4.2.1 Matched Exit Pressure

The effect of swirl on the mixing of a supersonic jet is best shown by examining the growth rate of the shear layer for the matched exit pressure condition. The growth and structure of turbulent shear layers has been examined recently.^{32,33} Results have shown that the spreading of a turbulent shear layer between a supersonic stream and a stream at rest is less than in the incompressible case. It has also been shown that with an increasing freestream Mach number, the spreading rate decreases. It is believed that by adding swirl to the flow, the growth rate of the shear layer will increase.

Papamoschou and Roshko³² collapsed a substantial body of data for the spreading rate of a shear layer between streams of different speed, density, γ , etc. by graphing the normalized shear layer growth rate as a function of the convective Mach number. The normalized shear layer growth rate is defined as the compressible shear layer growth rate divided by the incompressible shear layer growth rate. The convective Mach number is defined as the Mach number in a frame of reference convecting with the velocity U_c , which is assumed to be constant.

Images from focusing schlieren with a horizontal knife edge and Rayleigh scattering from a laser light sheet were used to obtain the compressible shear layer growth rate, $\frac{d\delta}{dx}$. The images from focusing schlieren with a horizontal knife edge are shown in figures 4.17 and 4.19. The Rayleigh scattering images from a laser light sheet are shown in figure 4.20 and a detailed discussion of this technique is given by Cutler and Levey.¹³ The Rayleigh scattering images show laser light sheet scattering from the submicron ice particles or clusters, which formed due to the mixing of the warm damp ambient air and the cold dry jet air in the shear

layer. The shear layer growth rate was obtained for the no swirl case by drawing straight lines tangent to the edge of the shear layer, whose growth was expected to be linear, and measuring the growth of the shear layer width. This was done from a height of 0.5" above the nozzle exit to an area where the shear layer was still visible. This resulted in a measurement region of about 2" for the focusing schlieren with a horizontal knife edge and about 1.25" for the Rayleigh scattering from a laser light sheet. The two shear layers, one on each side of the jet, were both measured and an average value was calculated. So, $\frac{d\delta}{dx} = 0.06$ for the focusing schlieren with a horizontal knife edge and $\frac{d\delta}{dx} = 0.08$ for Rayleigh scattering from a laser light sheet. An uncertainty of $\pm 33\%$ was estimated for these values due to the ambiguity in drawing the tangent lines. The incompressible shear layer growth rate was calculated using the formula provided by Papamoschou and Roshko³² and the simplification that $U_1 = 0$ for this investigation:

$$\left(\frac{d\delta}{dx}\right)_i = 0.17 \left[1 + \sqrt{\frac{\rho_1}{\rho_h}} \right] \quad (4.7)$$

Therefore, for this investigation $\left(\frac{d\delta}{dx}\right)_i = 0.29$. This gives a normalized shear layer growth rate of 0.20 for focusing schlieren with a horizontal knife edge and 0.26 for Rayleigh scattering from a laser light sheet. The normalized shear layer growth is graphed as a function of the convective Mach number, given by the expression of Papamoschou and Roshko³²:

$$M_c = \frac{U_h + U_1}{a_h + a_1} \quad (4.8)$$

In this investigation, $M_c = 0.90$. The two data points are plotted in figure 4.21 with data previously obtained by Papamoschou and Roshko.³² The data from this investigation agreed favorably with the previous data. The data showed that the no swirl case was slow to mix, when compared with incompressible data.

To see the effects of swirl on the compressible shear layer growth rate, the growth rate is graphed against the helix angle extrapolated to the edge of the nozzle (the angle in the jet at the jet/ambient air interface at the nozzle exit). In fact, the calculated values of the helix flow angle, determined as described in Appendix A, were used for convenience since the calculated and measured helix angle agreed favorably at the edge of the nozzle. The compressible shear layer growth rate for the other swirl cases was determined by the same method employed in the no swirl case. These results are shown in figure 4.22 and show an increase in the shear layer growth rate with an increase in swirl. The Rayleigh scattering from a laser light sheet images showed that the high swirl case had a shear layer growth rate 4.5 times that of the no swirl case. The shear layer growth rate for the high swirl case was found to be 4.3 times that of the no swirl case using the images from focusing schlieren with a horizontal knife edge.

By measuring the shear layer growth rate, the flow visualization techniques provided some quantitative results; but flow visualization techniques primarily provide qualitative results. Therefore, the qualitative results from the various swirl cases at the matched exit pressure condition are presented below. In the no swirl case a complex system of weak shocks and waves emanating from the nozzle lip was visible above the nozzle exit (figure 4.5a, 4.11a). The system of shocks and waves was due to the discontinuity at the nozzle lip and may have been made worse by the fact that the nozzle was not designed by the method of characteristics for one-dimensional flow. This system of shocks appeared to be more or less absent for the swirl cases (figures 4.5b, 4.11c, 4.17b). In the swirl cases, the sharp radial density gradients seemed to indicate the presence of a low density region near the center of the vortical flow (figures 4.14b,c). Also at the top of the field of view, the shear layers appeared to have merged and the flow was less structured (figures 4.8b,c). The radial density gradients were also more uniform in this region. The Rayleigh scattering images presented by Cutler and Levey¹³ agreed with many of the results discussed above. Their results showed a system of weak shocks and

waves emanating from the nozzle lip for the no swirl case. The swirl cases showed a region of low density at the center of the vortical flow. Therefore at the matched exit condition, swirl was shown to cause an increase in the shear layer growth rate and eliminate the system of weak shocks and waves emanating from the nozzle lip.

The flow visualization techniques used in this investigation provided the desired results; but each technique did have some shortcomings. Shadowgraphy provided preliminary results on the effect of swirl on a supersonic jet. However, many of the finer details were suppressed. Conventional schlieren showed some of the details, such as shock structures and low density region of the vortical flow, that were not visible in the shadowgraphs. However, the focusing schlieren provided the most critical results for this investigation. The images from focusing schlieren with a horizontal knife edge showed the shear layer. Therefore, the flow visualization techniques added to the understanding of how swirl affects a supersonic jet.

4.2.2 Effect of Mismatched Exit Pressure

When the vortical flow apparatus was run at the overexpanded condition, atmospheric pressure greater than the nozzle exit pressure, it was believed that a conical shock would emanate from the nozzle exit. This condition would compress the flow and perhaps cause vortex breakdown, which is similar to the way in which vortex breakdown is induced in confined tube studies at low speeds.³⁴ In these studies, an adverse pressure gradient is created by an expansion in the tube, which causes the breakdown. The results obtained from the overexpanded condition are discussed below and compared with the results of Metwally, Settles, and Horstman.¹²

No data were obtained for the overexpanded condition of the no swirl case; therefore, no direct comparison between the no swirl case and the other swirl cases is made. In both the medium and high swirl cases, sharp radial density gradients were visible for only a short distance above the nozzle exit (figures 4.7a,b). The disappearance of these radial density

gradients seemed to indicate that vortex breakdown occurred. Metwally, Settles, and Horstman¹² proposed a hypothetical flow model for supersonic vortex breakdown, that is illustrated in figure 4.23. This was done by inspection of schlieren images of a vortex with streamwise Mach numbers of 2.2, 3.0, and 3.5 embedded in a Mach 2.0 flow. This model is compared with the images from focusing schlieren with a horizontal knife edge for the medium swirl case (figure 4.16a). These results showed a conical shock emanating from the nozzle, which is consistent with the hypothetical model. Also, a bubble shock appears just above the nozzle exit in the model, which was also apparent in the images from focusing schlieren with a horizontal knife edge. In the hypothetical flow model there is a stagnation point downstream of the bubble shock. This assumption comes from the analysis of similar types of flow, such as supersonic flow over a counterflowing sonic jet. In this flow, a stagnation point exists after the shock wave. In the hypothetical flow model, there is also a region of recirculation, which may be responsible for the stagnation point. This region of recirculation is suggested by the formation of a recompression shock downstream, which suggests that the outer region has expanded over a bubble-shaped displacement and is then recompressed. By analogy with incompressible vortex breakdown, it is assumed that the bubble-shaped displacement is really a recirculation bubble. A recompression shock was visible in the images from focusing schlieren with a horizontal knife edge. However, the existence of a recirculation region could not be confirmed by the flow visualization analysis. Cutler and Levey¹³ obtained evidence which suggested vortex breakdown for the high swirl case. Condensation penetrated to the core of the vortical flow and moved upstream towards the jet exit. Therefore at the overexpanded condition, it is suggested that vortex breakdown occurred.

At the underexpanded condition, exit pressure greater than atmospheric pressure, data were only available for the no and medium swirl case. The no swirl case had a pyramid shock structure at the nozzle exit (figure 4.6a) and for the medium swirl case, the shock structure had disappeared except for a few shocks that were visible at the nozzle exit (figure 4.6b). A shear layer was visible in the images from focusing schlieren with a

horizontal knife edge (figures 4.18a,b). However for the medium swirl case, the vortical flow remained structured and the sharp radial density gradients were visible throughout the field of view (figure 4.18b). These sharp radial density gradients seemed to indicate a region of low density near the center of the vortical flow. Therefore at the underexpanded condition, the major effect of adding swirl to the supersonic jet was to eliminate the pyramid shock structure.

5.0 INTRUSIVE MEASUREMENT TECHNIQUES

Flow visualization techniques provide primarily qualitative results. Other measurement techniques are required if precise quantitative results, such as flow angles, pressure, and temperature are desired. In this investigation, a five hole pressure probe, a static pressure probe, and a total temperature probe were used. All desired flowfield properties were either measured directly or derived from the data obtained by the three probes. A major concern when using probes is the disturbance of the flow, for this reason miniature probes were used.

5.1 Experimental Method

A brief historical overview of the five hole pressure probe, static pressure probe, and total temperature probe follows. After each overview, a detailed description of the probe used in this investigation is given. A description of the data acquisition system and methods of data reduction is also provided.

5.1.1 Five Hole Pressure Probe

The basis of the five hole pressure probe is that the pressure variation on a conical probe can be related to the Mach number, total pressure, and velocity direction at the probe. With the five measurements from the pressure taps and a suitable calibration, the Mach number, total pressure, and flow angles of supersonic flows can be determined. There are problems which arise in the development of the five hole probe. Trade-offs must be made in designing the apex angle of the cone. A large angle provides increased sensitivity to flow direction; whereas, a smaller angle minimizes the disturbance created by the probe.

Raney³⁵ was able to measure the flow direction in various supersonic wind tunnels with a 15° conical probe, 90° conical probe, and 90° pyramidal

probe. Centolanzi³⁶ then used a 40° cone to measure the Mach number, total pressure, and flow angles of supersonic flows.

Andrews and Sawyer³⁷ used these results to design their 60° included angle conical probe. Their probe was used in flows with Mach numbers up to 4.32. The probe calibration consisted of varying the pitch and roll angle. They noted that because of the small tubing dimensions, the length of the tubing to the manometers should be short to minimize the time lag effects. At the higher Mach numbers, they obtained larger errors in the calculation of the local Mach number and total pressure. This was due to the insensitivity of the cone surface pressure to higher Mach numbers.

Nebbling and Bannick³⁸ designed a five hole pressure probe with a conical head. This probe had a 0.14" outer diameter (O.D.) with each pressure orifice having an O.D. of 0.012". This probe traversed the Mach 2.94 flow by the use of three stepping motors, which allowed for movement in three directions. The pressures were measured with Statham pressure transducers, which needed settling time before the results could be recorded.

Gaillard³⁹ used a miniature five hole pressure probe in flows with Mach numbers up to 2.6. The probe had an O.D. of 0.06" with a 60° included cone angle. Gaillard studied the effect of drilling the orifice taps parallel to the probe axis and normal to the cone surface. He determined that with the orifice taps normal to the cone surface, the five hole pressure probe provided more accurate results. This probe was used to take velocity measurements in a vortex flow.

Marquart, et al.,⁴⁰ designed a miniature five hole pressure probe to measure the flow properties of a boundary layer. Their first attempt was to braze five 0.022" O.D. tubes together, but it was decided that a sturdier probe was needed. They then designed a single piece five hole probe made from Inconel 600. The five holes were drilled through the Inconel 600 and then the steel was elongated to obtain the desired O.D. Tip diameters as small as 0.03" were obtained by this process.

The design of the five hole pressure probe was part of this thesis. However after the design of the probe was completed, it was determined that

a similar probe had already been manufactured, so it was used in this investigation. The probe is illustrated in figure 5.1. The literature review suggested an included cone angle of 40° or 60° . This five hole pressure probe had an included cone angle of 51.3° . Since both included angles, 40° and 60° , provided desirable results in previous investigations, it was decided that an included cone angle of 51.3° was sufficient. Andrews and Sawyer³⁷ designed a five hole pressure probe based on the O.D. of the probe. Their dimensions were used to decide if the probe used in this investigation was suitable. The center hole should have a diameter of 0.01"; however, the probe used in this investigation had a diameter of 0.006". The results of the no swirl case, shown in Section 5.2.1, indicated that this was not a problem. The four side holes had a diameter of 0.005". This design agreed with the probe of Andrews and Sawyer,³⁷ which also suggested a diameter of 0.005". The side holes were drilled parallel to the probe axis. Gaillard³⁹ showed that the probe error was reduced by drilling the side holes normal to the cone surface. Another probe was constructed with the side holes drilled perpendicular to the cone surface, but this probe provided poor results. These poor results were believed to have been caused by the poor probe construction. The side holes should be spaced at 90° intervals around the cone. However, the two holes that were used to calculate the helix angle were separated by approximately 175° .

5.1.2 Static Pressure Probe

Static pressure is defined as the pressure measured by an instrument moving at the velocity of the flow. Over time, the design of static pressure probes has become extremely reliable. However, attention needs to be focused on the details of the probe during design and manufacturing. The probe typically consists of a small included cone angle with a number of holes equally spaced around the tip of the probe. This allows for an average static pressure to be recorded.

The size of the holes on the static probe is of particular importance. A trade-off is required between the diameter of the holes and the

response time. Rayle⁴¹ stated that the holes must have a small corner radius. This prevents errors that arise from having the flow streamlines deflect into the hole. It was also determined that as the hole diameter increases so does the error. However, Peto and Pugh⁴² more closely examined the effects of the hole size on the pressure measurements. They determined that the response time could be increased by increasing the hole's diameter. This increase had a minimal effect on the error. In this case, the holes were located near the nose of the body. Peto and Pugh also confirmed the conclusion of Liversay, et al.,⁴³ that burrs and dirt in the holes increase the error.

Pickney⁴⁴ used these results to set his criteria for a static pressure probe. Pickney's goal was to create a probe that was insensitive to the probe angle of attack and had holes close to the nose. He performed a numerical analysis on a variety of probe geometries and compared these to experimental results. He determined that a conical static pressure probe with a 10° cone-tip half-angle and a 1.5° tangent cone half-angle would be the least sensitive to Mach number.

The freestream static pressure can be obtained from the complex flow-field, which occurs over the conical tip of the static pressure probe. As the flow passes over the conical tip, it becomes compressed and an oblique shock is formed. The static pressure is increased as it crosses the oblique shock. The flow is then expanded as it passes over the probe's shoulder. The expansion fan causes a decrease in the static pressure. If the decrease in static pressure through the expansion region is equal to the increase across the oblique shock, then the true freestream static pressure is measured.

The static pressure probe designed for this investigation was based primarily on information from Pickney⁴⁴ and Lagen.⁴⁵ The probe is illustrated in figure 5.2. A piece of 304 stainless steel tubing with an O.D. of 0.06" and an I.D. of 0.04" was used to make the static pressure probe. The probe tip was a solid piece of 304 stainless steel, which was brazed into place. The cone angle was 39.5° and each of the four holes had a diameter of 0.01". The desired tangent cone half-angle was 2°, but due

to manufacturing difficulties, a value of 1.74° was accepted. This same magnitude of error was tolerable for the other dimensions, due to the miniaturization of the probe and the problems incurred in making it.

5.1.3 Total Temperature Probe

Static temperature is defined as the temperature indicated by a thermometer traveling at the velocity of the flow. It is impossible to measure this quantity with an intrusive probe in a stationary frame of reference once compressibility effects take place ($M > 0.3$). Therefore, the total temperature is measured in supersonic flows. This is the temperature of a flow brought to rest adiabatically. However, the extent to which a probe indicates this temperature is dependent on the conductivity and configuration of the probe along with the flow conditions.

The static temperature can be related to the total temperature by the equation for steady flow of a perfect gas with no loss or gain of energy:

$$T_o = T + \frac{r' U^2}{2C_p} \quad (5.1)$$

If the flow was brought to rest adiabatically, the recovery factor is equal to 1 and the kinetic energy of the flow would be completely recovered. In reality due to radiation and conduction losses, this is not possible. So the recovery factor is generally less than one and the probe indicated temperature is between the static and total temperature.

Stodola⁴⁶ was one of the first to measure the temperature of high speed flows. He used a mercury thermometer to measure the temperature drop along the axis of a nozzle. He incurred errors and determined that the superheated air was not reaching its theoretical temperature.

However around 1940, Franz⁴⁷ made a major discovery and designed the first total temperature probe. He initially used a mercury thermometer in subsonic flow supercharger investigations and also obtained poor results with this set up. Therefore, he decided to use a thermocouple at the stagnation point of a hemisphere to measure the temperature. This led to a new

total temperature probe, an enclosed thermocouple or thermometer. Therefore, Franz showed that radiation and conduction needed to be minimized to reduce the error.

At about the same time, Wimmer⁴⁸ tested various probe arrangements, changing the distance of the thermocouple from the entry hole. However, without any vent holes the highest recovery factor he obtained was 0.95.

Hottel and Kalitinsky⁴⁹ also researched temperature probe designs. They experienced difficulties in reproducing Franz's results and determined that it was related to the instability of the diffuser. Therefore, they designed a probe where the distance from the bead and the rear chamber wall could be adjusted. The vent hole openings were also adjustable.

Hottel and Kalitinsky had placed the vent holes ahead of the thermocouple bead. Malmquist⁵⁰ had difficulty in reproducing their results. He attributed this difficulty to the placement of the vent holes. It was discovered that the vent holes should not be placed in front of the bead, because there would be varying currents of air around the bead. He also determined that a large probe diameter produced more desirable results and the entry hole area should be 3 to 6 times larger than the vent hole area.

Goldstein and Scherrer⁵¹ used a 1.0" O.D. probe in flows up to Mach 2. This large diameter probe had a recovery factor of 0.99. Their emphasis was focused on minimizing the internal boundary layer by maintaining a high Reynolds number in the stagnation chamber. This would keep to a minimum the effects due to radiation and conduction. They determined that the entrance area should be 2 times the area of the vent hole for Mach 1.5 flows; however, the Mach number did not significantly affect the recovery factor. The probe was insensitive to the yaw angle up to $\pm 9^\circ$. Winkler⁵² also determined that as the Reynolds number increased, the recovery factor increased. He found that the entrance area to vent area ratio should be between 4 and 5.5.

Haig⁵³ designed a probe for use in Mach 0.2 to 1 flows by use of an analytic procedure. Haig assumed that there were three independent sources of error: velocity, radiation, and conduction. These independent errors determined how accurate the probe's results were. The size of the vent

holes was determined by assuming that the freestream static pressure was equal to the static pressure at the exit of the vent holes. Haig's probes had a maximum error of 0.2°F for 100°F flows.

In this investigation a type T (copper constantan) thermocouple was used, since cold dry air was used as the working fluid. The temperature probe is illustrated in figure 5.3. The thermocouple was shielded by a 0.06" O.D. (0.05" inner diameter (I.D.)) thin wall 304 stainless steel tubing. The tubing was made by the Accu-Tube Corporation. The two vent holes were separated by 180° and were 0.02" in diameter. An entry to vent hole area ratio of 6.25 was obtained.

It was desired to have the thermocouple bead centered in the sheath and in front of the vent holes. The 0.025" diameter bead should have been located 0.025" in front of the vent holes. However after testing, it was noticed that the bead had become lodged in one of the two vent holes. Therefore, the flow was not uniform over the bead. Since the bead may have been touching the sheath, heat conduction could have caused the bead to read a temperature other than the total temperature of the flow. These problems are discussed further in Sections 5.2.3 and 5.3.3.

5.1.4 Data Aquisition System

A block diagram of the data aquisition system is shown in figure 5.4. As was previously mentioned, the total pressure of the plenum chamber was manually controlled by varying the pressure on the incoming airline to the vortical flow apparatus. A 286 personal computer (PC) was used for all other control and data aquisition. An IEEE-488 Instrument Interface card was used to communicate with the probe motion controller, data aquisition unit, and printer. High Tech (HT) Basic was used to write the software for the data aquisition unit and probe motion controller. The data was available in real time either on screen or as a printout on a dot matrix printer. Also, real time monitoring of the probe's movement was possible with a camera and video monitor. A helium-neon laser and a microscope objective lens provided a point source and the shadow of the probe was

observed on a piece of graph paper, allowing detection of any probe movement. The data was stored on the PC hard disk drive and then data reduction was carried out on the PC with HT Basic. The data were then transferred to a floppy disk and by use of the phone lines (RS 232) and Procomm, the data were sent to a Macintosh, where they were graphed.

A Hewlett Packard (HP) Model 3497A Data Acquisition/Control Unit (3497A) with a 44421A 20 Channel Guarded Acquisition Card was used to acquire the voltage readings from the pressure transducers. The pressure transducers were placed at various locations on the vortical flow apparatus and were also used with the pressure probes. The transducers were made by various manufacturers, B&H, T Hydronic, MB Alinco, Statham, and Dynisco, and calibrated at Wyle Laboratories in Hampton, VA. The pressure transducers were tested in the laboratory set up and if the expected pressures were not obtained, the pressure transducers were recalibrated on-site. The temperature readings were obtained manually using a Fluke 2190A Digital Thermometer, Fluke 2300A Scanner, and a Fluke 2030A Printer.

A Klinger system was used to manipulate the probes. A Klinger CD4 Programmable Controller for stepping motors with an IEEE interface was used to control the movement of the probes. Two stages were employed, a translation and a rotational stage, both driven by a stepping motor. The probe movement in the radial direction was accomplished with the translation stage, which had a 100 mm range with 10 μ m step size. The rotational stage was used to align the probe with the flow (helix angle) and had a step size of 0.01°. Figure 5.5 shows a photograph of the vortical flow apparatus with the mount used for the probes, translation stage, and rotational stage. This mount was designed by the Facilities Engineering Division at NASA Langley.

5.1.5 Data Analysis

The intrusive measurement techniques provided by direct measurement the pitot pressure, flow angles, static pressure, and total temperature. These measured quantities were used to calculate other flowfield

properties, such as Mach number, total pressure, and static density. The formulas employed to calculate these properties are given below and can be found in Liepmann and Roshko.²⁸ The Mach number, M , was determined from the Rayleigh supersonic pitot formula:

$$\frac{P}{P_{o2}} = \frac{\left[\frac{2\gamma}{(\gamma+1)} M^2 - \frac{(\gamma-1)}{(\gamma+1)} \right]^{1/(\gamma-1)}}{\left[\frac{(\gamma+1)}{2} M^2 \right]^{\gamma/(\gamma-1)}} \quad (5.2)$$

In order to obtain the Mach number, the Rayleigh supersonic pitot formula was rearranged and solved with a tolerance of 0.001 using the fixed-point iteration method:

$$M = \left[\left(\frac{2}{(\gamma+1)} \right) \left(\frac{P_{o2}}{P} \right)^{(\gamma-1)/\gamma} \left[\frac{2\gamma}{(\gamma+1)} M^2 - \frac{(\gamma-1)}{(\gamma+1)} \right]^{1/\gamma} \right]^{1/2} \quad (5.3)$$

The total pressure in the flow was then calculated from the Mach number and pitot pressure:

$$P_{o1} = P_{o2} \left[\frac{2\gamma}{(\gamma+1)} M^2 - \frac{(\gamma-1)}{(\gamma+1)} \right]^{1/(\gamma-1)} \left[\frac{1 + \frac{(\gamma-1)}{2} M^2}{\frac{(\gamma+1)}{2} M^2} \right]^{\gamma/(\gamma-1)} \quad (5.4)$$

For the no swirl case (where there was no viscous core) it was thought reasonable to assume that P_o was unchanged from the plenum chamber condition. Mach number in this case was therefore also calculated using formula 5.4, which was slightly rewritten to employ the fixed-point iteration method with a tolerance of 0.001:

$$M = \left[\frac{2}{(\gamma-1)} \left[\left(\frac{P_{o2}}{P_o} \right)^{(1-\gamma)/\gamma} \left[\frac{2\gamma}{(\gamma+1)} M^2 - \frac{(\gamma+1)}{(\gamma+1)} \right]^{-1/\gamma} \left[\frac{(\gamma+1)}{2} M^2 \right] - 1 \right] \right]^{1/2} \quad (5.5)$$

The static pressure was then calculated using formula 5.2. The circles on all derived results represent the values obtained using the static pressure and pitot pressure; whereas, the triangles represent the values derived from the total pressure of the plenum chamber and the pitot pressure. The

Mach number based on sonic conditions, M^* , was calculated from the Mach number:

$$M^* = \left[\frac{(\gamma+1)}{2} \frac{1}{M^2 + (\gamma-1)} \right]^{1/2} \quad (5.6)$$

Data was presented in terms of M^* rather than M . Since with M^* the velocity is non-dimensionalized on a^* , which is dependent only on T^* ; whereas M is non-dimensionalized on a , which depends on T . M_x^* (axial velocity) is the axial component of M^* :

$$M_x^* = M^* \cos \theta \quad (5.7)$$

M_θ^* (tangential velocity) is the tangential component of M^* :

$$M_\theta^* = M^* \sin \theta \quad (5.8)$$

The freestream static temperature was calculated using the freestream stagnation temperature and Mach number:

$$T = \frac{T_o}{1 + \frac{(\gamma-1)}{2} M^2} \quad (5.9)$$

The freestream density was then calculated using the ideal gas relation:

$$\rho = \frac{P}{RT} \quad (5.10)$$

5.2 Probe Calibration and Check Out

It is desirable to calibrate a probe in a facility in which the flow-field properties are known and predictable. This method allows the probe imperfections to be separated from those of the testing facility. However, such a facility was not available for the probes used in this investigation. Therefore, the probes were calibrated in the no swirl case at $x = 5/16"$.

Structural concerns were also addressed during calibration. The probes were moved along the r axis for various helix angles. No damage or significant deflection of the probes was observed for the loads exerted by the no swirl case, so it was decided that the probes could withstand the loads in the vortical flow.

The probe data is presented only for the matched exit pressure condition. However, any variation in the plenum chamber total pressure did cause a variation in the nozzle exit pressure. Therefore, the exit pressure was held as close to 14.7 psia as was possible. In order to take these variations into account, the results are normalized by their respective total property at the plenum chamber. Table 5.1 contains the average total property values at the plenum chamber for the various swirl cases. At a radial distance of -0.5" the probe was located directly above the nozzle lip and therefore the data obtained at this location were at times inconsistent when compared with other data. The radial distance for the probe data is presented as both positive and negative values. This was used to represent the sides of the flow relative to the center.

5.2.1 Five Hole Pressure Probe

Figure 5.6 shows the dependence of the pressures from the five hole pressure probe upon yawing of the probe in the no swirl case. This figure contains two sets of data and the waiting time between the recording of each data point was 10 seconds. The waiting time was obtained by acquiring a sequence of data from a yaw angle of 10° to -10° to 10° again in increments of 2° . This sequence, or hysteresis loop, was repeated with different waiting times until the data was found to be repeatable. This same method was also employed in the calibration of the other probes and was used in deciding on the proper waiting time for the other swirl cases. These data were compared to the calibration of Gaillard³⁹ in a Mach 2.0 flow and were found to be similar. The center hole (pitot pressure) was insensitive to flow alignment within ± 5 - 10° and the pitot pressure compared

favorably with the value of $\left(\frac{P_{o2}}{P_o}\right) = 0.628$ calculated assuming quasi-one-dimensional, isentropic flow and a nozzle exit to throat area ratio of 2. The two holes used to align the probe with the flow, 1 and 3, had slope magnitudes that were similar. The two holes not used for nulling, 2 and 4, showed almost no sensitivity to the yaw angle.

The zero helix angle was defined to be the angle at the axis for the no swirl case. The helix angle for the other swirl cases was referenced to the zero helix angle. Therefore in the other swirl cases, the five hole pressure probe was nulled to the nearest degree, so the difference in pressure between holes 1 and 3 was approximately zero. Then pressure readings were taken at $\pm 5^\circ$ out of alignment with the flow. The true helix angle of the flow was then interpolated from these three points. Since the pitot pressure showed little sensitivity to alignment within $\pm 10^\circ$ of the flow, the pitot pressure was not interpolated. In the swirl cases, the static pressure probe and total temperature probe were aligned with the flow by locating them at the angle interpolated from the five hole pressure probe data.

5.2.2 Static Pressure Probe

The variation of static probe pressure with yaw angle is shown in figure 5.7 which contains two sets of data. The waiting time between sampling of data points was 10 seconds. The repeatability of the data was within 3%. Since the static pressure probe was sensitive to alignment, it needed to be aligned within 2° of the flow. In the vortical flow, the probe was aligned with the flow using the five hole pressure probe data and the static pressure was measured. However, to indicate that the probe was properly aligned, static pressures were also recorded at $\pm 5^\circ$ to the flow alignment. Symmetry of the measurements at $\pm 5^\circ$ indicated that the static pressure was measured correctly.

5.2.3 Total Temperature Probe

In Section 5.1.3 it was indicated that the thermocouple bead in the total temperature probe may have been displaced from its proper position during data acquisition. It is not known if this displacement affected the temperature results. Regardless, the results are presented and another probe is being designed to either confirm or dispute these results. Figure 5.8 shows the effect of the yaw angle on the total temperature probe, only one data set is shown on this figure. A 10 second interval was used between the acquisition of each data at each location. At a radial distance of ± 0.25 " the total temperature profiles were similar. However, the total temperature profile at $r = 0.25$ " showed more variation with the yaw angle. The profile at the center of the jet showed almost no variation with the yaw angle. Even though the total temperature probe was insensitive to alignment, it was aligned with the vortical flow during data acquisition to avoid disturbing the flow too much. Although there probably should not have been a total temperature variation across the jet in the no swirl case, the total temperature values were between 1-2% lower at a radial distance of 0" than ± 0.25 ". The total temperature variance could have been caused by the displaced thermocouple bead.

5.3 Results

The results obtained from the five hole pressure probe, static pressure probe, and total temperature probe are presented below. These include both the measured and derived results, which are compared with the theoretical calculations described in Appendix A. Probe results were obtained for four swirl cases: no, low, medium, and high. Data are shown for $-0.65 < r < 0.25$ " at $x = 5/16$ ". However, the derived results are shown for $-0.5 < r < 0.25$ " and the theoretical calculations are shown for $-0.5 < r < 0.5$ ". It was desired to obtain data as close to the nozzle exit as possible. A height of $5/16$ " was chosen, because the holes on the static

pressure probe were approximately 1/4" from the probe tip. Also, some extra height above the nozzle exit was desired, since icing occurred on the nozzle after long run times and it was desirable to have the probe avoid the ice as it moved in and out of the flow. The viscous core for the probe results is defined as the the diameter of the flow from the positive peak helix angle to the negative peak helix angle.

5.3.1 Five Hole Pressure Probe

The five hole pressure probe results consisted of one set of data for the no swirl case and two sets of data for the other swirl cases. The helix angle, θ , was measured directly using the five hole probe and the results are shown in figures 5.9-5.12. For the no swirl case, θ was less than 1° , except at the edge of the nozzle. The low swirl case results agreed favorably with the theoretical calculations up to the edge of the viscous core where viscous effects were presumed large. The theoretical calculations were inviscid, so they did not agree with the experimental results in the viscous core. The θ peak of 28° was reached at $-0.2"$ and the vortical flow was symmetric so that at $r = 0.2"$, θ was -28° . There were less data points recorded in the viscous core due to the longer response time of the probe. For example, at $r = 0$ it was necessary to wait 40 seconds for the measurement to settle to ensure repeatable results. The results for the medium swirl case were almost identical to those of the low swirl case. The high swirl case results agreed with the theoretical calculations only at the outer region of the flow. A peak value of 33° for θ was obtained in the high swirl case at a radial distance of $-0.25"$, which indicated that the viscous core was slightly larger in the high swirl case.

Since in the movement of the probe only one rotational degree of freedom was available, the radial angle, ϕ , could not be measured by nulling the probe. However, using the calibration information from holes 1 and 3 with the measured pressures of holes 2 and 4, ϕ was calculated. The equation for the pressure difference across holes 1 and 3 as a function of θ was in the form of:

$$\Delta P_{3-1} = e\theta + f \quad (5.11)$$

This equation was converted into an equation for ϕ :

$$\Delta P_{4-2} = e\phi + g \quad (5.12)$$

Equations 5.11 and 5.12 had the same value for e , and g was set equal to the pressure across holes 2 and 4, when ϕ was equal to zero (determined at the axis of the no swirl case). Equation 5.12 was slightly rearranged to provide ϕ :

$$\phi = \frac{\Delta P_{4-2} - g}{e} \quad (5.13)$$

Using this relationship ϕ was calculated for all the swirl cases. As figures 5.13-5.16 indicate, the radial velocity pointed outward and the radial angle varied linearly with the radial distance up to approximately 4° .

The pitot pressure results are shown in figures 5.17-5.20. The pitot pressure results are not discussed, but rather the derived total pressure results are discussed in Section 5.3.4.

5.3.2 Static Pressure Probe

Figures 5.21-5.24 show the static pressure results with one set of data for the no swirl case and two sets of data for the other swirl cases. Also shown in these figures are the calculated static pressures using the method of Appendix A. For the no swirl case, the static pressure derived from the pitot pressure and the plenum chamber total pressure (equations 5.5 and 5.2) is also shown. This data set is indicated by the triangles. This same type of calculation was not done for the other swirl cases, because the total pressure could not be considered constant in the nozzle. The comparison between the calculated static pressure, the static pressure derived from the pitot pressure and plenum chamber total pressure, and the directly measured static pressure, also provided an estimate of the maximum error. It is assumed that the measured static pressure was in error, due

to imperfections in the probe. The calculated static pressure was not correct, because it assumed that the nozzle was perfect. The static pressure derived from the pitot pressure and plenum chamber total pressure was in error due to uncertainties in these pressures and in the assumption that the total pressure was constant in the nozzle. Therefore, the maximum error in the static pressure measurements was 12% and the real error was probably less than this amount.

The waiting time for the other swirl cases was increased from 10 to 40 seconds. The static pressure measurements compared favorably with the theoretical calculations up to the viscous core and showed the symmetry of the vortical flow. The theoretical viscous core is defined as the region of zero static pressure, which is indicated by the theoretical calculations shown in figures 5.22-5.24. In fact, the theoretical viscous core compared favorably with the viscous core.

5.3.3 Total Temperature Probe

The total temperature results are presented in figures 5.25-5.28. The effect of the misplaced bead may have caused some of the inconsistencies in the results. One data set is presented for the no swirl case, but two data sets are shown for the other swirl cases. The total temperature results showed a variation of T_{01}/T_0 across the jet for the no swirl case between 0.97 and 0.99, where this quantity was expected to be 1.0. A drop in total temperature occurred at the center of the jet. The other swirl cases were expected to have a small drop in total temperature in the viscous core of the vortical flow. A waiting time of 20 seconds was required for the viscous core total temperature measurements. The total temperature drop was about 10% for the low swirl case and 15% for the medium and high swirl cases. The total temperature profile was not perfectly symmetric. Also in the high swirl case at a radial distance of -0.25", a large significant increase in total temperature occurred. This behavior may have been caused by the misplaced bead. However, a similar

but less profound increase occurred in the low and medium swirl cases. By conservation of energy, a total temperature decrease at one location must be accompanied by an increase elsewhere. Therefore, the total temperature increase at $r = -0.25"$ may have occurred because of the total temperature drop in the viscous core. Thus, this result may have been real, and not experimental error.

5.3.4 Derived Results

In this section, each set of results is represented by only one set of data points. Where multiple data points were acquired, they were averaged together to obtain the derived result at a given location. For example, the Mach number was calculated using P_{O2} and P , which were each measured twice, so these two values were averaged together and then used to calculate the Mach number. The equations used to derive the results presented below are described in Section 5.1.5.

The Mach number results are shown in figures 5.29-5.32. The no swirl case results derived from P and P_{O2} (experimental method #1) were within 10% of the theoretical calculations. However, the results derived from P_O and P_{O2} (experimental method #2) were within 5% of the theoretical calculations. The low and medium swirl results showed similar trends with respect to each other. However, the high swirl case had a higher peak Mach number ($M = 3.3$), but the results were not symmetric. The inviscid theoretical calculations suggested that the Mach number approaches infinity in the viscous core. In fact, the experimental results indicated that the Mach number decreased in the viscous core.

The Mach number and pitot pressure were used to calculate the total pressure. These results are presented in figures 5.33-5.36. P_{O1} should have been equal to (or at least less than) P_O for the no swirl case. However, the error was as large as 26%. Therefore, using $P_{O1} = P_O$ and the pitot pressure, the static pressure was calculated to determine how large

an error in the static pressure would cause $P_{01} \neq P_0$. These results are presented in Section 5.3.2 and show that errors in static pressure up to 12% are possible. The total pressure results for the other swirl cases indicated that the total pressure cannot be considered constant. These results showed that the nozzle boundary layer and viscous core occupy most of the flow. In fact, the high swirl results showed that the nozzle boundary layer and viscous core occupy all of the jet.

The axial component of M^* , M_x^* (axial velocity), is shown in figures 5.37-5.40. Both sets of results for the no swirl case agreed with the theoretical calculations. The low swirl experimental results showed a slight increase in the axial velocity near the center of the viscous core. M_x^* was noticeably lower on the negative side of the radial distance than the positive side. The medium swirl results also indicated a slight increase in axial speed near the viscous core. The experimental results on the outer region did agree with the theoretical calculations. The M_x^* results for the high swirl case were erratic. An increase was indicated near the viscous core; however, at a radial distance of 0.15" a low value was obtained. At a radial distance of 0.25", M_x^* had returned to its expected value. The sudden decrease at $r = 0.15$ " may have been caused by an erroneous measurement in the pitot pressure, static pressure, or total temperature.

The tangential component of M^* , M_θ^* (tangential velocity), results are shown in figures 5.41-5.43. Since the value of M_θ^* was nominally zero for the no swirl case, no results are shown. The trends of M_θ^* for the low, medium, and high swirl cases were similar. A modest increase in the peak of M_θ^* was observed as the swirl was increased. The peaks were approximately located at a radial distance of -0.25". The theoretical results compared favorably with the experimental results in the outer

region. However, the theoretical calculations suggested that M_θ^* approached infinity in the viscous core; whereas, it actually approached zero.

Figures 5.44-5.47 show the static temperature results. Since the total temperature probe results may have been in error due to the misplaced thermocouple bead, the static temperature results may also be in error. The experimental method #2 results for the no swirl case agreed more favorably with the theoretical calculations than the experimental method #1 results. The low, medium, and high swirl results were all similar. The static temperature profile for the high swirl case was about 10-15% lower than the low and medium swirl cases. The outer region results for the low and medium swirl cases agreed with the theoretical calculations. However, the theoretical calculations indicated that the static temperature would be zero in the viscous core. Actually, a small increase in static temperature occurred in the viscous core.

Figures 5.48-5.51 show the static density results. The results from experimental method #1, except for the nozzle edge value, were in almost exact agreement with the results from the Rayleigh scattering from a laser light sheet for the no swirl case.¹³ The results from experimental method #2 did not agree as well with the Rayleigh scattering results. However, all three experimental techniques agreed reasonably well with the theoretical calculations. The low swirl probe results indicated a lower density in the viscous core than the Rayleigh scattering results. Also, the probe results agreed more favorably with the theoretical calculations than the Rayleigh scattering results. No Rayleigh scattering results were available for the medium and high swirl cases. The medium and high swirl probe results indicated a larger region of low static density when compared with the low swirl probe results.

6.0 SUMMARY AND CONCLUSIONS

The objective of this investigation was to verify that the vortical flow apparatus was functioning properly and therefore, begin to quantify the effect of swirl on a supersonic jet. Flow visualization techniques were used to provide a primarily qualitative analysis of the flow. Intrusive measurement techniques were used to provide quantitative results, which were compared with inviscid theoretical calculations and Rayleigh scattering from a laser light sheet.¹³

Shadowgraphy, conventional schlieren, and focusing schlieren were the flow visualization techniques used to provide a preliminary understanding of the flow. The vertical and horizontal knife edge orientations were both used with the conventional and focusing schlieren systems. The no, medium, and high swirl cases were analyzed at the overexpanded, matched, and under-expanded exit conditions. The shear layer growth rate was obtained from the images of focusing schlieren with a horizontal knife edge at the matched exit condition. Rayleigh scattering from a laser light sheet was also used.¹³ The no swirl case results indicated that the jet was slow to spread when compared with an incompressible jet. However, an increase in swirl caused an increase in the shear layer growth rate, which indicated an increase in mixing. The shear layer growth rate of the high swirl case was approximately 4.4 times that of the no swirl case. An examination of the flow visualization results showed that the complex shock structure, which was visible in the no swirl case was less apparent in the other swirl cases. Signs of vortex breakdown were apparent in the overexpanded condition. The medium swirl case images from focusing schlieren with a horizontal knife edge were compared with Metwally, Settles, and Horstman's¹² hypothetical flow model of vortex breakdown at supersonic speeds. These results contained many of the same features as those in the hypothetical model.

A five hole pressure probe, a static pressure probe, and a total temperature probe were used to obtain quantitative flowfield results for the matched exit condition. The data were obtained for the no, low, medium,

and high swirl cases at a height of $5/16$ " above the nozzle at $-0.65" < r < 0.25"$. The probes were calibrated in the no swirl case. The five hole pressure probe provided flow angles and pitot pressure results. Helix angles as high as 33° were obtained for the high swirl case. The viscous core diameter was determined to be approximately 40% of the jet exit diameter for the low and medium swirl cases and 50% for the high swirl case. Static pressure measurements indicated low pressures in the viscous core. At $r = 0$, static pressure measurements of about 0.7 psia were obtained for the low, medium, and high swirl cases. The thermocouple bead of the total temperature probe became lodged in one of the vent holes, which may have caused some error in the total temperature measurements. The total temperature results were not perfectly symmetric and dropped in the viscous core. The measured flowfield properties were used to derive other properties, such as the Mach number, total pressure, and static density. The total pressure was calculated from the pitot and static pressures and values of about 12 psia were obtained in the viscous core. The derived results were compared with theoretical inviscid calculations, which were found to be in good agreement with the experimental results in the outer region of the vortical flow. However, the theoretical calculations did not compare favorably with the high swirl case, where the viscous core occupied most of the flow. The trends were similar for the low, medium, and high swirl cases for the derived results. The static density results for the no and low swirl cases agreed with the Rayleigh scattering from a laser light sheet.¹³ Therefore, the intrusive measurement techniques provided quantitative results, which were compared with theoretical inviscid calculations and non-intrusive measurements.

Tangential injection was proven to be a viable method to produce a high axial speed compressible flow. Preliminary results indicate that swirl increases mixing. However, more research is required in order to obtain a complete understanding of high axial speed compressible flows.

7.0 RECOMMENDATIONS

The objective of this investigation was to create a high axial speed compressible vortical flow and obtain both a qualitative and quantitative understanding of the flow. However, if adding swirl to a flow is to become a viable mixing aid in scramjet applications, a more detailed study is needed. This section provides some recommendations for future investigations.

The probe surveys showed the symmetry of the vortical flow. However, these surveys were for only $3/4$ of the exit plane diameter. Also, the surveys were taken only at the location $x = 5/16"$. Since the conditions that exist at the exit plane are the initial conditions for any future CFD work, a detailed survey of the exit plane should be taken. This means changing the current set up, so that the probe could traverse the entire diameter of the nozzle. Once this is done, more surveys should be taken to provide a detailed mapping of the exit plane. This would help to confirm that the flow is axisymmetric and also help to determine if the intrusion of the probe disturbs the flow.

In mixing studies, the exit region of the injector is not the only area of concern. The area downstream of the injector is also examined. This would provide results of whether or not mixing occurred or how rapidly it occurred. For this reason, it is recommended that a region several nozzle diameters above the exit plane be surveyed. This would also give some quantitative results in the areas of concern, specifically vortex breakdown for the overexpanded case. However non-intrusive measurements would be required, because probe interference could cause invalid results to be obtained in the region near breakdown.

It would also be desirable to study any Mach number effects on the vortical flow. Therefore, it is recommended that a set of different nozzles be designed, which would allow for the Mach number to be varied.

A major concern with the use of intrusive measurement techniques is that the probes may cause disturbances in the flow. This may result in an inaccurate measurement of the flowfield properties. If the manufacturing

problems can be corrected, it is suggested that even smaller probes be used in the vortical flow. This would give an estimate of the effect that the probes used in this investigation had on the flow.

Finally, to complete the main objective of the on-going investigation at NASA LaRC, it is recommended that vortical flow injectors be incorporated into a scramjet configuration. This configuration could then be tested to determine if vortical flow injectors enhance mixing at flight conditions.

APPENDIX A

These calculations were performed by Dr. A. D. Cutler with contributions by Dr. R. W. Barnwell, and some of the results are presented by Cutler and Levey.¹³ The nozzle and tangential injection holes were sized by the calculations below, which are also the theoretical calculations presented in Chapter 5. The calculations assumed steady state, isentropic, axisymmetric, quasi-one-dimensional (radial velocity is zero) flow in the nozzle. According to conservation of angular momentum, the fluid passing through the nozzle is required to have a uniform angular momentum, $Vr = V_n r_n$, since all of this fluid enters through the tangential injection holes at a radius r_n with velocity V_n . The flow in the nozzle is considered to be irrotational due to Crocco's theorem,²⁸ since enthalpy and entropy of the flow is constant. Therefore, assuming no radial velocity and using $Vr = a^* r^*$, the nozzle mass flow rate is:

$$\dot{m}_f = \int_{\eta_c}^{\eta_w} \rho U \pi r^{*2} d\eta^2 \quad (\text{A.1})$$

a^* is defined as the speed of sound in an isentropic nozzle where $M = 1$ and r^* is defined as the location where $M_\theta^* = 1$ and $M_x^* = 0$. Assuming isentropic flow of a perfect gas:

$$\Phi = \frac{\dot{m}_f}{\rho^* a^* r^{*2}} = \int_{\eta_c}^{\eta_w} \left[\frac{2 + (\gamma-1)M^2}{(\gamma+1)} \right]^{-1/(\gamma-1)} M_x^* \pi d\eta^2 \quad (\text{A.2})$$

$$M^2 = \frac{2 \left[1 + M_x^{*2} \eta^2 \right]}{\left[(\gamma+1) \eta^2 - (\gamma-1) \left[1 + M_x^{*2} \eta^2 \right] \right]} \quad (\text{A.3})$$

Define η_c as:

$$\eta_c = \left[\frac{(\gamma+1)}{(\gamma-1)} - M_x^{*2} \right]^{-1/2} \quad (\text{A.4})$$

From equation A.3, $M \rightarrow \infty$ as $\eta \rightarrow \eta_c$ and for $\eta < \eta_c$, the Mach number is imaginary. Therefore, η_c is the lower limit of integration for the mass flow rate. In the region $0 < \eta < \eta_c$, the pressure and density are zero; however in compressible vortical flows, viscous effects will prevent zero pressure and density values in the core.

Figure A.1 shows Φ as a function of the non-dimensional streamwise velocity, M_x^* , and the radius, η_w , for air. The results show that a converging-diverging nozzle can be used to create a high axial speed compressible vortical flow.

It is required that $\left(\frac{d\Phi}{ds}\right) = 0$ by the conservation of mass. M_x^* is related to η_w at the throat by differentiating Φ with respect to x at constant η_w :

$$\int_{\eta_{c,t}}^{\eta_{w,t}} \left[1 - \left(\frac{\gamma-1}{\gamma+1} \right) \left(M_{x,t}^{*2} + \frac{1}{\eta^2} \right) \right]^{2\gamma/(\gamma-1)} \left[1 - M_{x,t}^{*2} - \frac{(\gamma-1)}{(\gamma+1)\eta^2} \right] d\eta^2 = 0 \quad (A.5)$$

The mass flow rate through the tangential injection holes must be equal to the mass flow rate in the nozzle:

$$\rho_n A_n V_n = \Phi \rho^* a^* r^{*2} \quad (A.6)$$

Slightly rewritten to solve for $\left(\frac{A_n}{r_{w,t}^2}\right)$, equation A.6 becomes:

$$\frac{A_n}{r_{w,t}^2} = \Phi \left(\frac{\rho^*}{\rho_n} \right) \left(\frac{\eta_n}{\eta_{w,t}} \right)^2 \quad (A.7)$$

Assuming the radial and axial velocities are zero at the injectors and

using $V_n r_n = a^* r^*$, the equation for $\left(\frac{\rho^*}{\rho_n}\right)$ is:

$$\frac{\rho^*}{\rho_n} = \left[\frac{2}{(\gamma+1)} \left(1 + \frac{1}{\frac{(\gamma+1)}{(\gamma-1)\eta_n^2} - 1} \right) \right]^{1/(\gamma-1)} \quad (A.8)$$

An initial guess of $M_{x,t}^*$ is required and with this guess, Φ and $\eta_{w,t}$ can be determined using equations A.2-A.5. The design parameters, r_n and $r_{w,t}$,

are assumed to be known and therefore $\left(\frac{A_n}{r_{w,t}^2} \right)$ can be calculated using equa-

tions A.7-A.8. However, if A_n is known, then an initial guess of $M_{x,t}^*$ is required and an iteration is carried out until the proper convergence of

$\left(\frac{A_n}{r_{w,t}^2} \right)$ is met. M_x^* at the nozzle exit can now be determined, given $r_{w,e}$

and $r_{w,t}$ by using figure A.1 or an equivalent numerical routine.

Conditions at station 1 can be determined assuming zero radial and axial velocities.

The theoretical calculations presented in Chapter 5 can now be determined. The non-dimensional tangential velocity, M_θ^* , is determined from:

$$M_\theta^* = \left(\frac{r_{w,t}}{r} \right) \left(\frac{1}{\eta_{w,t}} \right) \quad (A.9)$$

The Mach number based on sonic conditions, M^* , can be calculated:

$$M^* = \left(M_\theta^{*2} + M_x^{*2} \right)^{1/2} \quad (A.10)$$

The Mach number can be determined using M^* :

$$M = \left(\frac{M^{*2}}{\frac{(\gamma+1)}{2} - \frac{(\gamma-1)}{2} M^{*2}} \right)^{1/2} \quad (A.11)$$

The helix angle, θ , is calculated from:

$$\theta = \tan^{-1} \left(\frac{M_\theta^*}{M_x^*} \right) \quad (A.12)$$

The static pressure, temperature, and density can be determined using the following isentropic relationships:

$$\frac{T}{T_0} = \left(1 + \frac{(\gamma-1)}{2} M^2 \right)^{-1} \quad (\text{A.13})$$

$$\frac{P}{P_0} = \left(1 + \frac{(\gamma-1)}{2} M^2 \right)^{-\gamma/(\gamma-1)} \quad (\text{A.14})$$

$$\frac{\rho}{\rho_0} = \left(1 + \frac{(\gamma-1)}{2} M^2 \right)^{-1/(\gamma-1)} \quad (\text{A.15})$$

The mathematical technique described above fails for the no swirl case, because the tangential velocity is zero in the no swirl case. However, the assumptions of isentropic, quasi-one-dimensional flow were used in the theoretical calculations for the no swirl case.

REFERENCES

1. Piland, W.M.: Technology Challenges for the National Aero-Space Plane. Paper IAF-87-205, October 1987.
2. Ferri, A.: Review of SCRAMJET Propulsion Technology. AIAA Paper 66-826, November 1966.
3. Waltrup, Paul J.; Anderson, Griffin Y.; and Stull, Frank D.: Supersonic Combustion Ramjet (Scramjet) Engine Development in the United States. Proceedings - 3rd International Symposium on Air Breathing Engines, pp. 835-861, June 1976.
4. Northam, G. Burton; and Anderson, G. Y.: Supersonic Combustion Ramjet Research at Langley. AIAA Paper 86-0159, January 1986.
5. Hannum, N. and Berkopce, F.: Fueling the National Aero-Space Plane with Slush Hydrogen. AIAA Paper 89-5014, July 1989.
6. Czysz, Paul; and Murthy, S. N. B.: Energy Analysis of Propulsion Systems for High Speed Vehicles. AIAA Paper 89-0182, January 1989.
7. Papamoschou, D. and Roshko, A.: Observations of Supersonic Free Shear Layers. AIAA Paper 86-0162, January 1986.
8. Northam, G. Burton; Capriotti, D. P.; Byington, C. S.; and Greenberg, I.: Mach 2 and Mach 3 Mixing and Combustion in Scramjets. AIAA Paper 91-2394, June 1991.
9. Swithenbank, J., and Chigier, N. A.: Vortex Mixing for Supersonic Combustion. XIIth International Symposium on Combustion, pp. 1153-1162, July 1968.
10. Leibovich, S.: Vortex Stability and Breakdown: Survey and Extension. AIAA Journal, Vol. 22, No. 9, pp. 1192-1206, September 1984.
11. Swanson, R. C.; and Schetz, J. A.: Turbulent Jet Mixing in a Supersonic Stream. NASA CR 111981, October 1971.
12. Metwally, O.; Settles, G.; and Horstman, C.: An Experimental Study of Shock Wave/Vortex Interaction. AIAA Paper 89-0082, January 1989.
13. Cutler, A. D.; and Levey, B. S.: Vortex Breakdown in a Supersonic Jet. AIAA 91-1815, June, 1991.

14. Ranque, G. J.: Experiences Sur la Detente Giratoire Avec Productions Simultanees d'un Echappement d'Air Chaud et d'un Echappement d'Air Froid. Bulletin Bi-Mensuel de la Societe Francaise de Physique, pp. 112,S-115,S, June 1933. Translated by General Electric Company, Schenctady Works Library, T.F. 3294, 1947.
15. Hilsch, R.: The Use of the Expansion of Gases in a Centrifugal Field as Cooling Process. The Review of Scientific Instruments, Vol. 18, No. 2, pp. 108-113, February 1947.
16. Hartnett, J. P.; and Eckert, E. R. G.: Experimental Study of the Velocity and Temperature Distribution in a High Velocity Vortex Type Flow. University of Minnesota Heat Transfer Laboratory Technical Report No. 6, September 1955.
17. Lay, J. E.: An Experimental and Analytical Study of Vortex-Flow Temperature Separation by Superposition of Spiral and Axial Flows (Parts 1 & 2). ASME Journal of Heat Transfer, Vol. 81, pp. 202-222, August 1959.
18. Savino, Joseph M.; and Ragsdale, Robert G.: Some Temperature and Pressure Measurements in Confined Vortex Fields. ASME Journal of Heat Transfer, Vol. 83, pp. 33-38, February 1961.
19. Mandella, M.; and Bershader, D.: Quantitative Study of the Compressible Vortex: Generation, Structure and Interaction with Airfoils. AIAA Paper 87-0328, January 1987.
20. Westley, R.: A Bibliography and Survey of the Vortex Tube. The College of Aeronautics Cranfield, Note No. 9, March 1954.
21. Gostintsev, Yu. A.; Zelentsov, V. V.; Ilyukhin, V. S.; and Pokhil, P. F.: Structure of Underexpanding Supersonic Swirling Gas Jet. Izv. AN SSSR. Mekhanika Zhidkosti i Gaza, Vol. 4, No. 5, pp. 158-162, 1969. Translated in Fluid Dynamics, Vol. 4, No. 5, pp. 105-107, September-October 1969.
22. Délery, J.; Horowitz, E.; Leuchter, O.; and Solignac J. L.: Fundamental Studies on Vortex Flows. La Recherche Aéronautique, pp. 1-24, 1984-2.

23. Metwally, O. M.; and Settles, G. S.: Measurements of a Supersonic Turbulent Vortex. Proceedings - 11th Symposium on Turbulence at University of Missouri-Rolla, pp. A31-1 to A31-5, October 1988.
24. Escudier, M. P.; Bornstein, J.; and Zehnder, N.: Observations and LDA Measurements of a Confined Turbulent Vortex Flow. Journal of Fluid Mechanics, Vol. 98, Part 1, pp. 49-63, May 1980.
25. Philbert, Michel; Surget, Jean; and Véret, Claude: Shadowgraph and Schlieren from Handbook of Flow Visualization (Chapter 12, pp. 189-201). Hemisphere Publishing Corporation, 1989.
26. Beams, J. W.: Shadow and Schlieren Methods from Volume IX High Speed Aerodynamics and Jet Propulsion - Physical Measurements in Gas Dynamics and Combustion (Chapter A,2, pp. 26-46). Princeton University Press, 1954.
27. Holder, D. W.; and North, R. J.: Part One: Schlieren Methods from Optical Methods for Examining the Flow in High-Speed Wind Tunnels. AGARDograph 23, November 1956.
28. Liepmann, H. W.; and Roshko, A.: Elements of Gasdynamics (Chapter 6.9-6.13, pp. 153-163). John Wiley & Sons, Inc., 1957.
29. Merzkirch, Wolfgang: Flow Visualization (Chapter 3.2-3.3, pp. 76-100). Academic Press, Inc., 1974.
30. Pope, Alan; and Goin, Kenneth L.: High-Speed Wind Tunnel Testing (Chapter 6.16-6.17, pp. 229-235). Robert E. Krieger Publishing Company, 1978.
31. Weinstein, Leonard M.: An Improved Large-Field Focusing Schlieren System. AIAA 91-0567, January 1991.
32. Papamoschou, Dimitri; and Roshko, Anatol: The Compressible Turbulent Shear Layer: An Experimental Study. Journal of Fluid Mechanics, Vol. 197, pp. 453-477, December 1988.
33. Papamoschou, D.: Structure of the Compressible Turbulent Shear Layer. AIAA Paper 89-0126, January 1989.
34. Hall, M. G.: Vortex Breakdown. Annual Review of Fluid Mechanics, Vol. 4, pp. 195-218, 1972.

35. Raney, D. J.: Flow Direction Measurements in Supersonic Wind Tunnels. A.R.C. C.P. 262, September 1954.
36. Centolanzi, Frank J.: Characteristics of a 40° Cone for Measuring Mach Number, Total Pressure, and Flow Angles at Supersonic Speeds. NACA TN 3967, May 1957.
37. Andrews, D. R.; and Sawyer, W. G.: The Calibration of a 60° Cone to Measure Mach Number, Total Pressure and Flow Angles at Supersonic Speeds. A.R.C. C.P. 628, June 1962.
38. Nebbling, C.; and Bannick, W. J.: Experimental Investigation of the Supersonic Flow Past a Slender Cone at High Incidence. Journal of Fluid Mechanics, Vol. 87, Part 3, pp. 475-496, July-August 1978.
39. Gaillard, R.: Calibration and Use of an ONERA Miniature Five Hole Probe. ONERA TP 1984-2, 1984.
40. Marquart, E. J.; Stepanek, S. A.; Byers, M. T.; and Donaldson, J. C.: Development and Calibration of Miniature Mach/Flow-Angularity Probes. AIAA 84-0630, March 1984.
41. Rayle, Roy E. Jr.: An Investigation of the Influence of Orifice Geometry on Static Pressure Measurements. Master of Science Thesis, Massachusetts Institute of Technology, May 1949.
42. Peto, J. W.; and Pugh, P. G.: The Effects of the Presence of Static Holes on the Measurement of Static Pressures on Models at Supersonic Speeds. N.P.L. Aero Report 1292, March 1969.
43. Liversay, J. L.; Jackson, J. D.; and Southern, C. J.: The Static Hole Error Problem: An Experimental Investigation of Errors for Holes of Varying Diameters and Depths. Aircraft Engineering (Vol. 34, pp. 43-47), Bunhill Publishing Ltd., February 1962.
44. Pickney, S. Z.: A Short Static-Pressure Probe Design for Supersonic Flow. NASA TN D-7978, July 1975.
45. *Personal Communications*, Nicholas T. Lagen, Lockheed Contractor at NASA Langley Research Center.
46. Stodola, A.: Z. VDI, Vol. 47, p. 1787, December 1903.
47. Franz, A.: Pressure and Temperature Measurement in Supercharger Investigations. NACA TM 953, September 1940.

48. Wimmer, W.: Stagnation Temperature Recording. NACA TM 967, January 1941.
49. Hottel, H. C.; and Kalitinsky, A.: Temperature Measurements in High-Velocity Air Streams. Journal of Applied Mechanics, pp. A-25 to A-32, March 1945.
50. Malmquist, Lars: Temperature Measurements in High-Velocity Gas Streams. Acta Polytechnica Mechanical Engineering Series, Vol. 1, Nr. 4, 1948.
51. Goldstein, David L.; and Scherrer, Richard: Design and Calibration of a Total-Temperature Probe for Use at Supersonic Speeds. NACA TN 1885, May 1949.
52. Winkler, Eva M.: Design and Calibration of Stagnation Temperature Probes for Use at High Supersonic Speeds and Elevated Temperatures. Journal of Applied Physics, Vol. 25, No. 2, pp. 231-232, February 1954.
53. Haig, Laurence B.: A Design Procedure for Thermocouple Probes. SAE National Aeronautic Meeting - Paper N-81685, April 1960.



Figure 1.1: Artist's Conception of Single-Stage-to-Orbit Vehicle

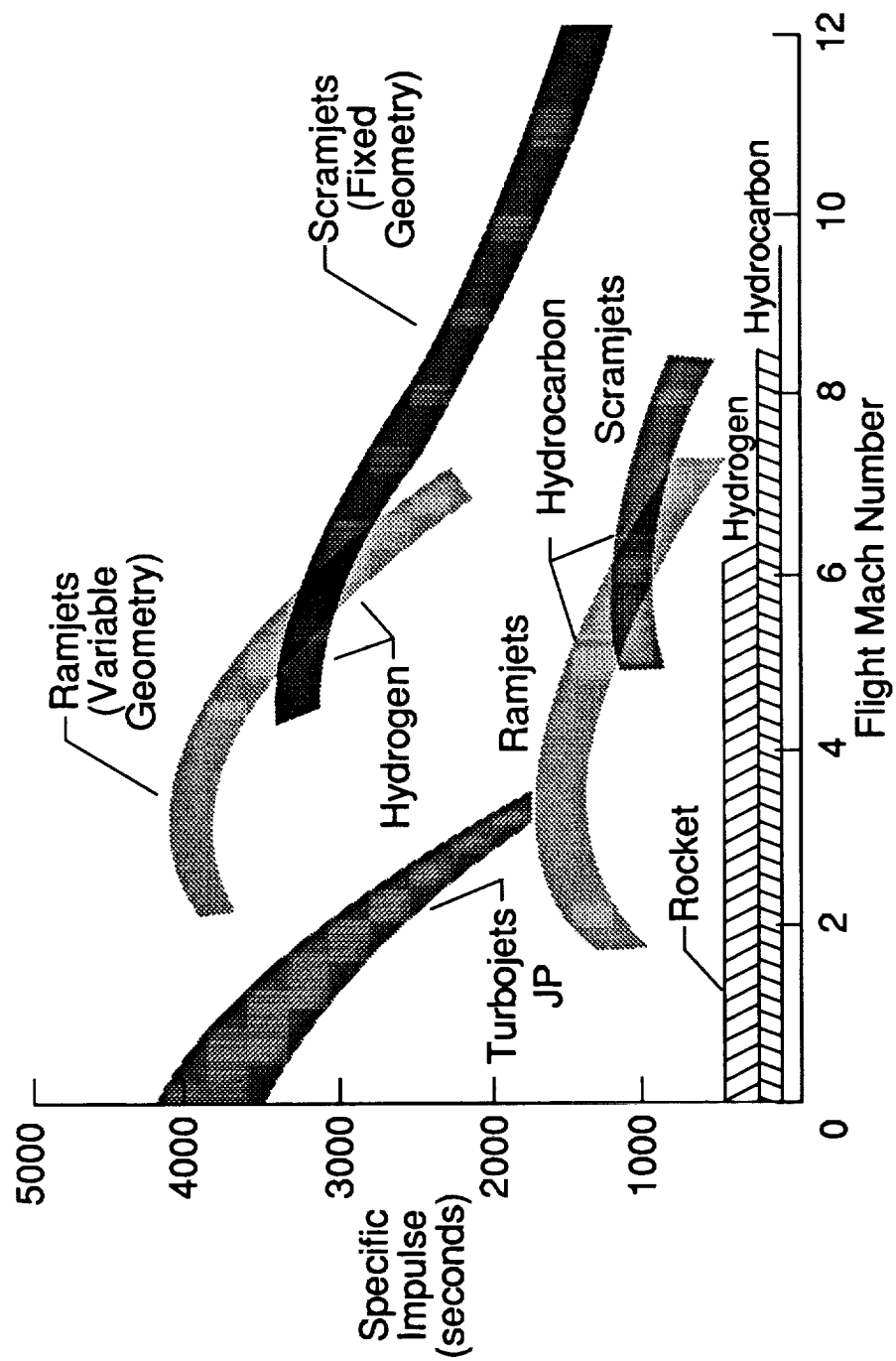


Figure 1.2: Operating Range for Various Propulsion Alternatives

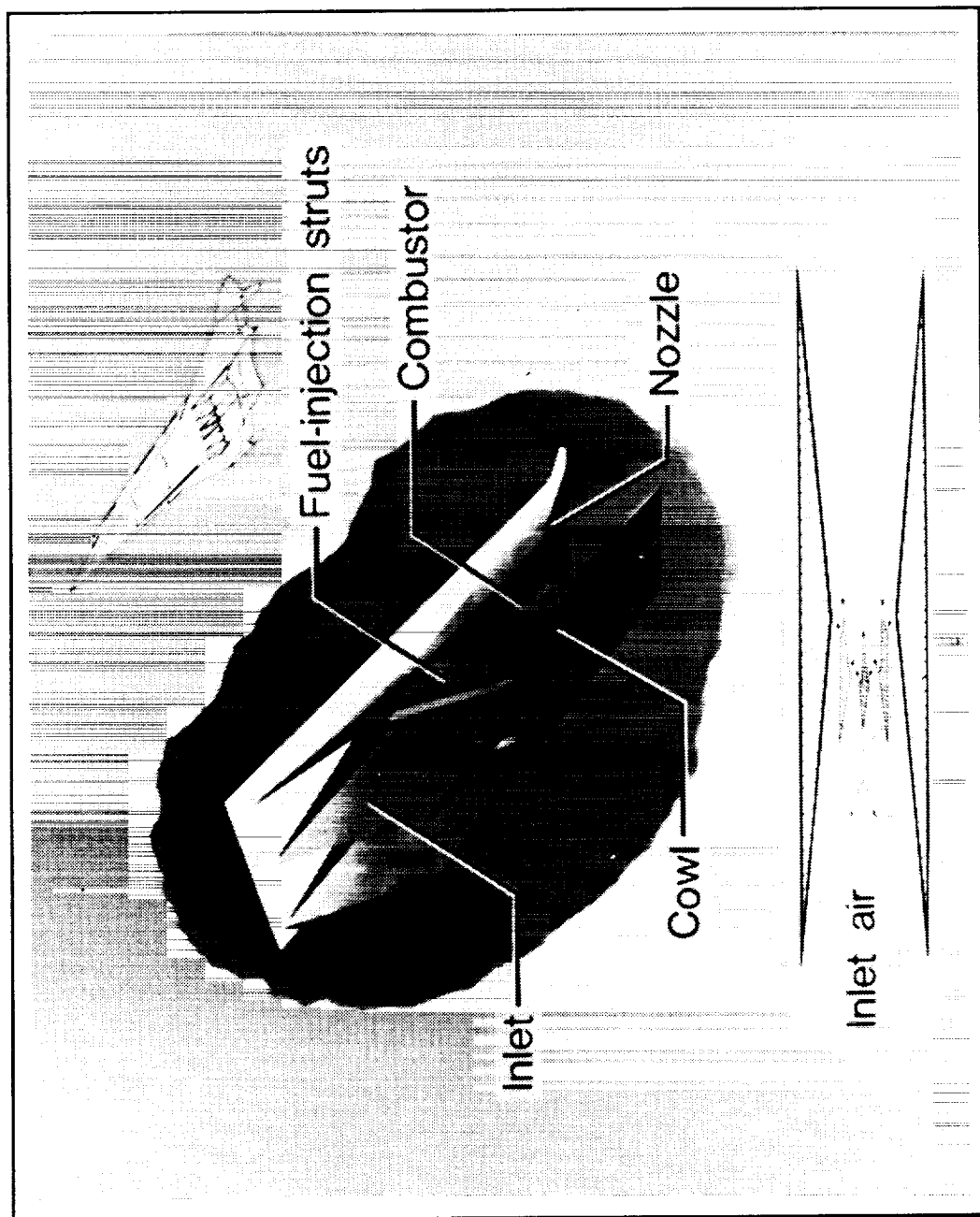


Figure 1.3: Airframe-Integrated Scramjet Model

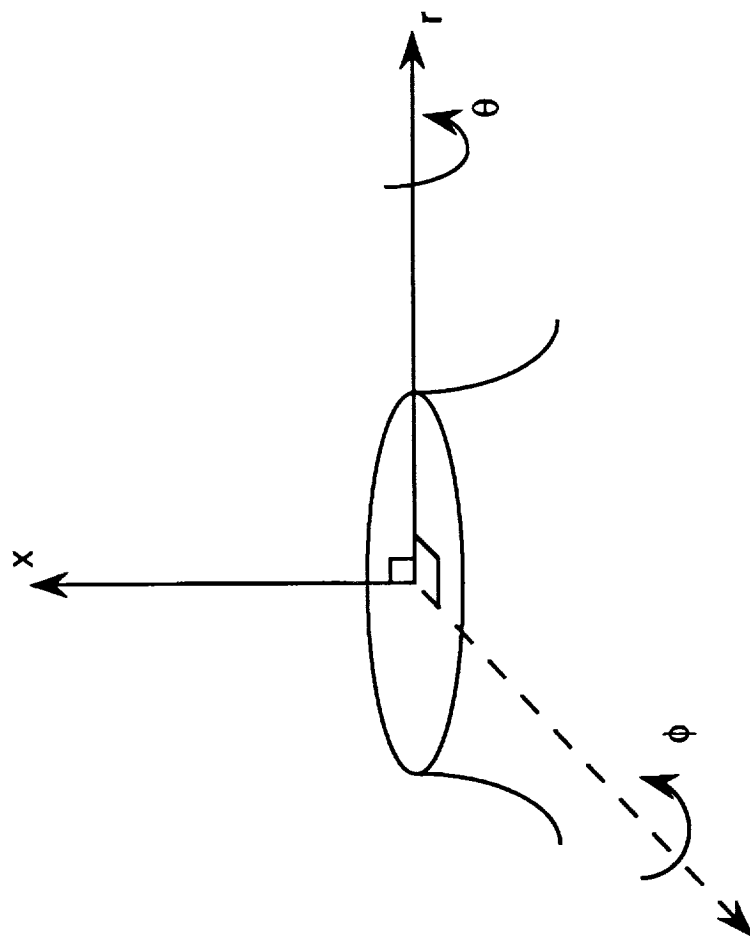


Figure 3.1: Coordinate System for Vortical Flow Apparatus

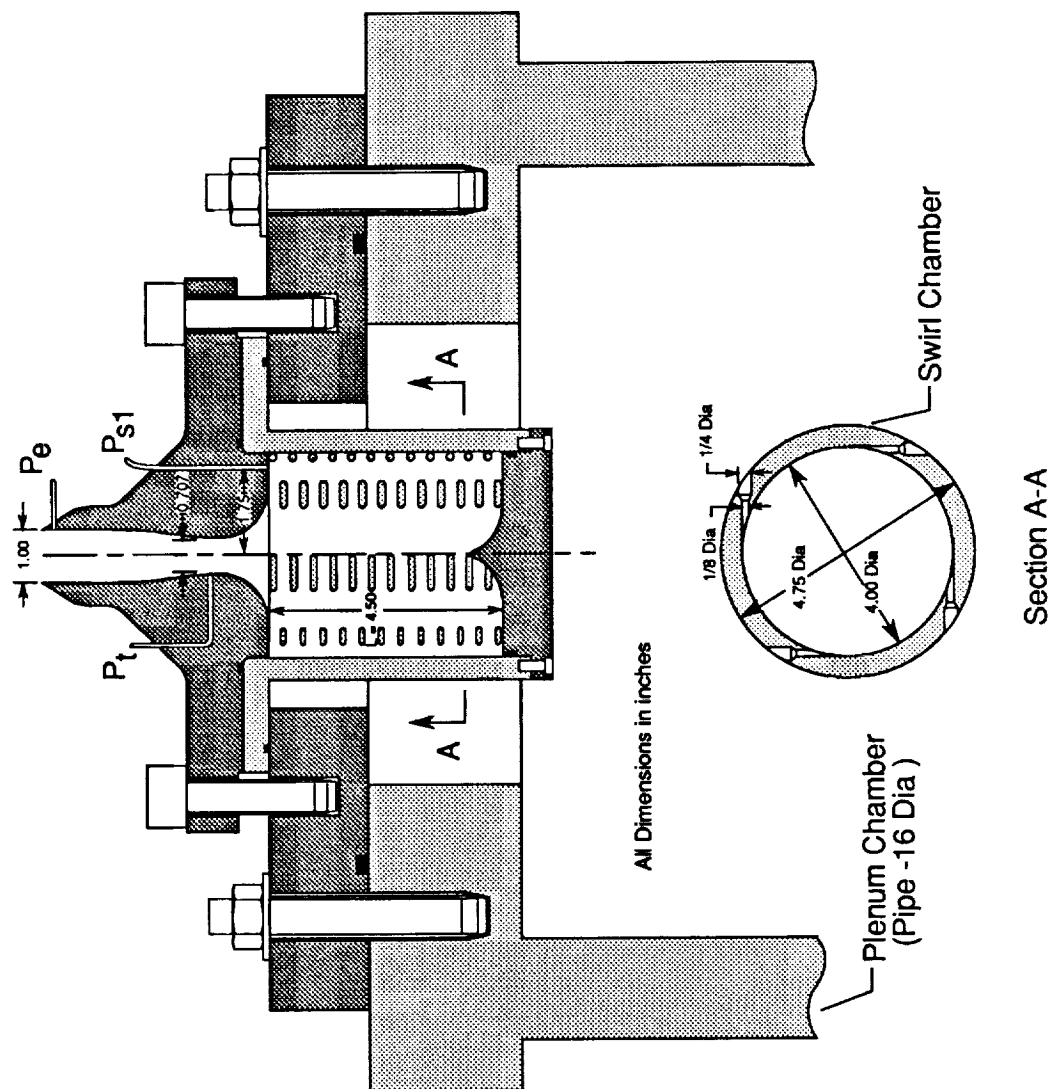


Figure 3.2: Vortical Flow Apparatus

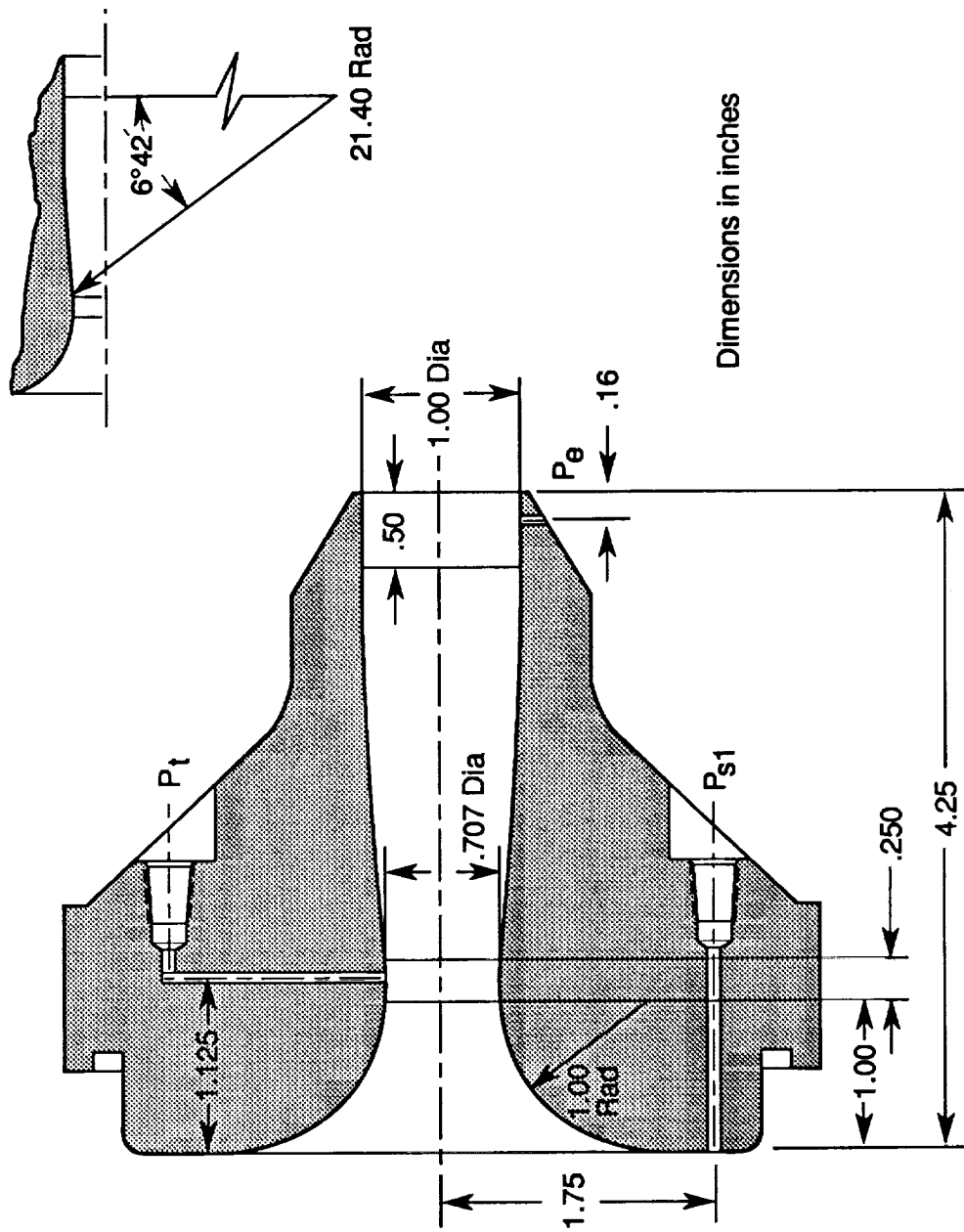


Figure 3.3: Nozzle Contour

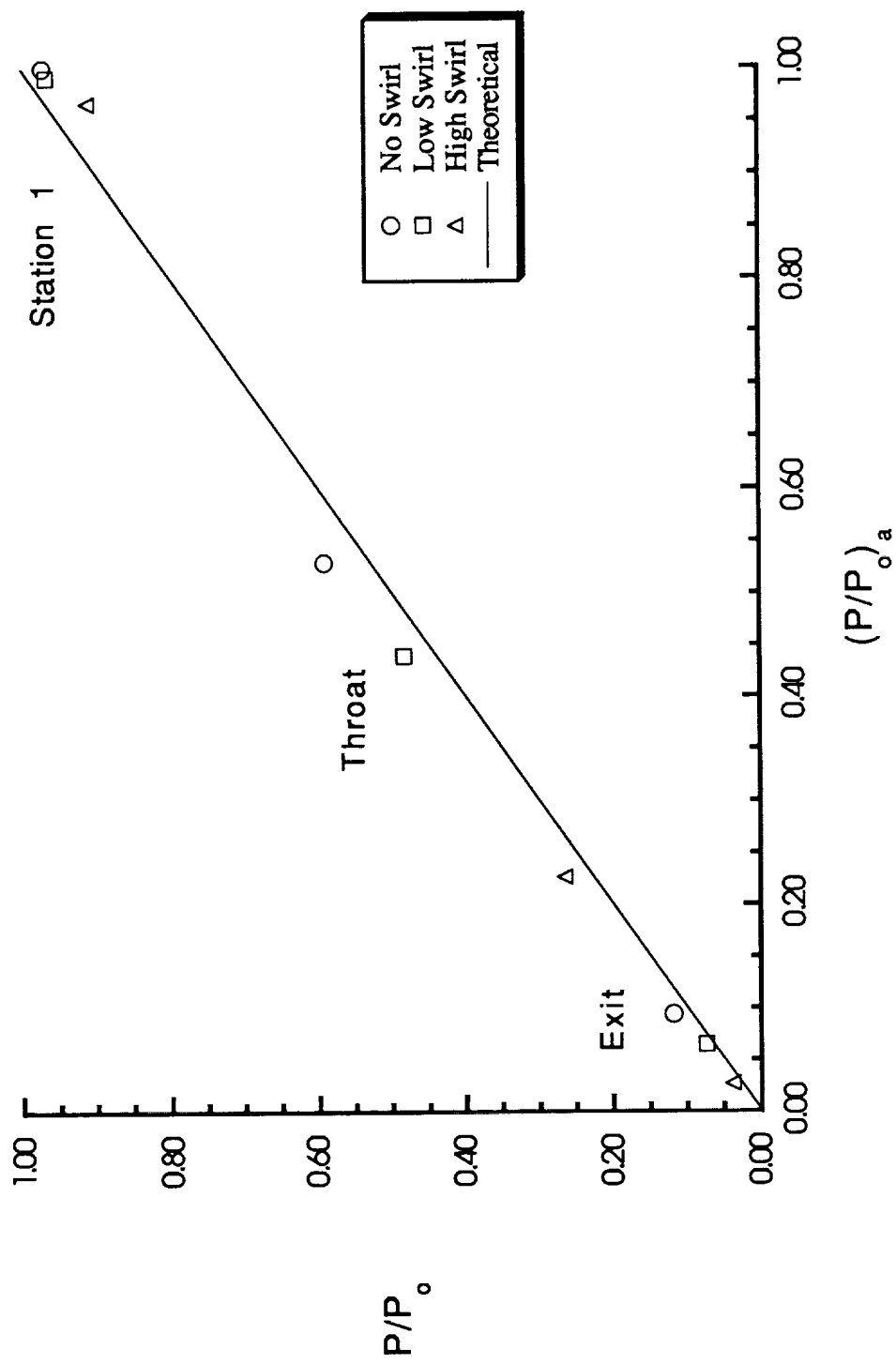


Figure 3.4: Measured Pressures Compared with Theoretical Pressures

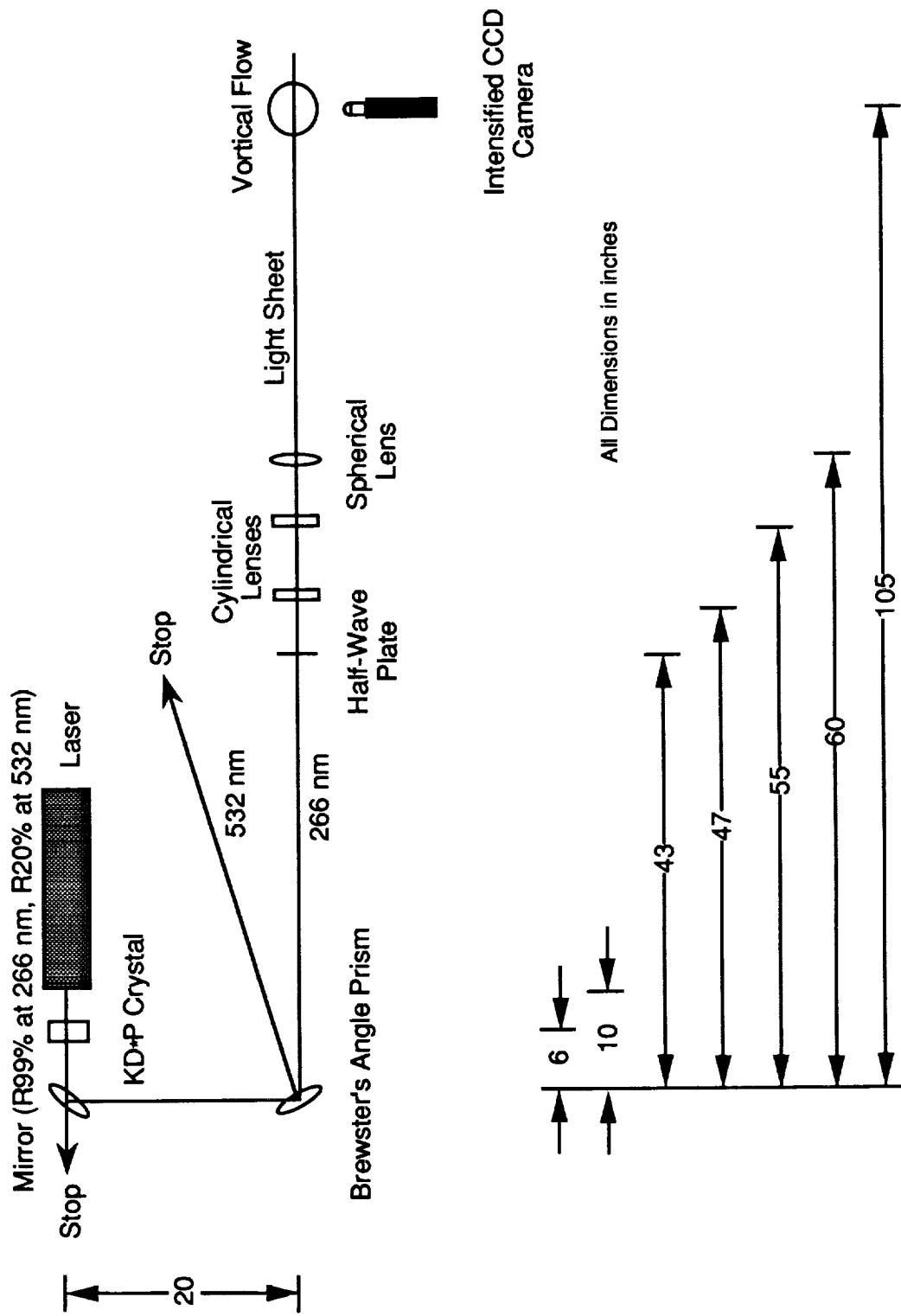


Figure 4.1: Rayleigh Scattering from a Laser Light Sheet System

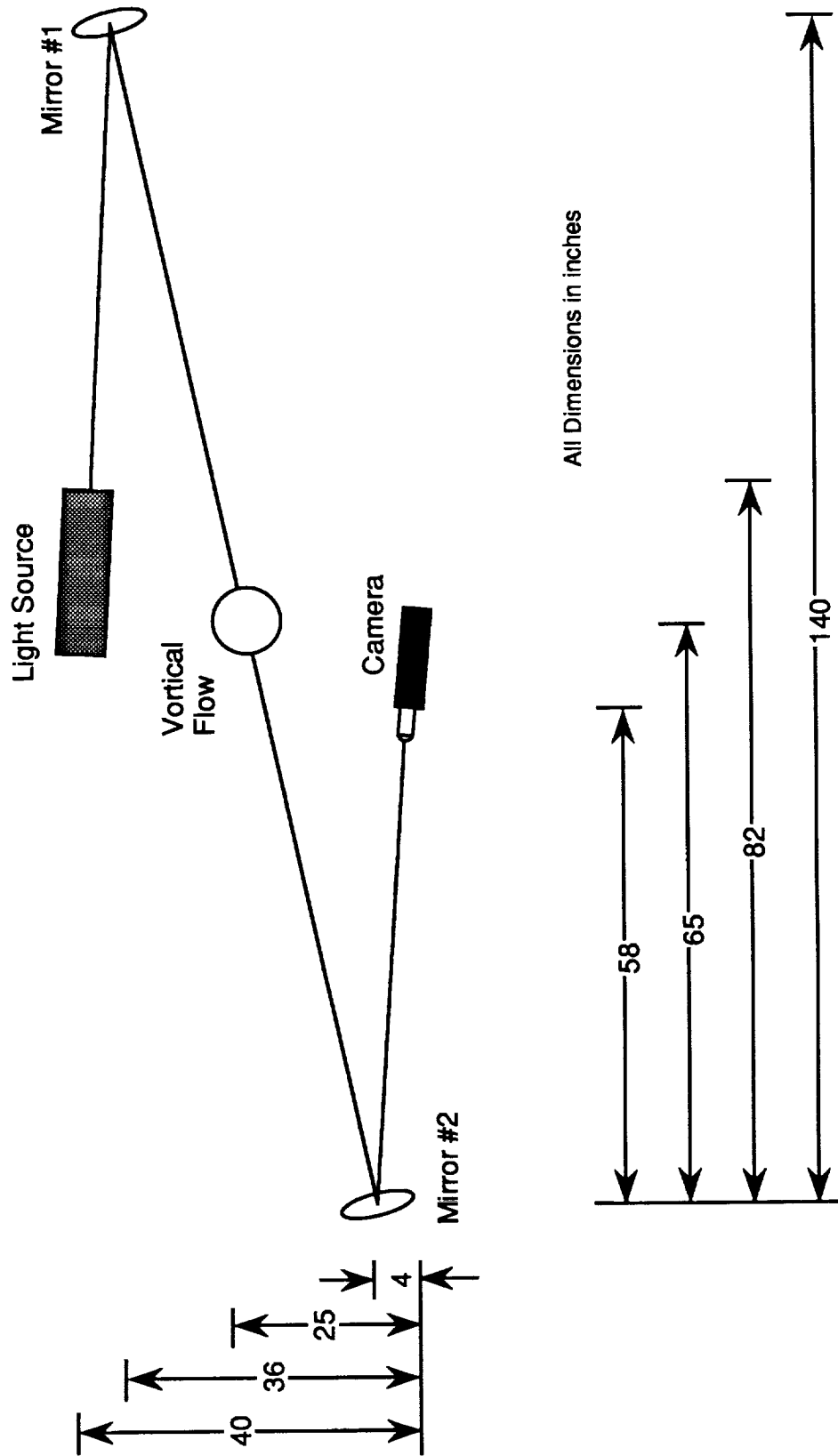


Figure 4.2a: Shadowgraphy System

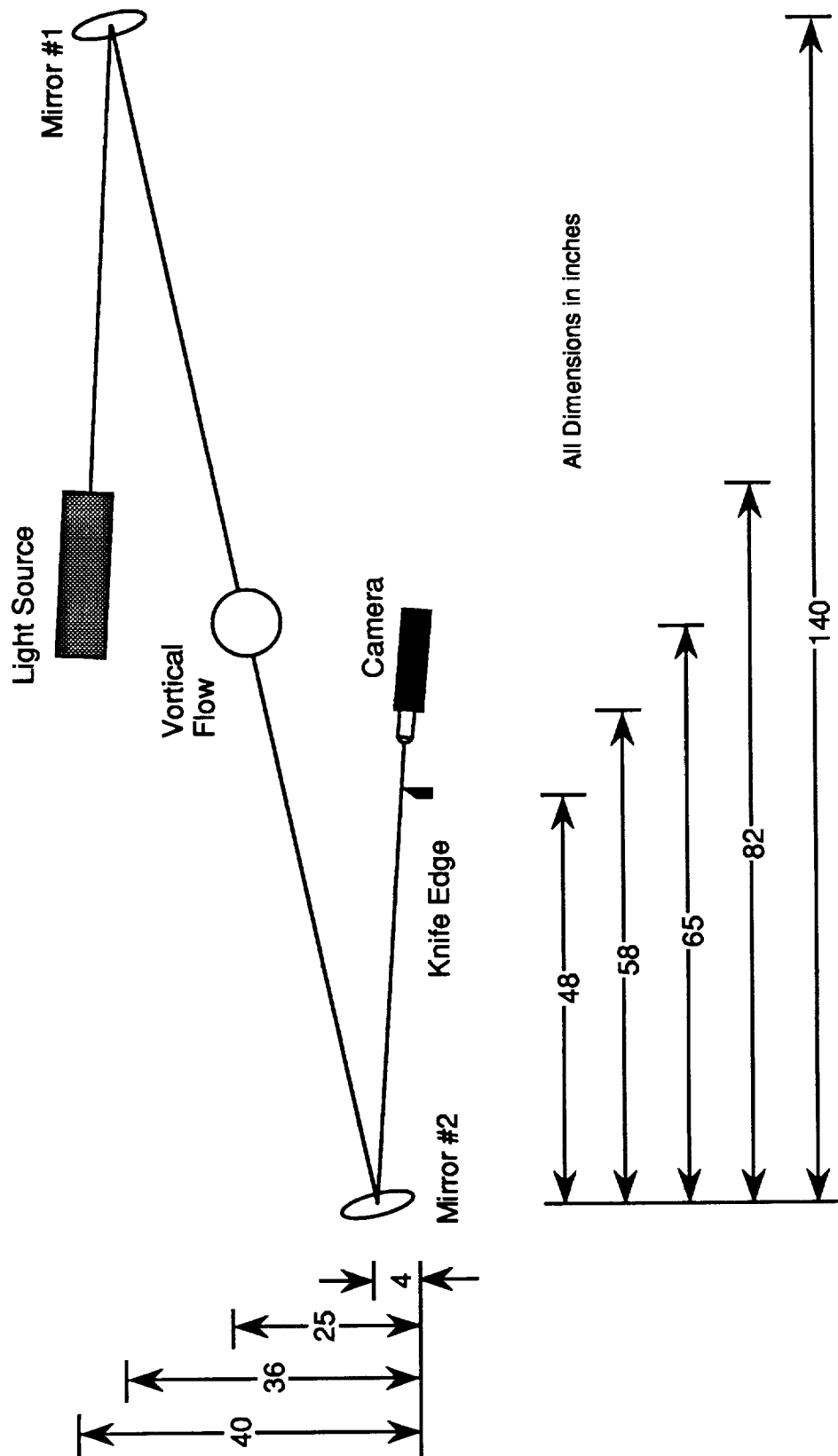
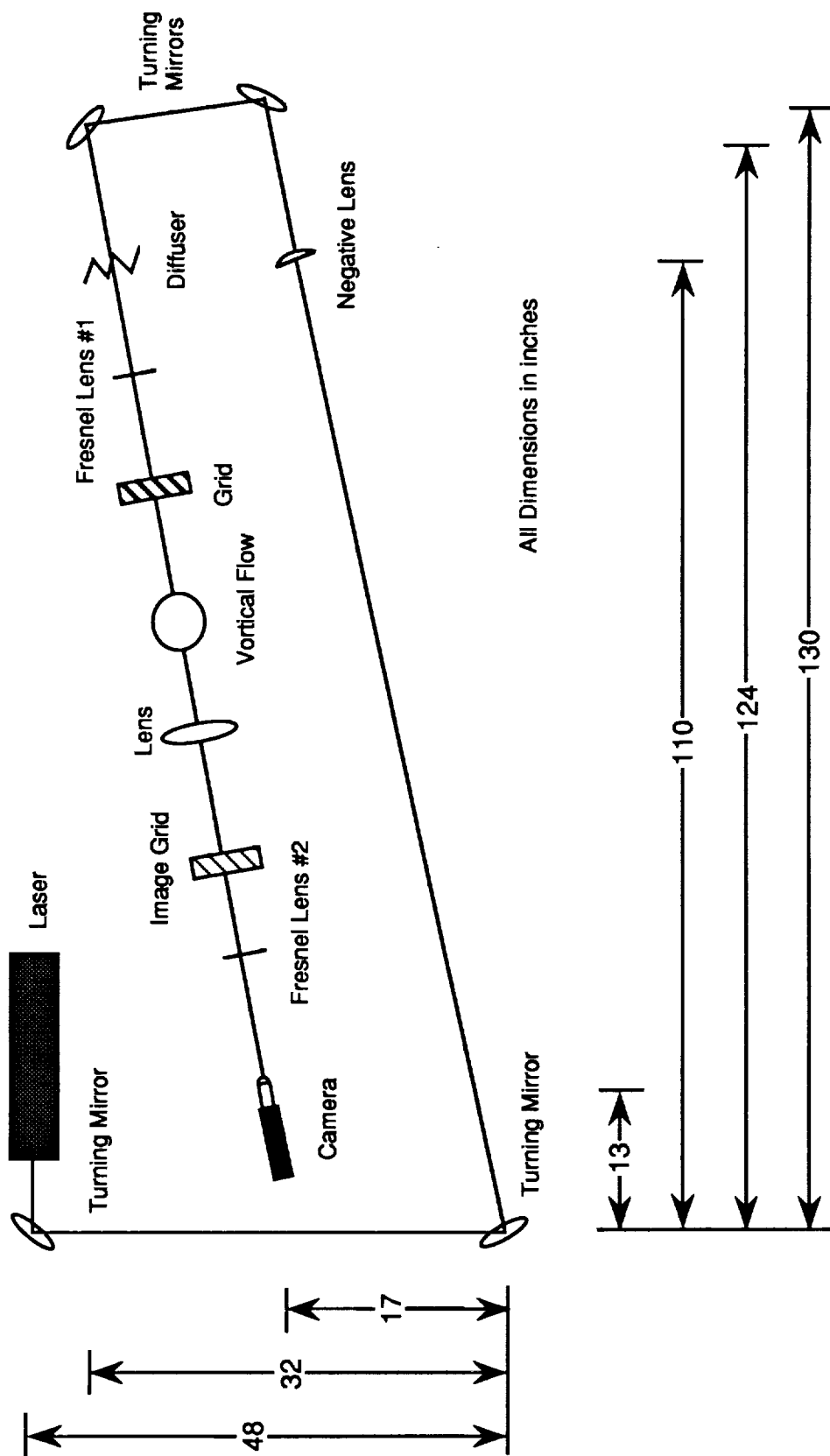
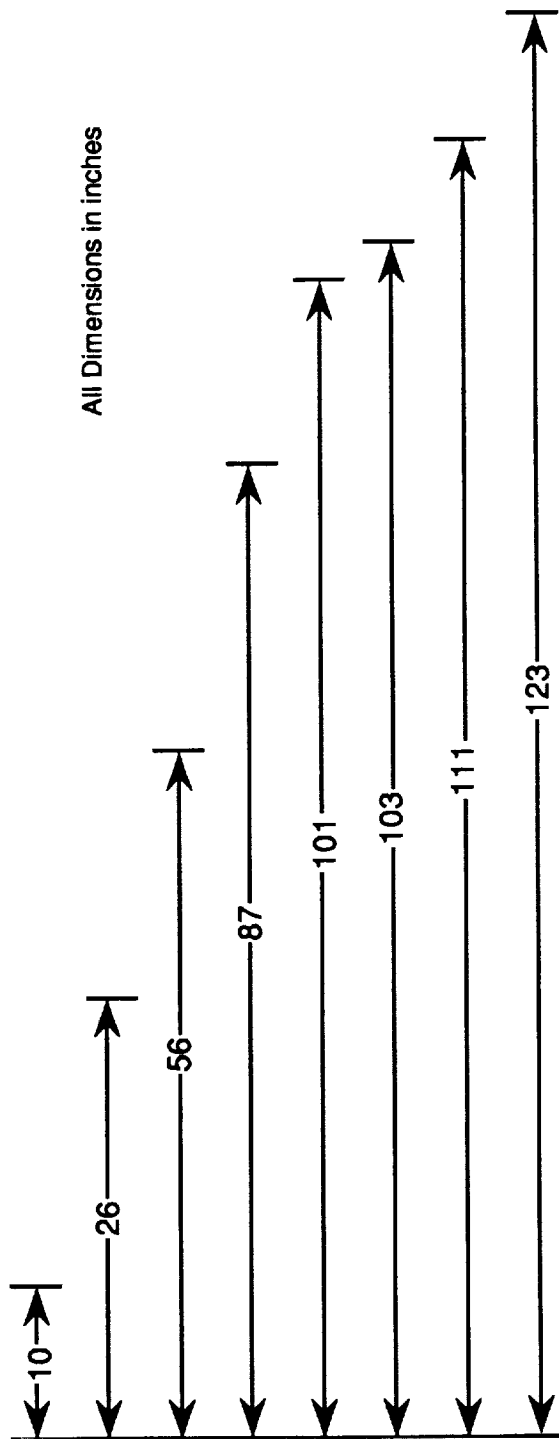
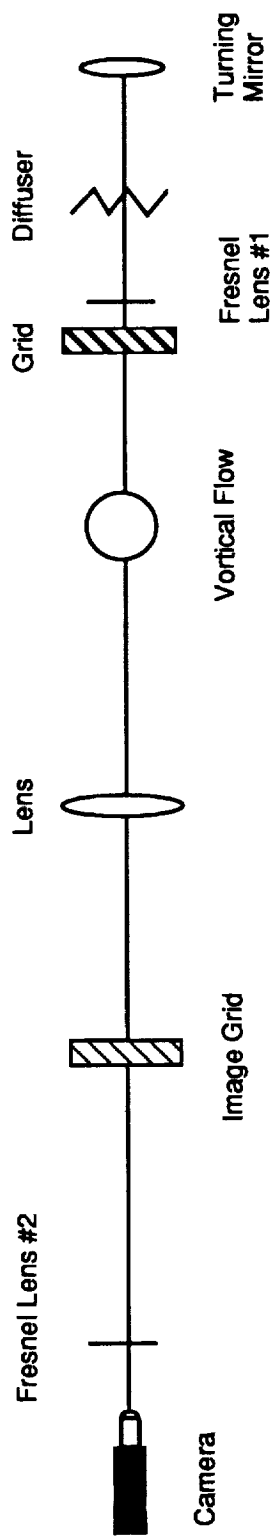


Figure 4.2b: Conventional Schlieren System



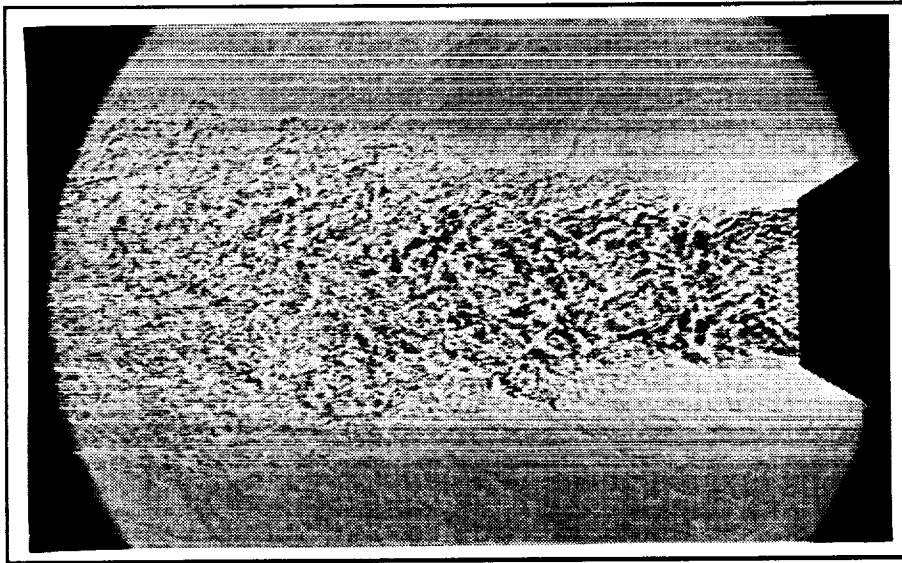
a: Complete View

Figure 4.3: Focusing Schlieren System

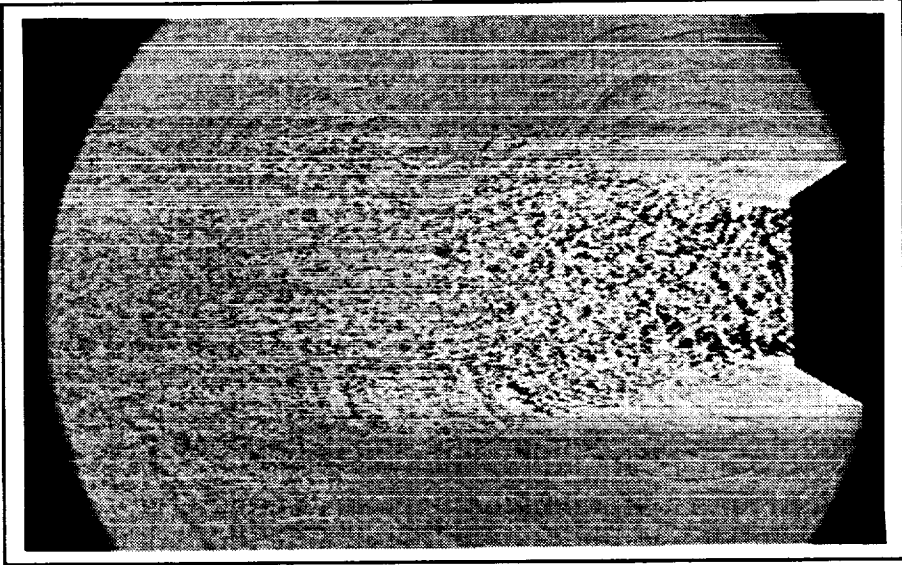


b: Detailed View

Figure 4.3 continued

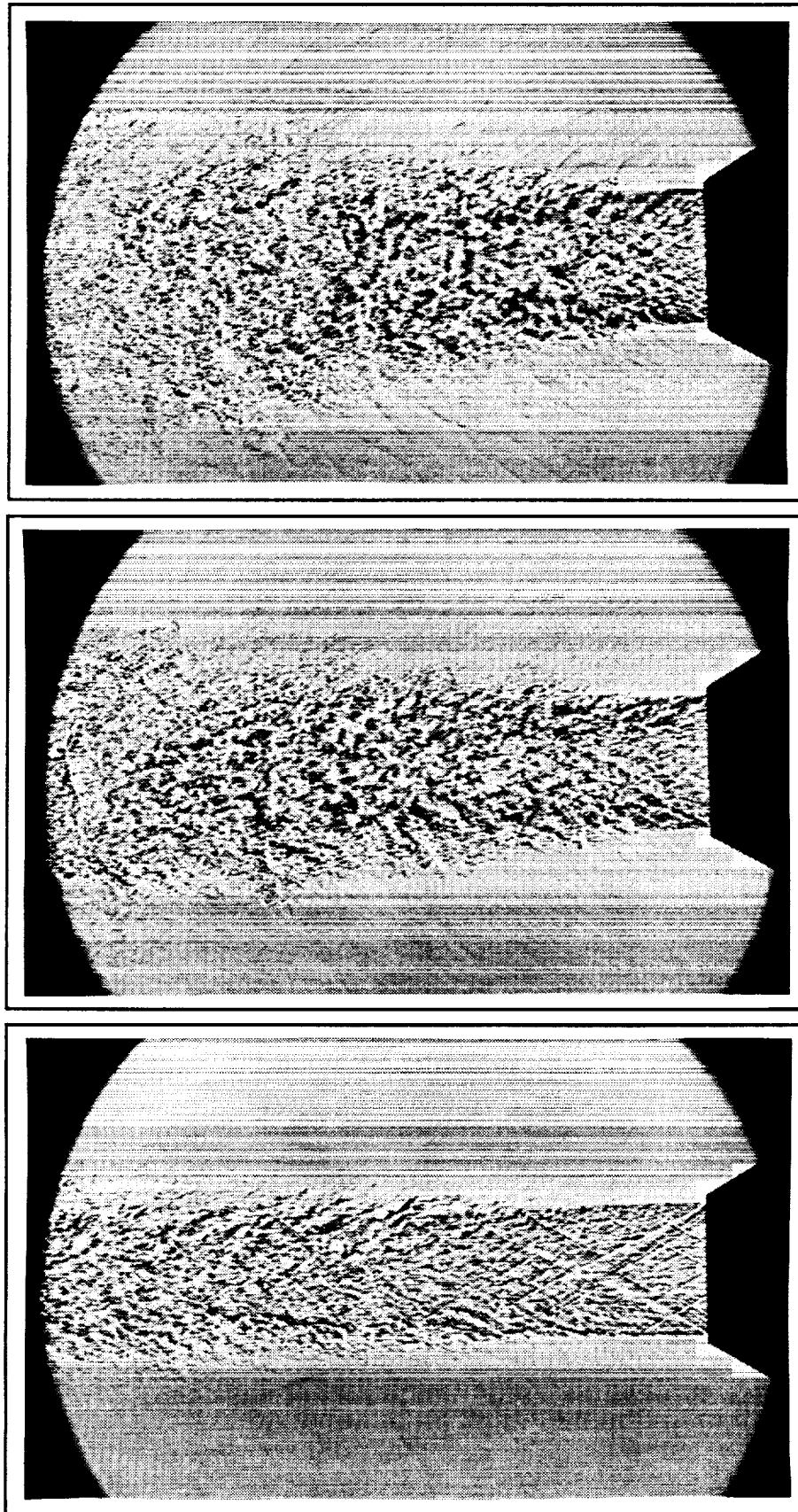


a) Medium Swirl: $P_e = 10.7$ psia



b) High Swirl: $P_e = 9.9$ psia

Figure 4.4: Shadowgraphs for Overexpanded Condition

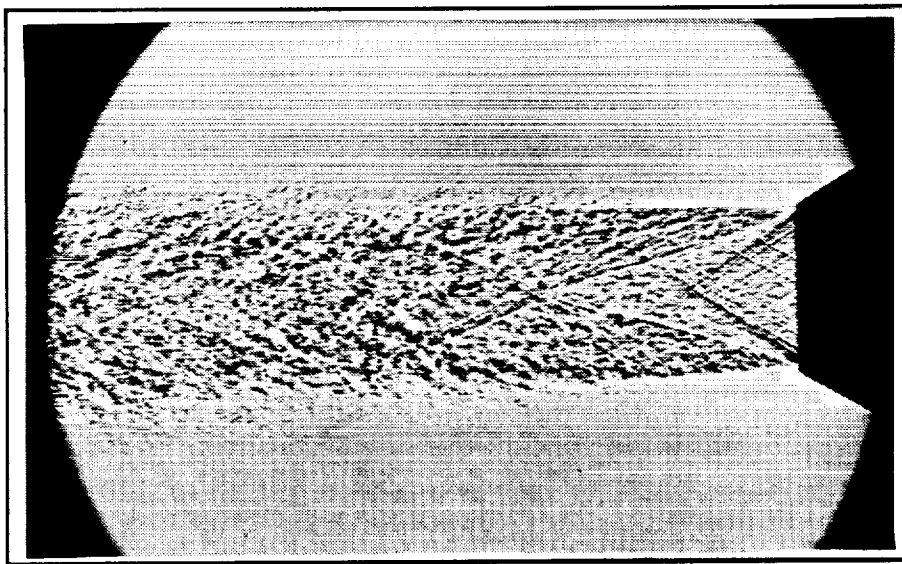


a) No Swirl: $P_e = 16.3$ psia

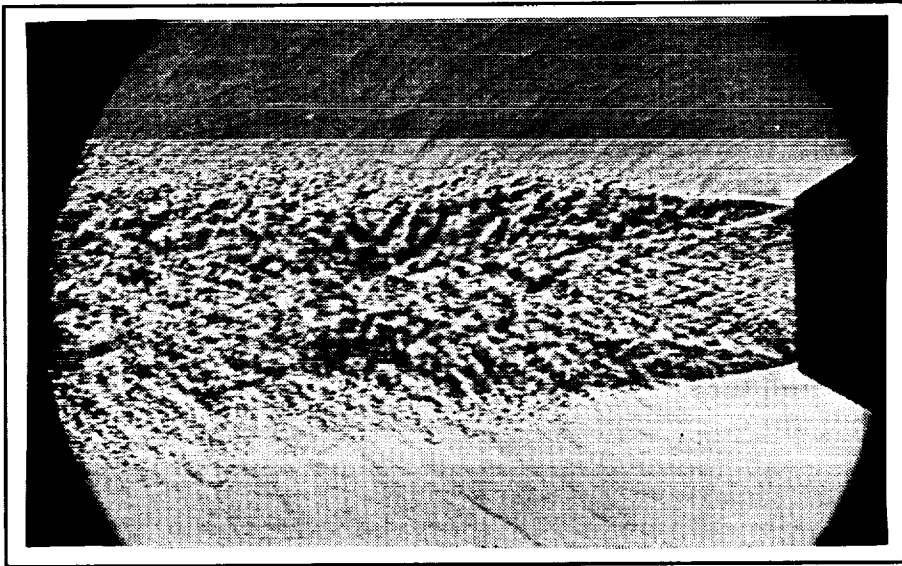
b) Medium Swirl: $P_e = 14.2$ psia

c) High Swirl: $P_e = 15.1$ psia

Figure 4.5: Shadowgraphs for Matched Condition

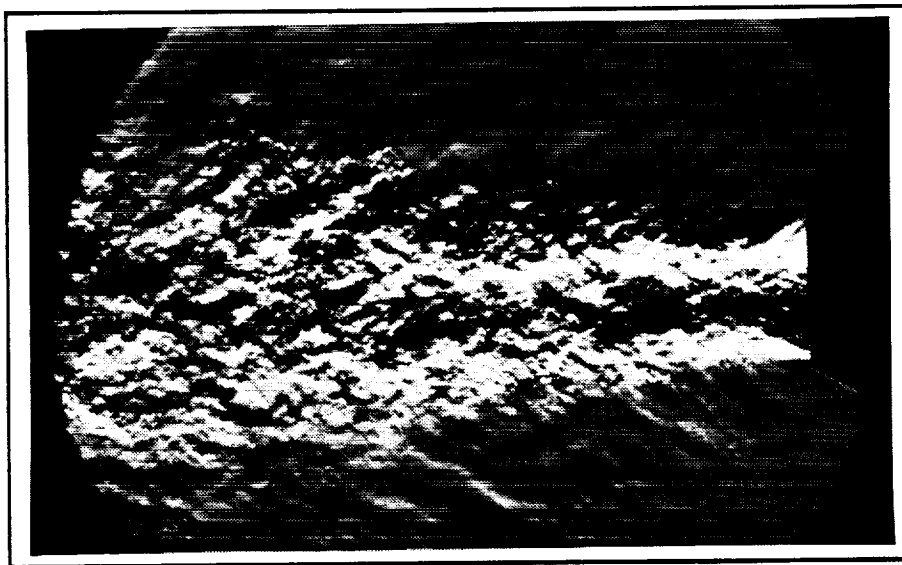


a) No Swirl: $P_e = 22.7$ psia

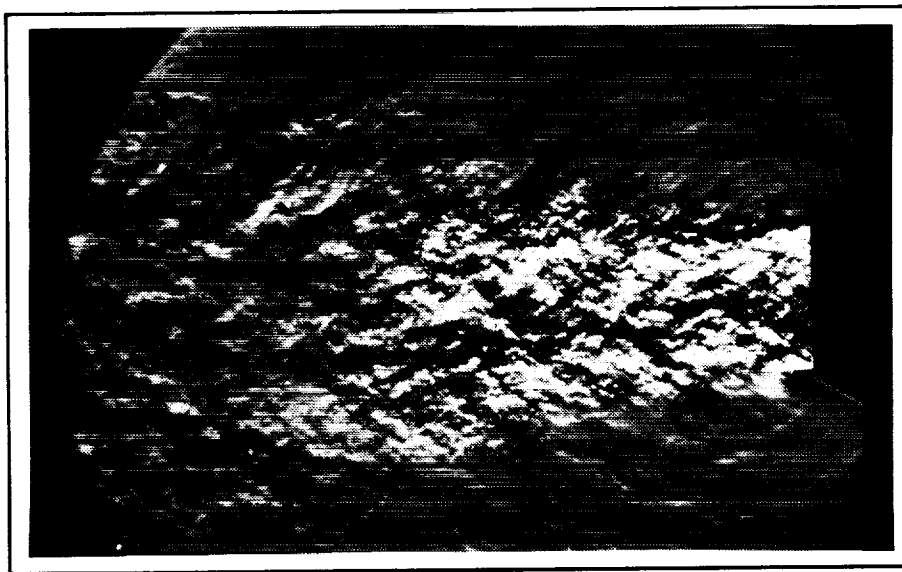


b) Medium Swirl: $P_e = 27.5$ psia

Figure 4.6: Shadowgraphs for Underexpanded Condition

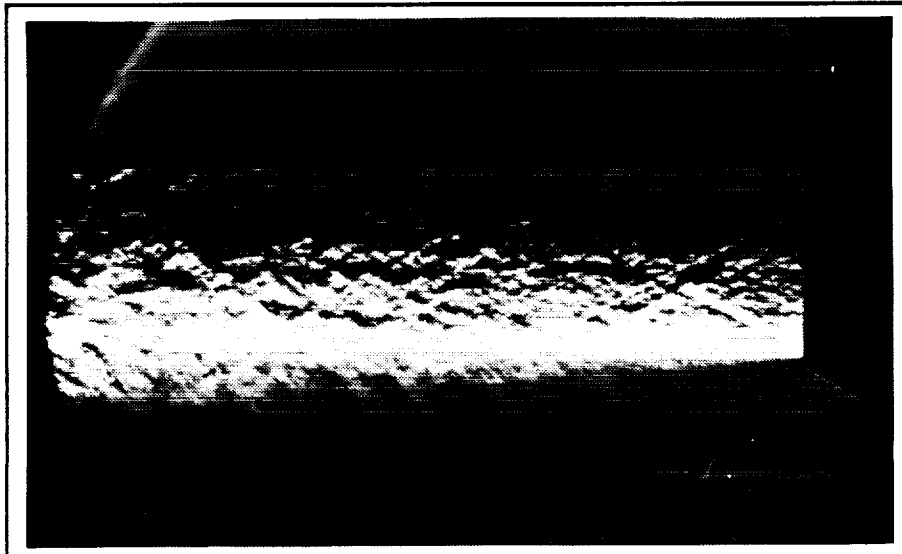


a) Medium Swirl: $P_e = 10.4$ psia

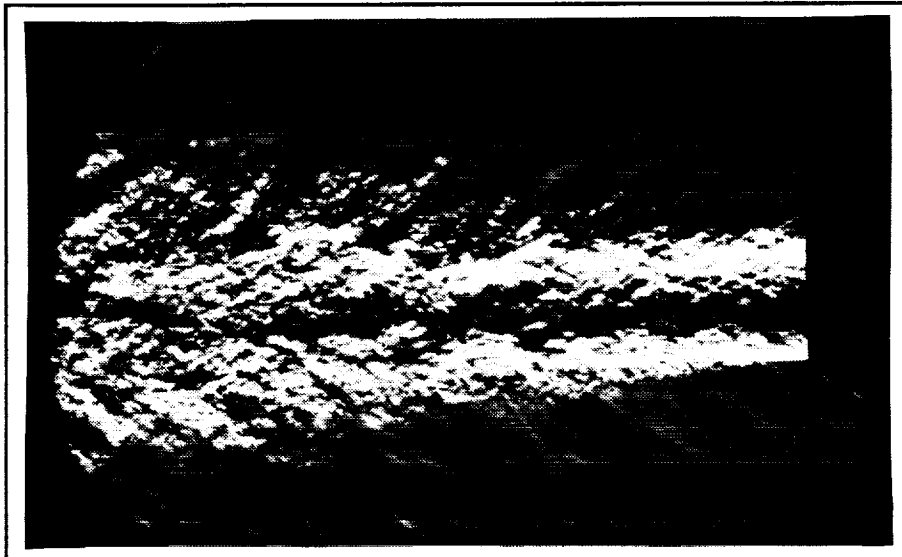


b) High Swirl: $P_e = 9.6$ psia

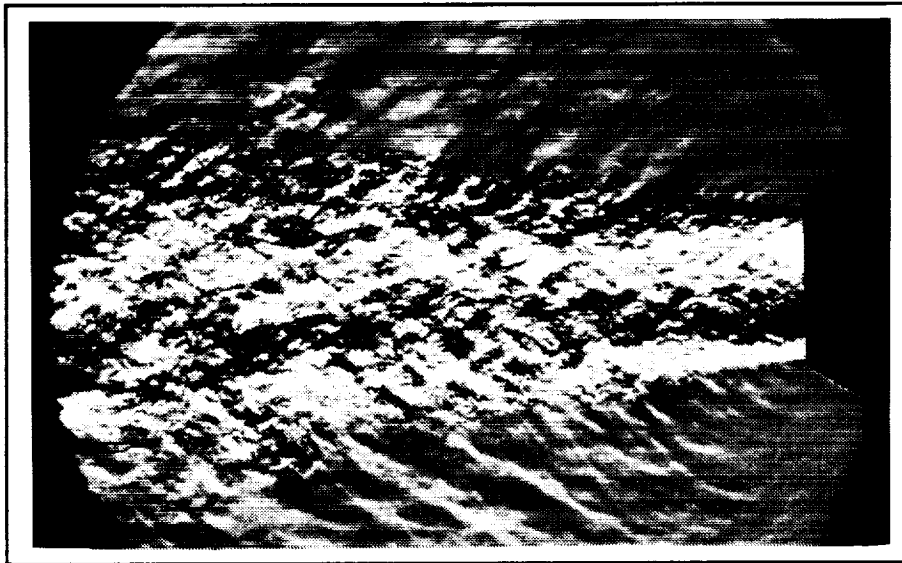
Figure 4.7: Conventional Schlieren with a Vertical Knife Edge for Overexpanded Condition



a) No Swirl: $P_e = 15.9$ psia

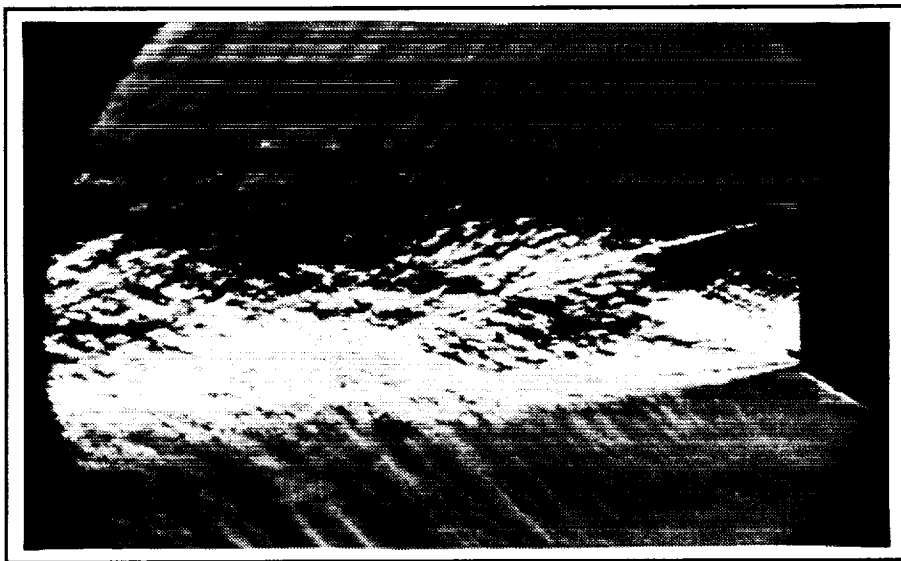


b) Medium Swirl: $P_e = 14.3$ psia

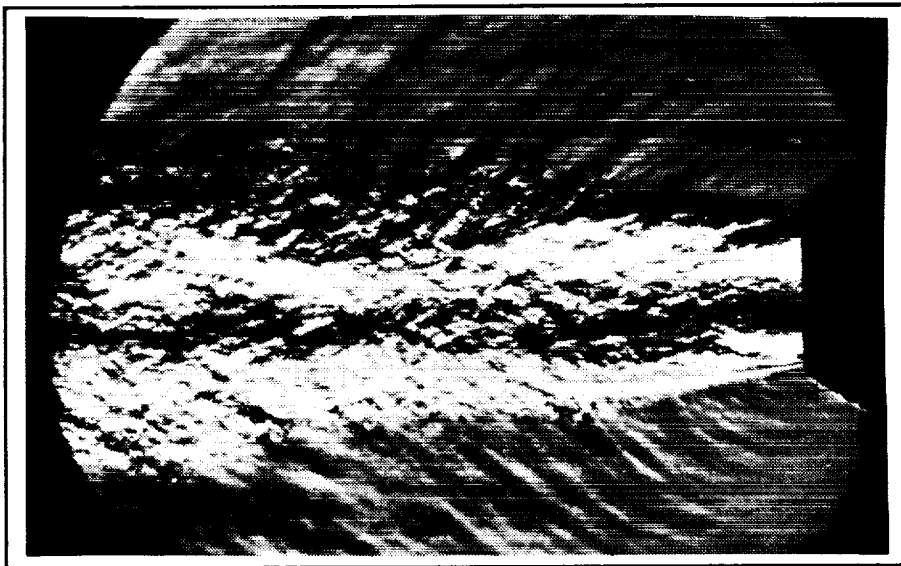


c) High Swirl: $P_e = 15.0$ psia

Figure 4.8: Conventional Schlieren with a Vertical Knife Edge for Matched Condition

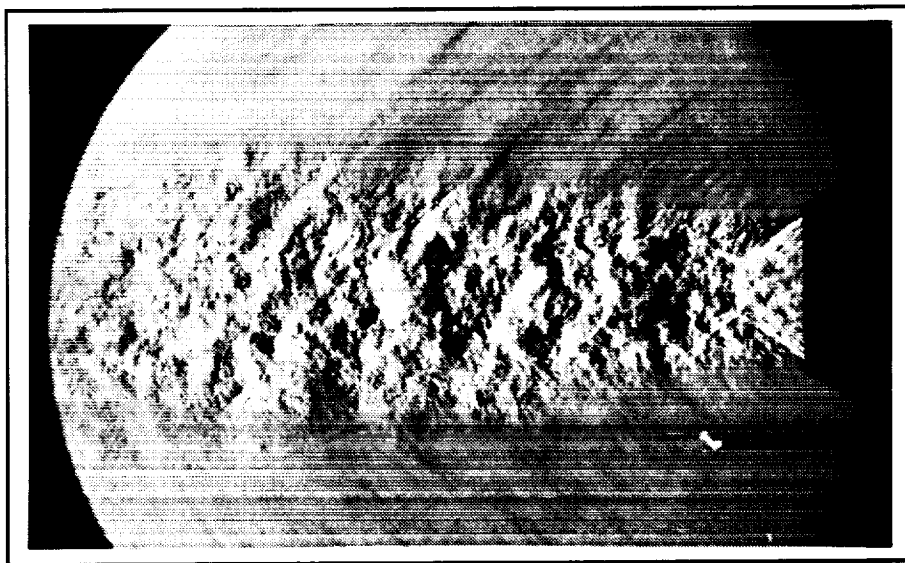


a) No Swirl: $P_e = 25.9$ psia

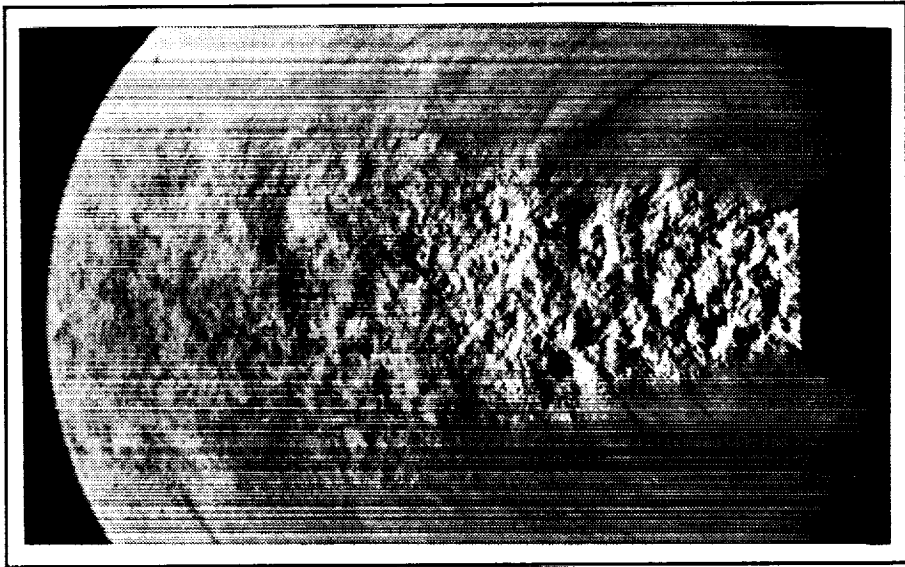


b) Medium Swirl: $P_e = 25.9$ psia

Figure 4.9: Conventional Schlieren with a Vertical Knife Edge for Underexpanded Condition

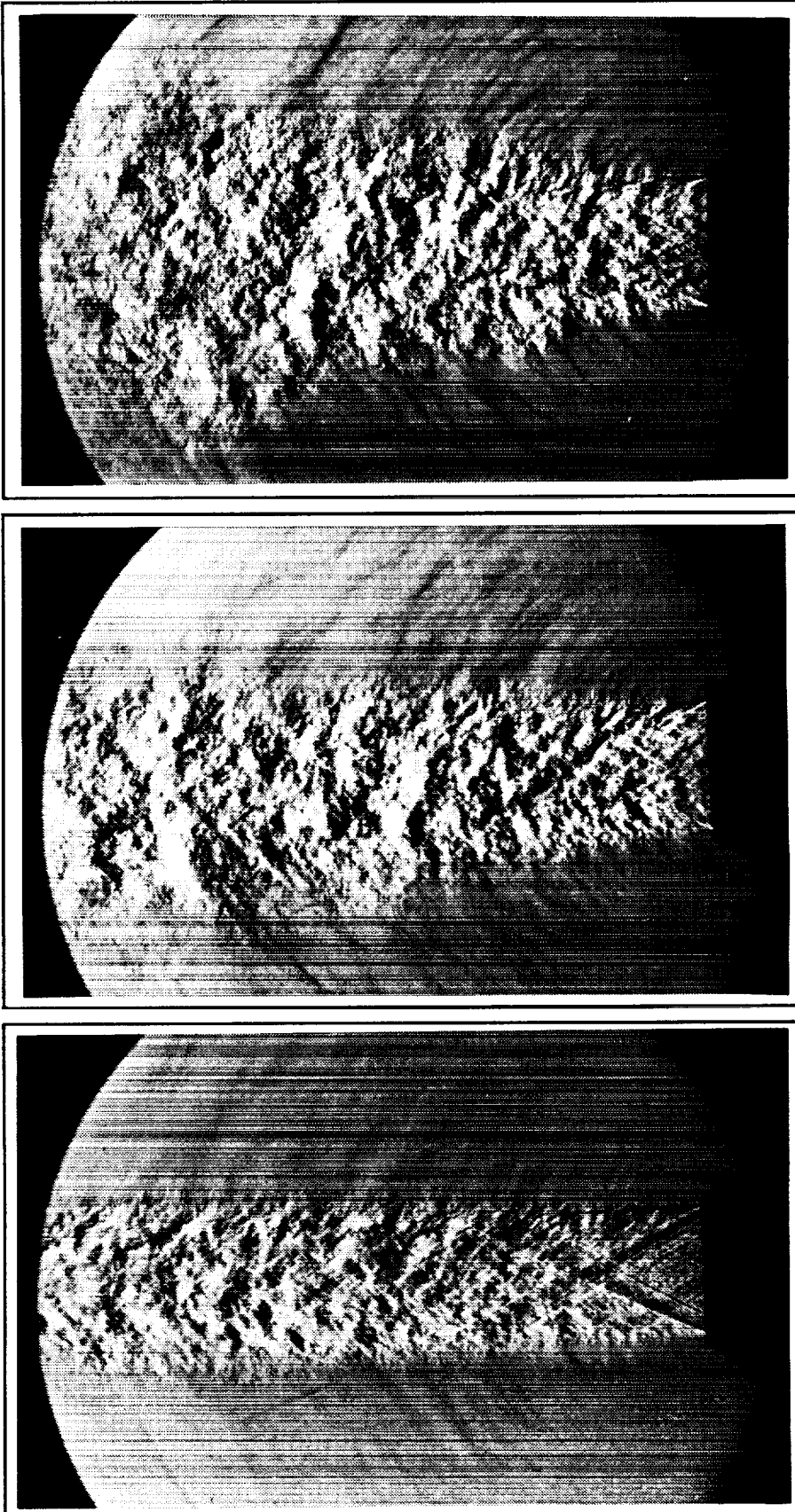


a) Medium Swirl: $P_e = 10.3$ psia



b) High Swirl: $P_e = 9.8$ psia

Figure 4.10: Conventional Schlieren with a Horizontal Knife Edge for Overexpanded Condition

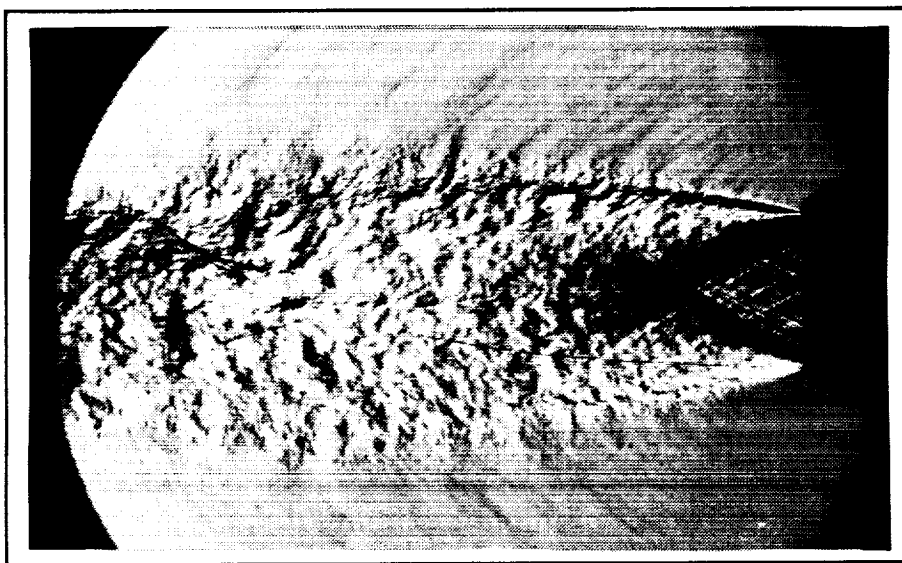


a) No Swirl: $P_e = 16.6$ psia

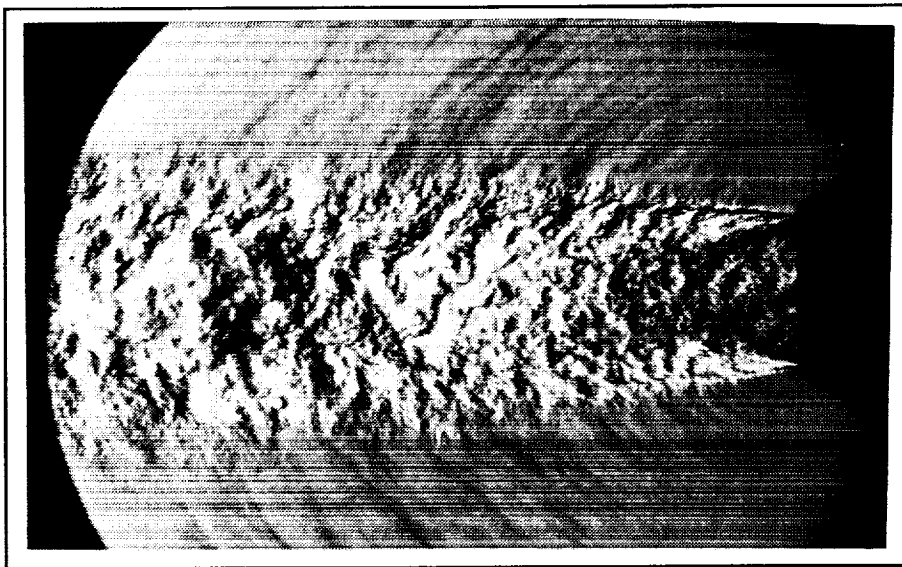
b) Medium Swirl: $P_e = 14.4$ psia

c) High Swirl: $P_e = 14.8$ psia

Figure 4.11: Conventional Schlieren with a Horizontal Knife Edge for Matched Condition

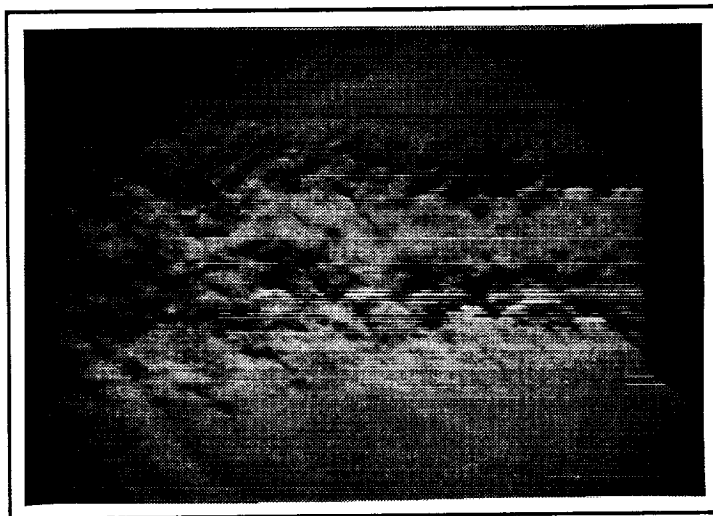


a) No Swirl: $P_e = 38.6$ psia

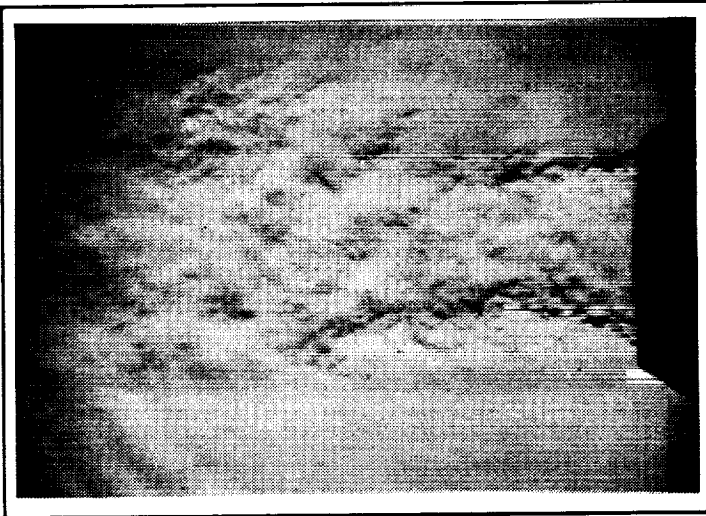


b) Medium Swirl: $P_e = 27.2$ psia

Figure 4.12: Conventional Schlieren with a Horizontal Knife Edge for Underexpanded Condition

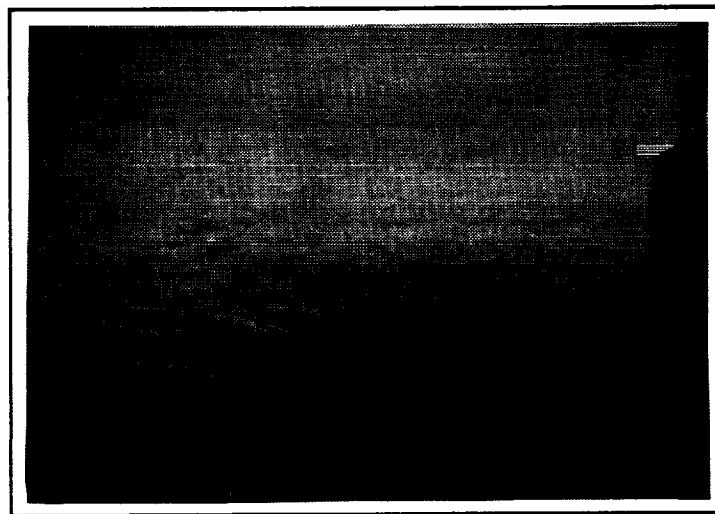


a) Medium Swirl: $P_e = 9.9$ psia

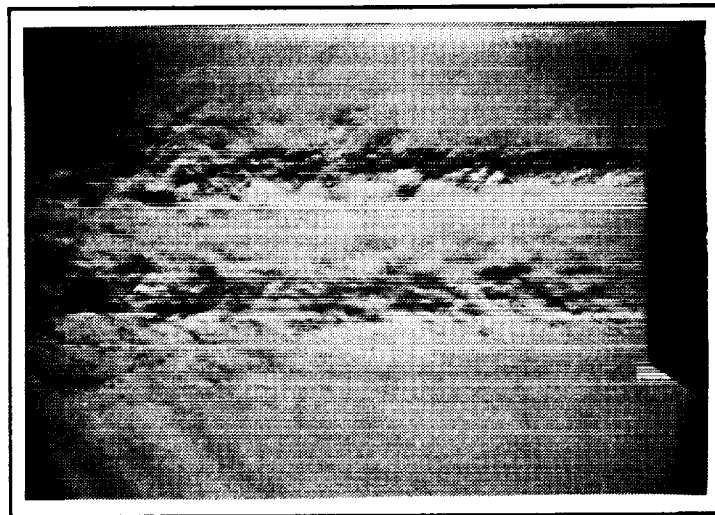


b) High Swirl: $P_e = 9.9$ psia

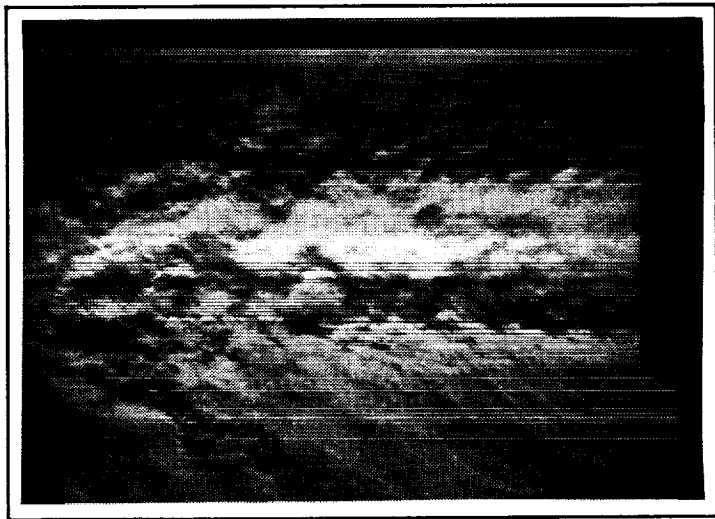
Figure 4.13: Focusing Schlieren with a Vertical Knife Edge for Overexpanded Condition



a) No Swirl: $P_e = 14.7$ psia

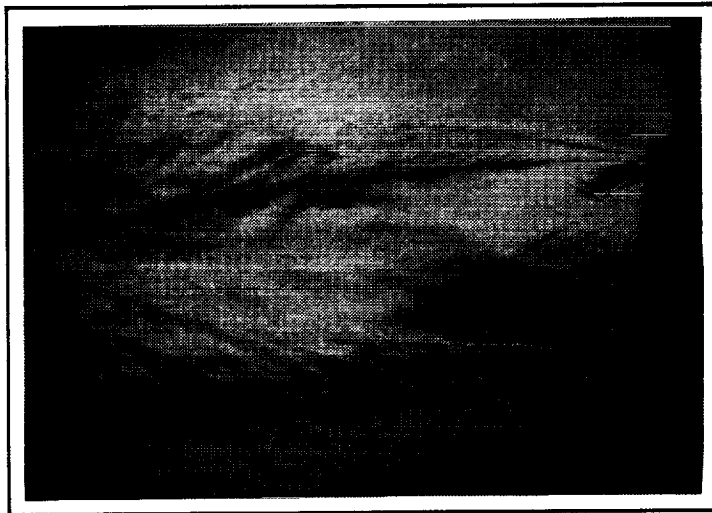


b) Medium Swirl: $P_e = 14.4$ psia

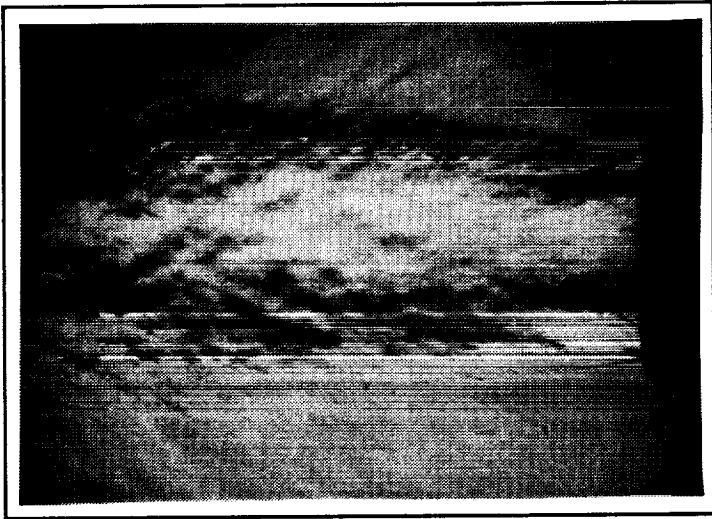


c) High Swirl: $P_e = 14.7$ psia

Figure 4.14: Focusing Schlieren with a Vertical Knife Edge for Matched Condition

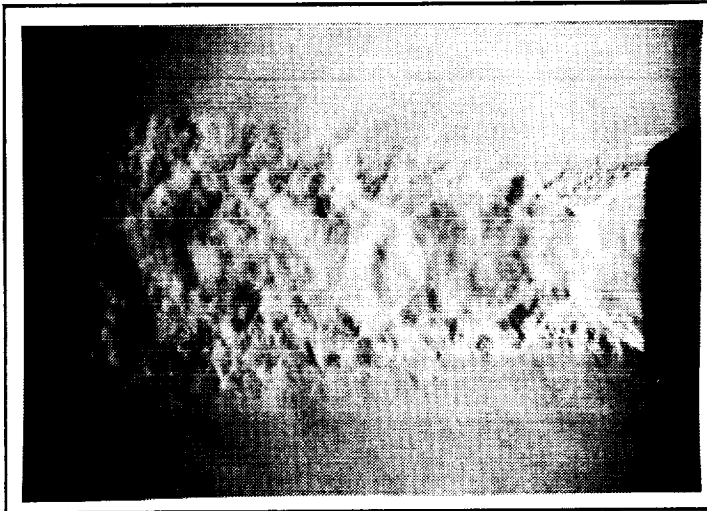


a) No Swirl: $P_e = 38.1$ psia

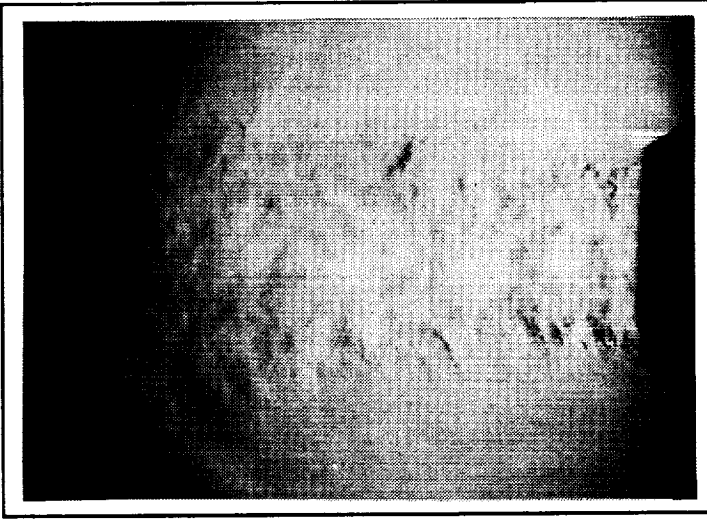


b) Medium Swirl: $P_e = 27.9$ psia

Figure 4.15: Focusing Schlieren with a Vertical Knife Edge for Underexpanded Condition

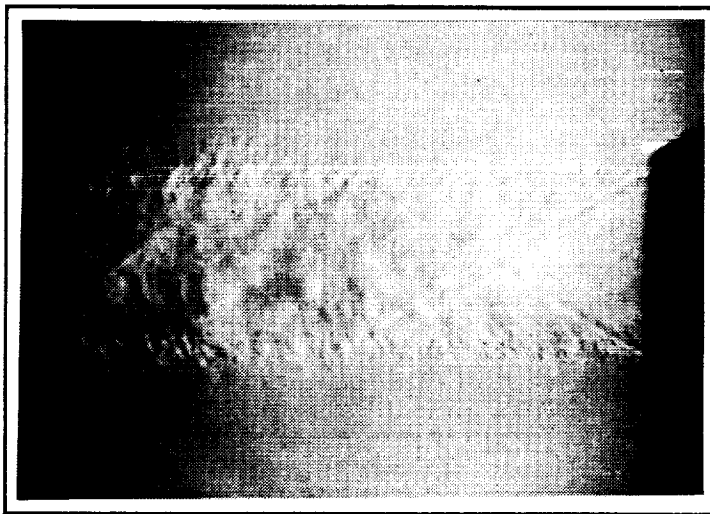


a) Medium Swirl: $P_e = 9.5$ psia

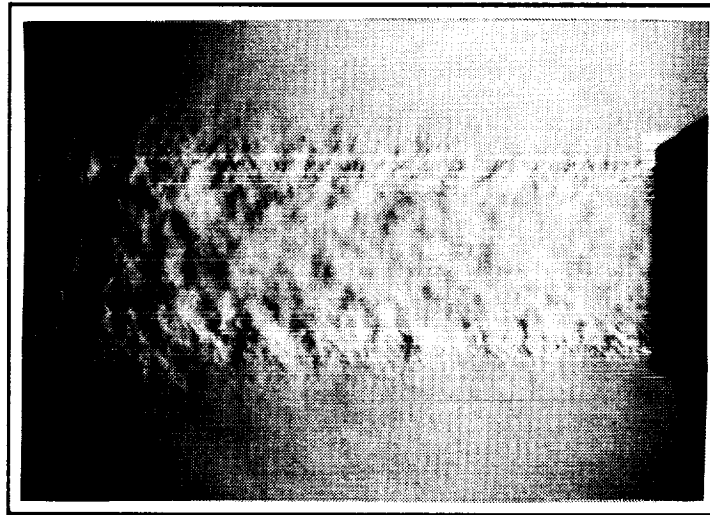


b) High Swirl: $P_e = 9.9$ psia

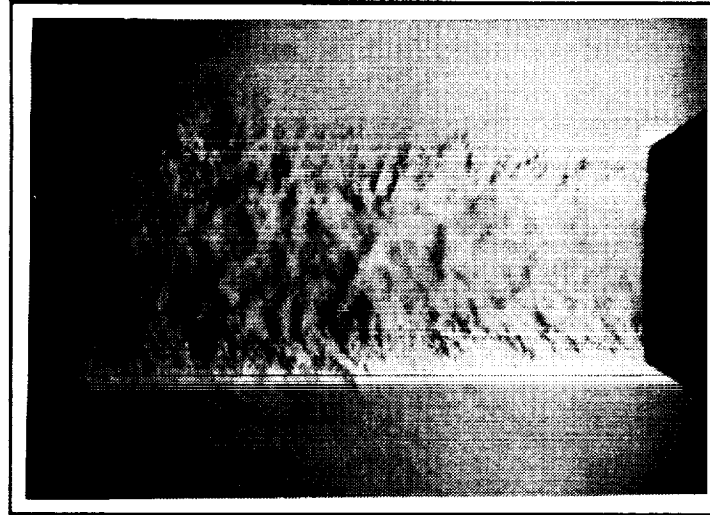
Figure 4.16: Focusing Schlieren with a Horizontal Knife Edge for Overexpanded Condition



a) No Swirl: $P_e = 14.2$ psia

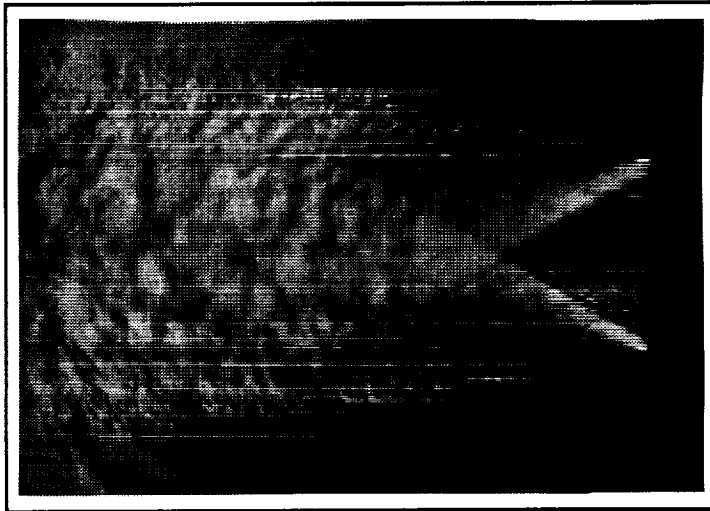


b) Medium Swirl: $P_e = 14.4$ psia

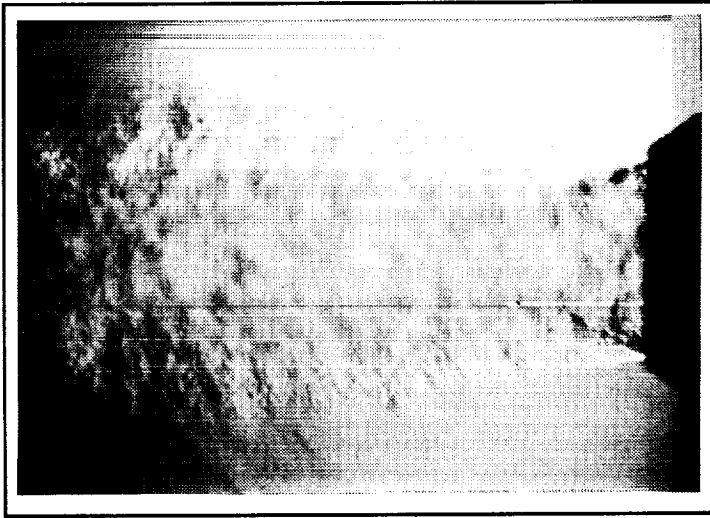


c) High Swirl: $P_e = 14.8$ psia

Figure 4.17: Focusing Schlieren with a Horizontal Knife Edge for Matched Condition



a) No Swirl: $P_e = 38.1$ psia



b) Medium Swirl: $P_e = 27.7$ psia

Figure 4.18: Focusing Schlieren with a Horizontal Knife Edge for Underexpanded Condition

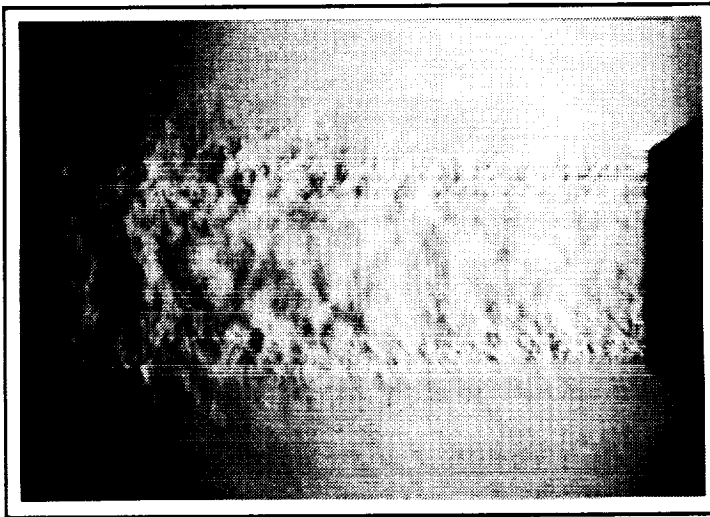
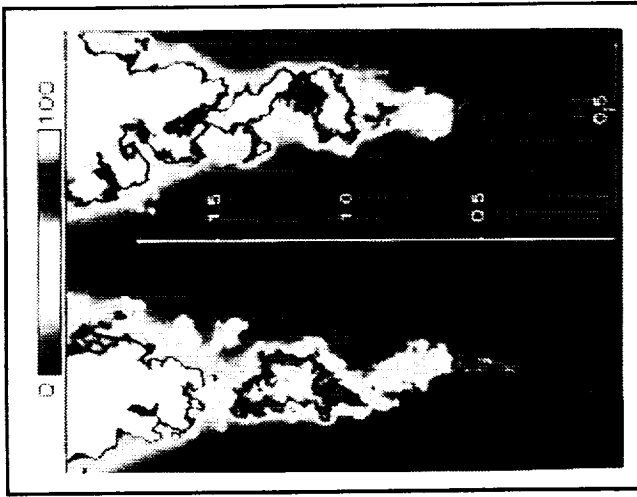
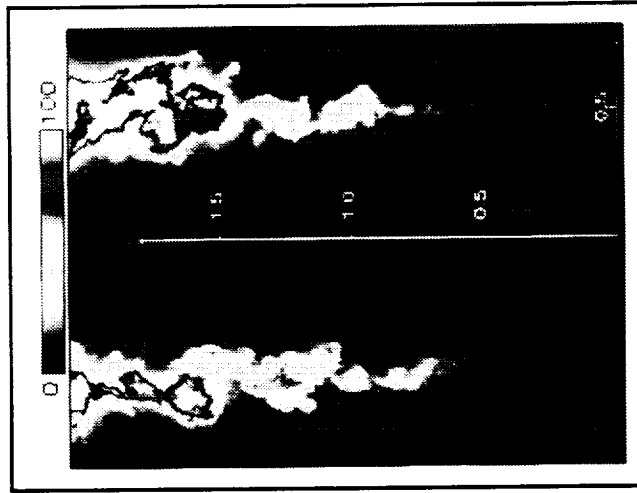


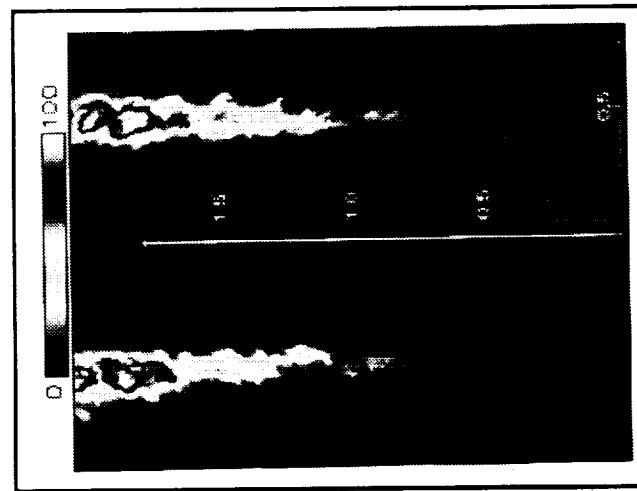
Figure 4.19: Focusing Schlieren with a Horizontal Knife Edge for Underexpanded Condition at Low Swirl ($P_e = 15.1$ psia)



c) High Swirl: $P_e = 14.7$ psia



b) Low Swirl: $P_e = 14.7$ psia



a) No Swirl: $P_e = 14.7$ psia

Figure 4.20: Rayleigh Scattering from a Laser Light Sheet Showing Condensation in the Shear Layer for Matched Condition

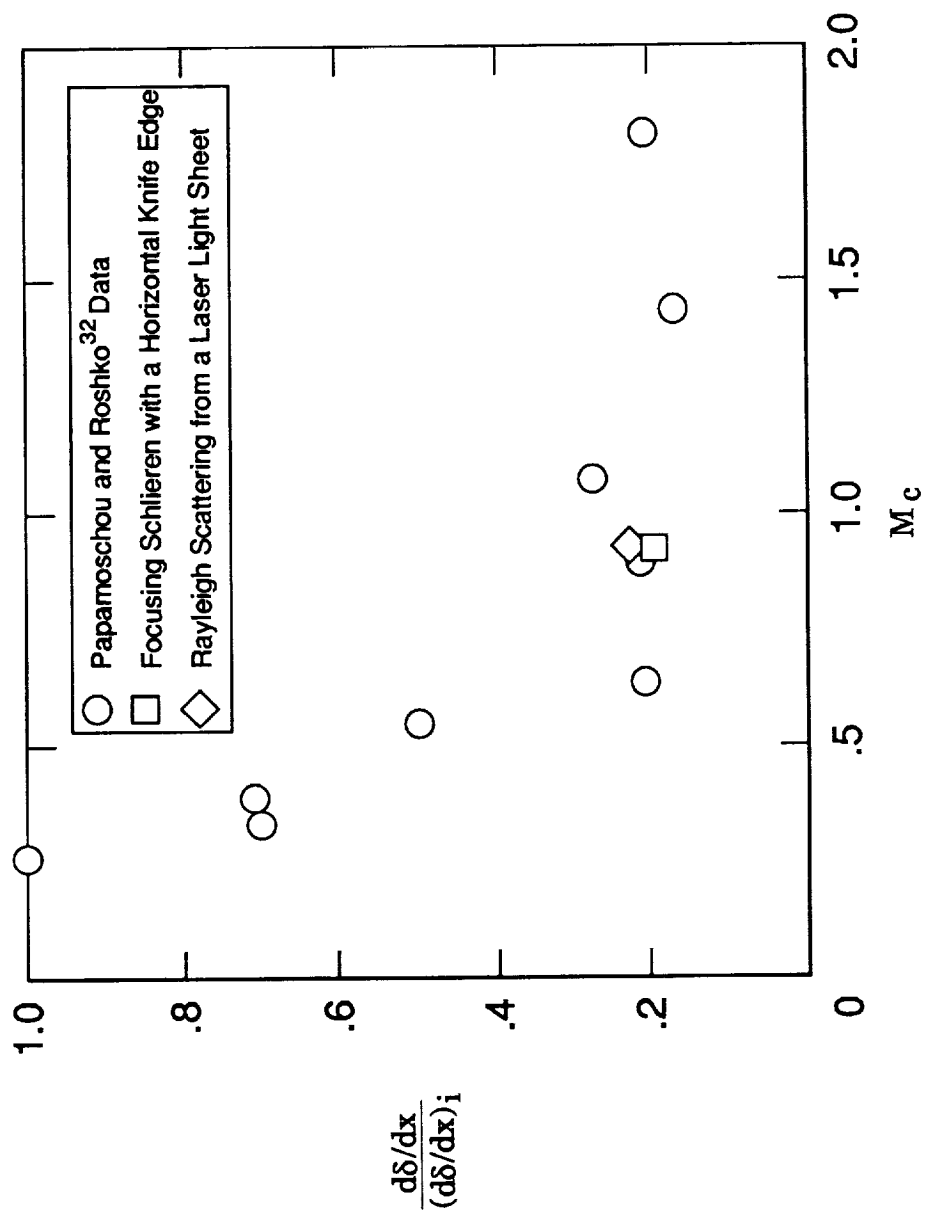


Figure 4.21: Normalized Shear Layer Growth Rate as a Function of Calculated Convective Mach Number

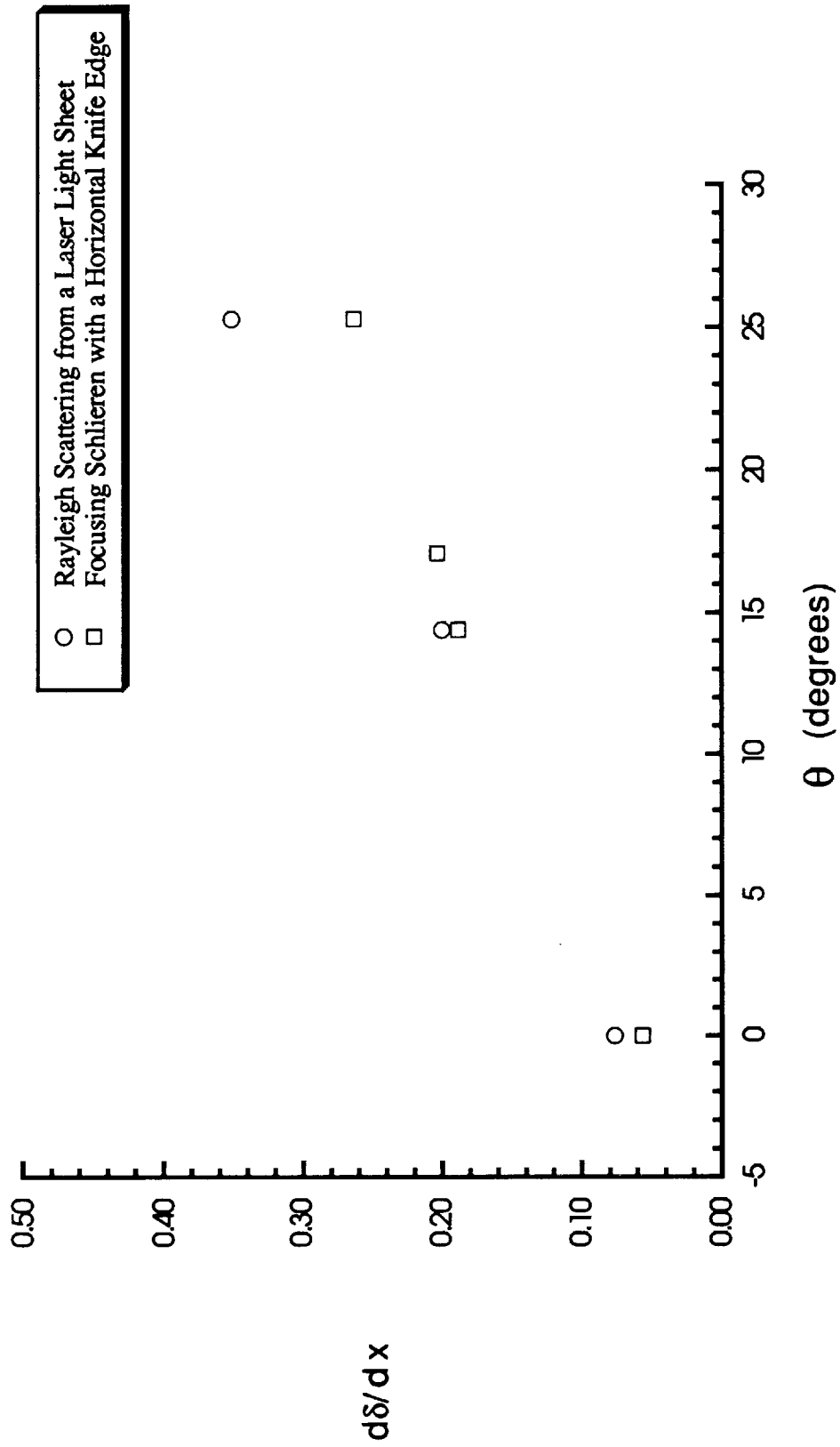


Figure 4.22: Shear Layer Growth Rate as a Function of Helix Angle Extrapolated to the Edge of the Jet

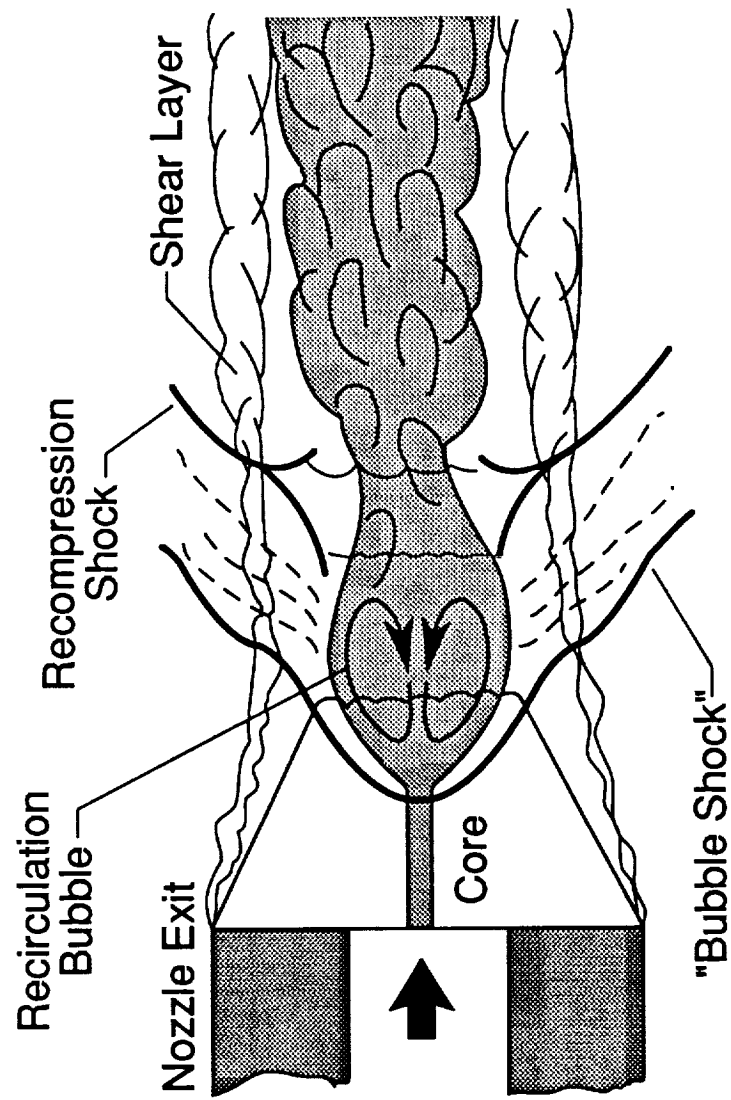
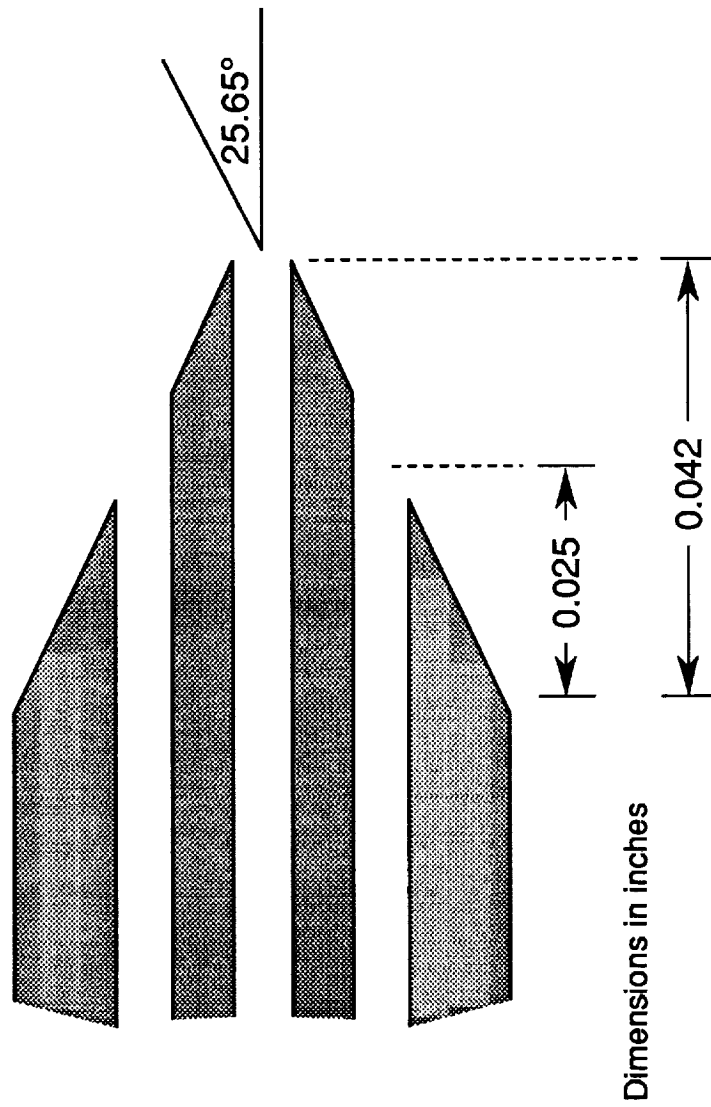
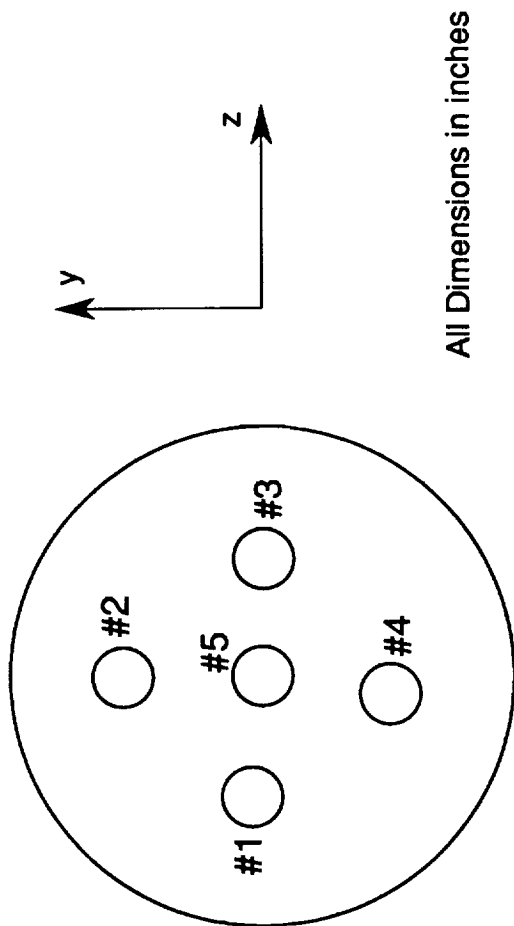


Figure 4.23: Hypothetical Flow Model of Vortex Breakdown at Supersonic Speeds



a: Side View of Tip

Figure 5.1: Illustration of Five Hole Probe



Hole #	Diameter	z-Coordinate	y-Coordinate
1	0.005	-0.014	0.001
2	0.005	-0.001	0.014
3	0.005	0.012	0.0
4	0.005	-0.002	-0.013
5	0.006	0	0

b: Top View of Tip

Figure 5.1 continued

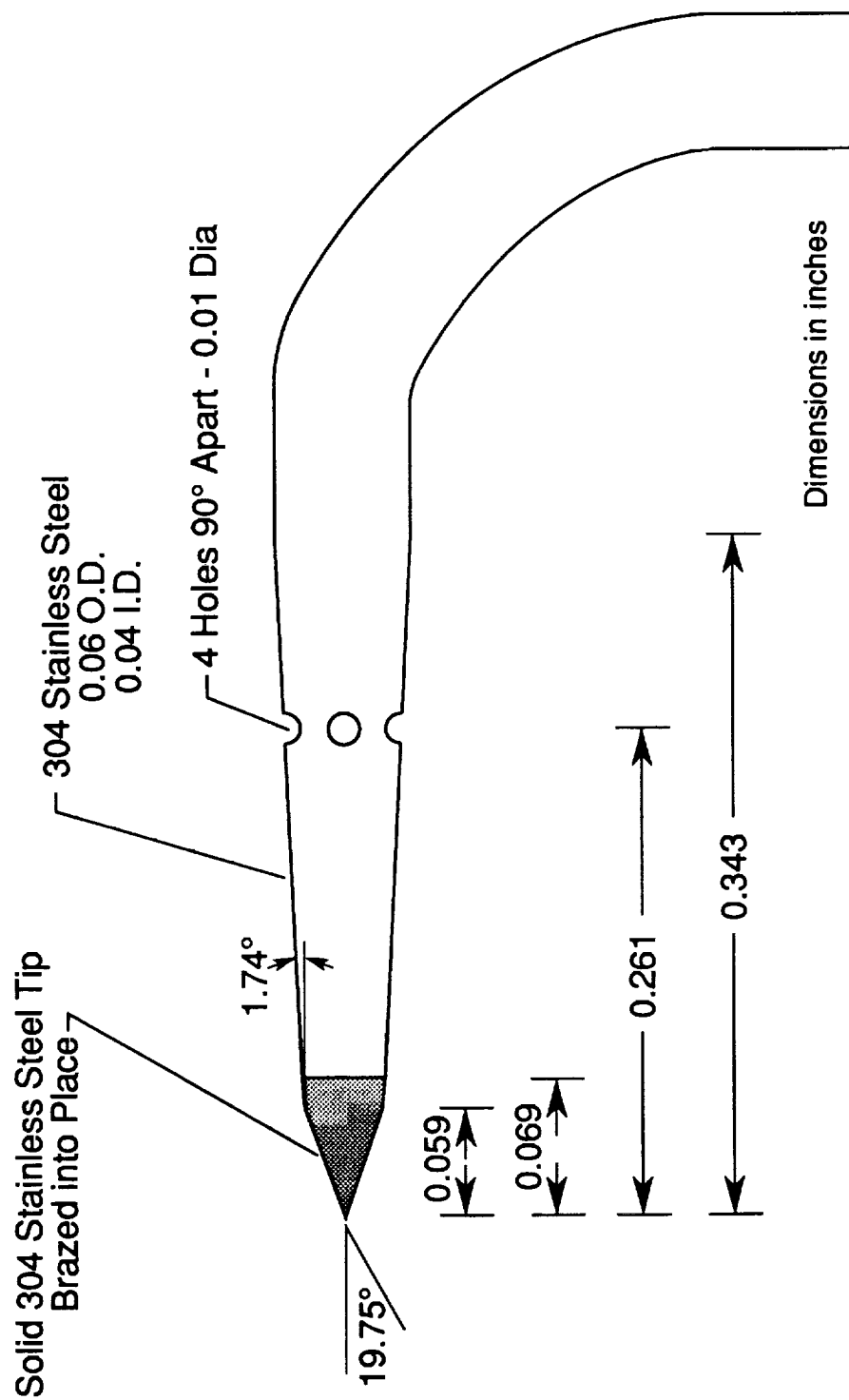
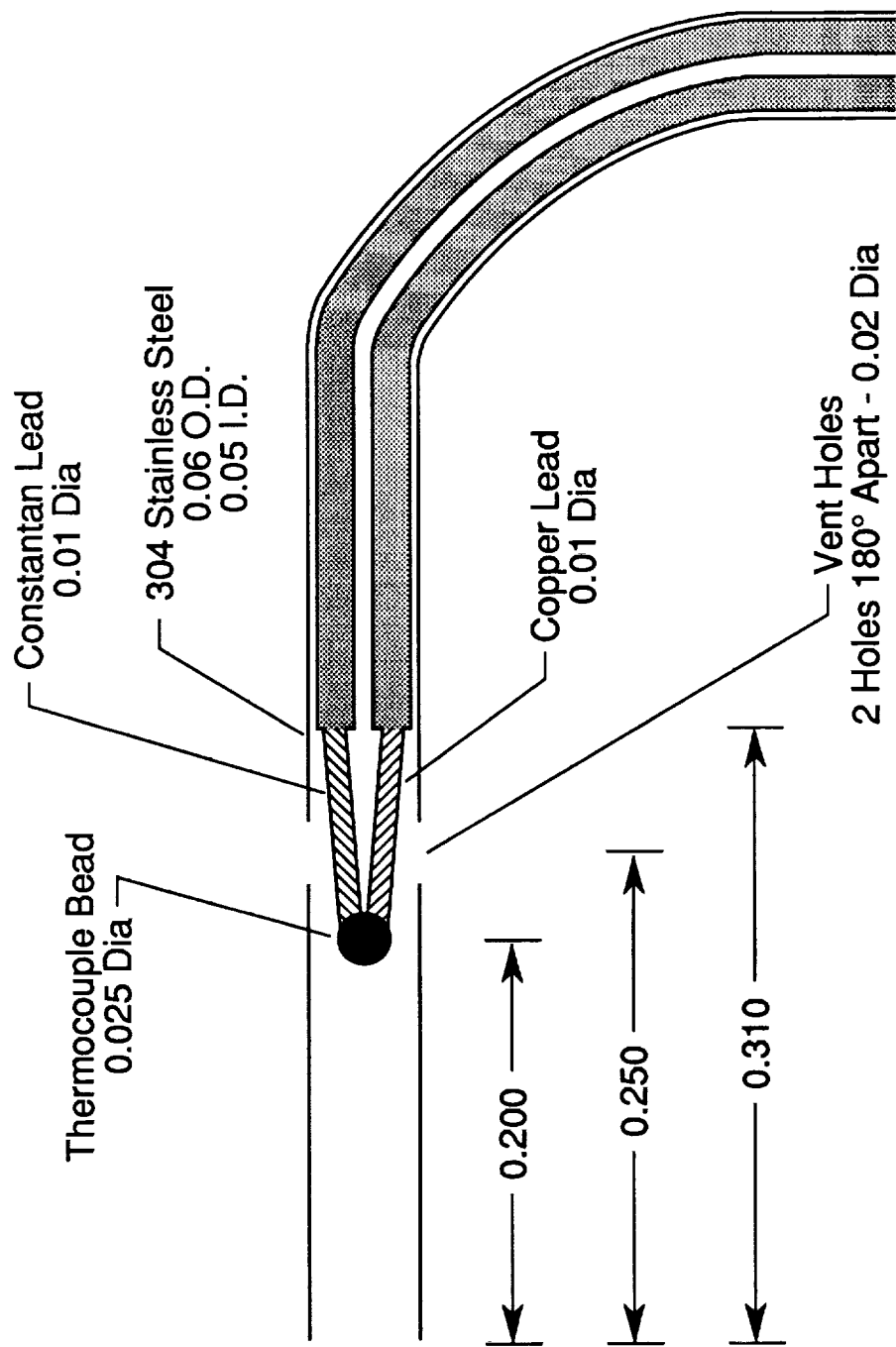


Figure 5.2: Illustration of Static Pressure Probe



Dimensions in inches

Figure 5.3: Illustration of Total Temperature Probe

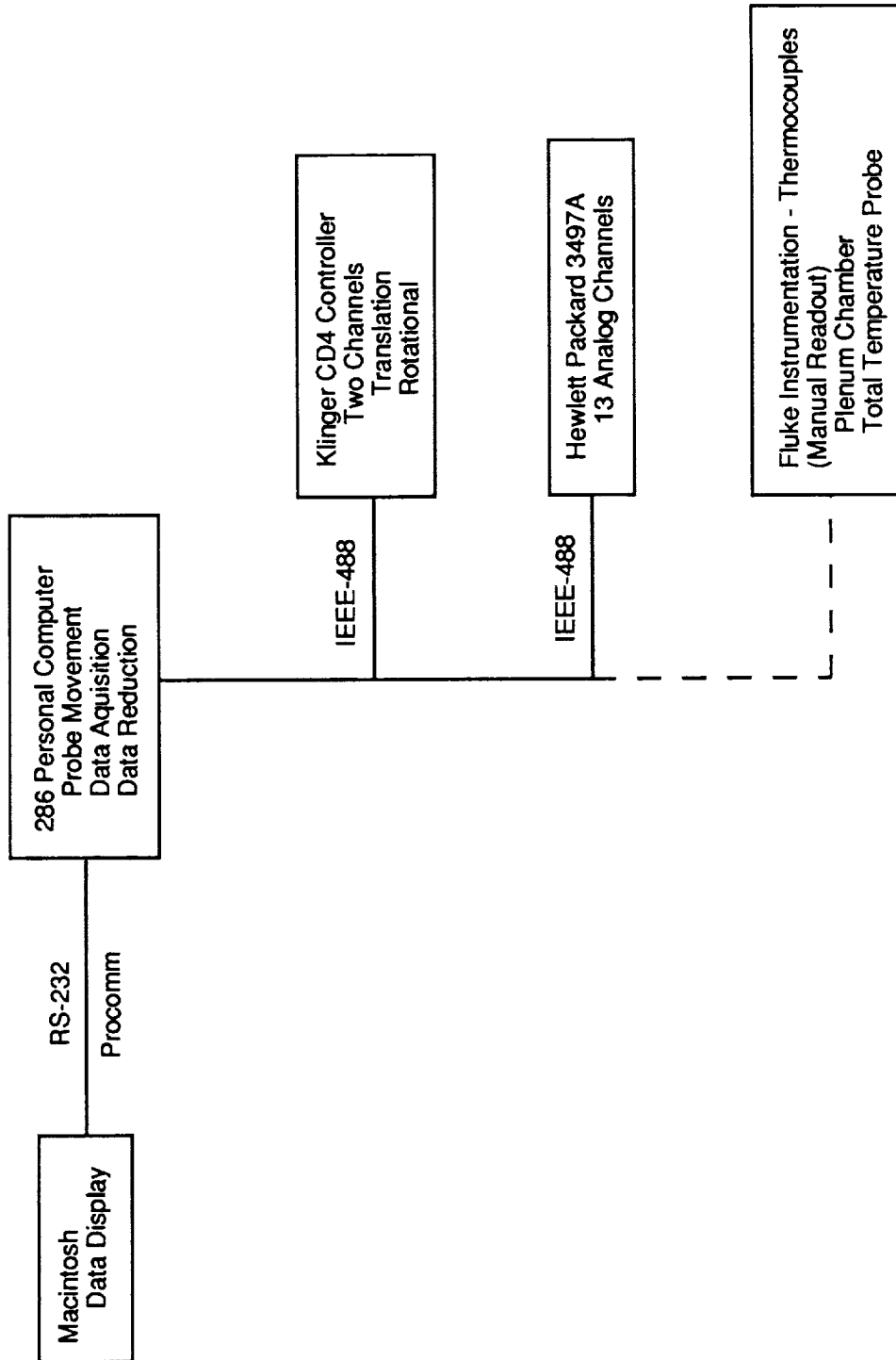


Figure 5.4: Block Diagram of Data Acquisition

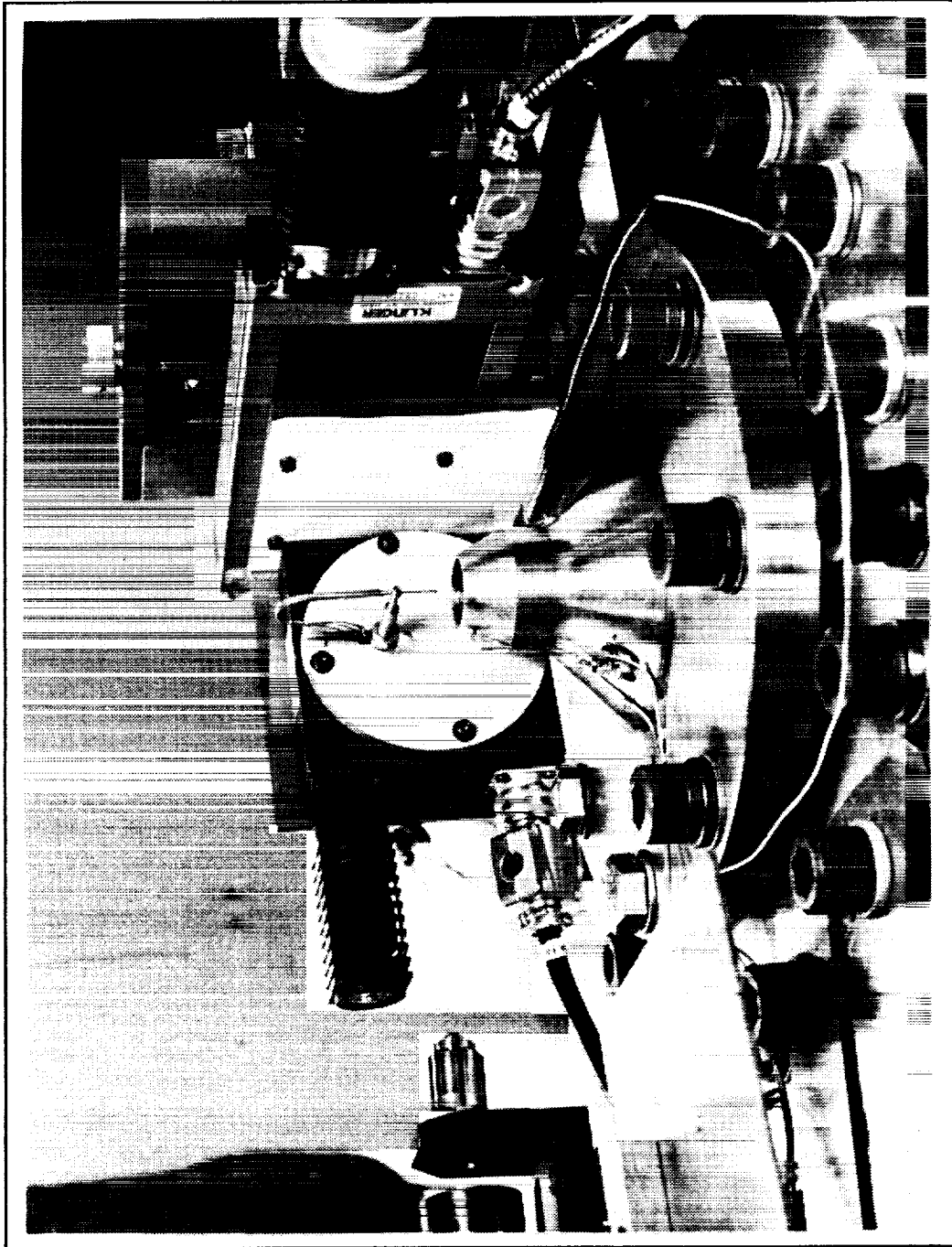


Figure 5.5: Photograph of Vortical Flow Apparatus with Probe

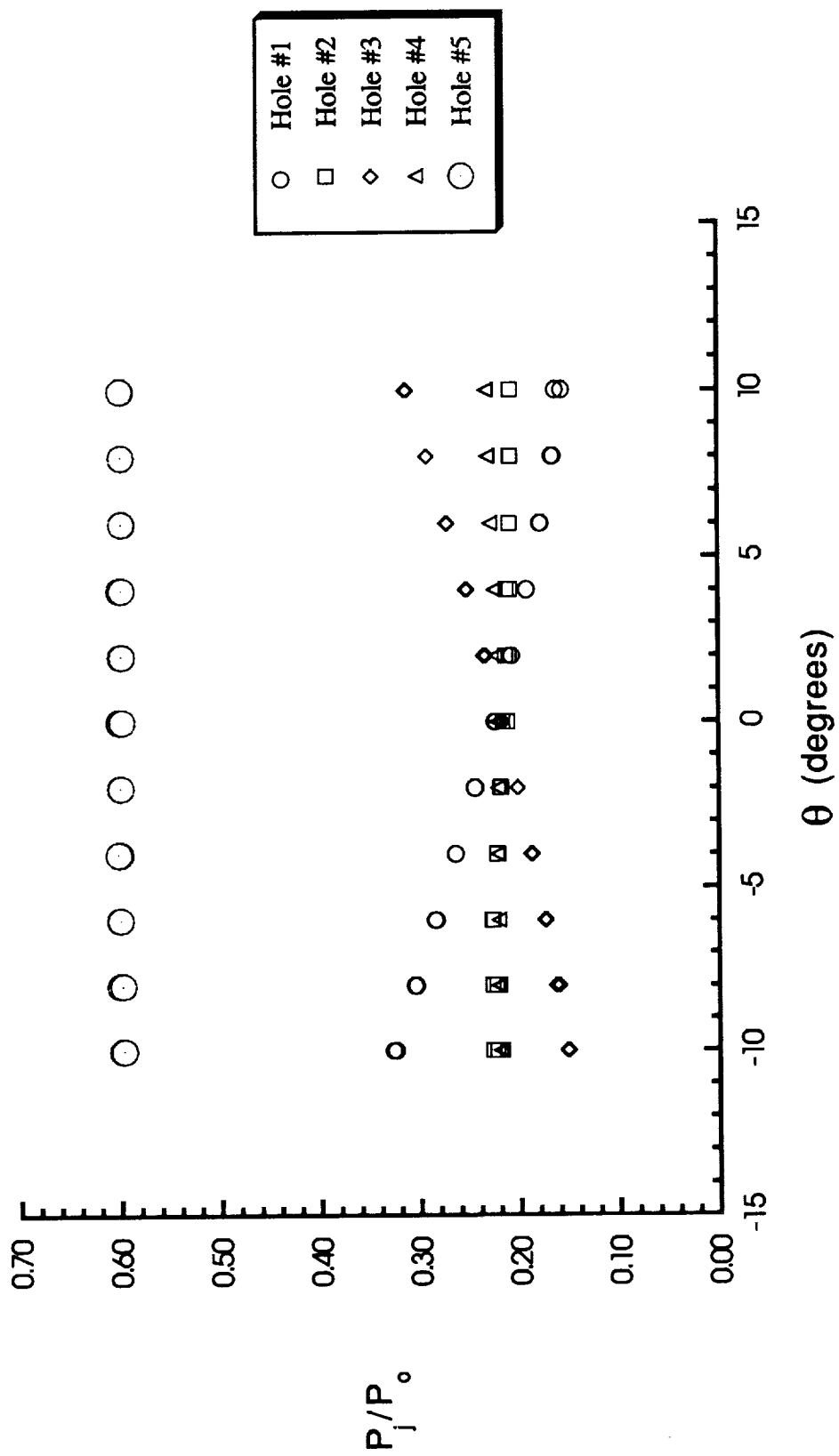


Figure 5.6: P_j/P_o as a Function of Yaw Angle at $r = 0$ for No Swirl

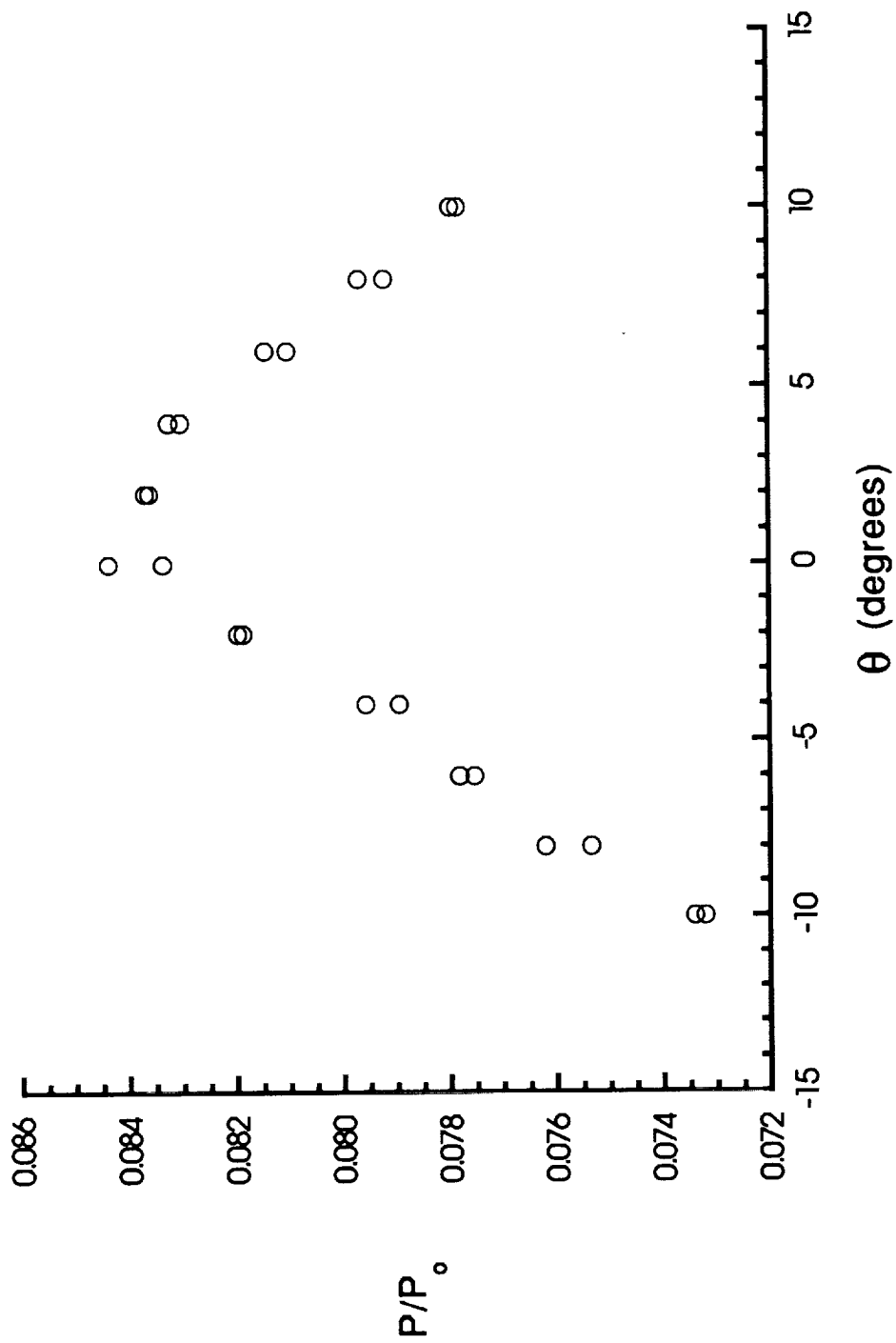


Figure 5.7: Static Pressure as a Function of Yaw Angle at $r = 0$ for No Swirl

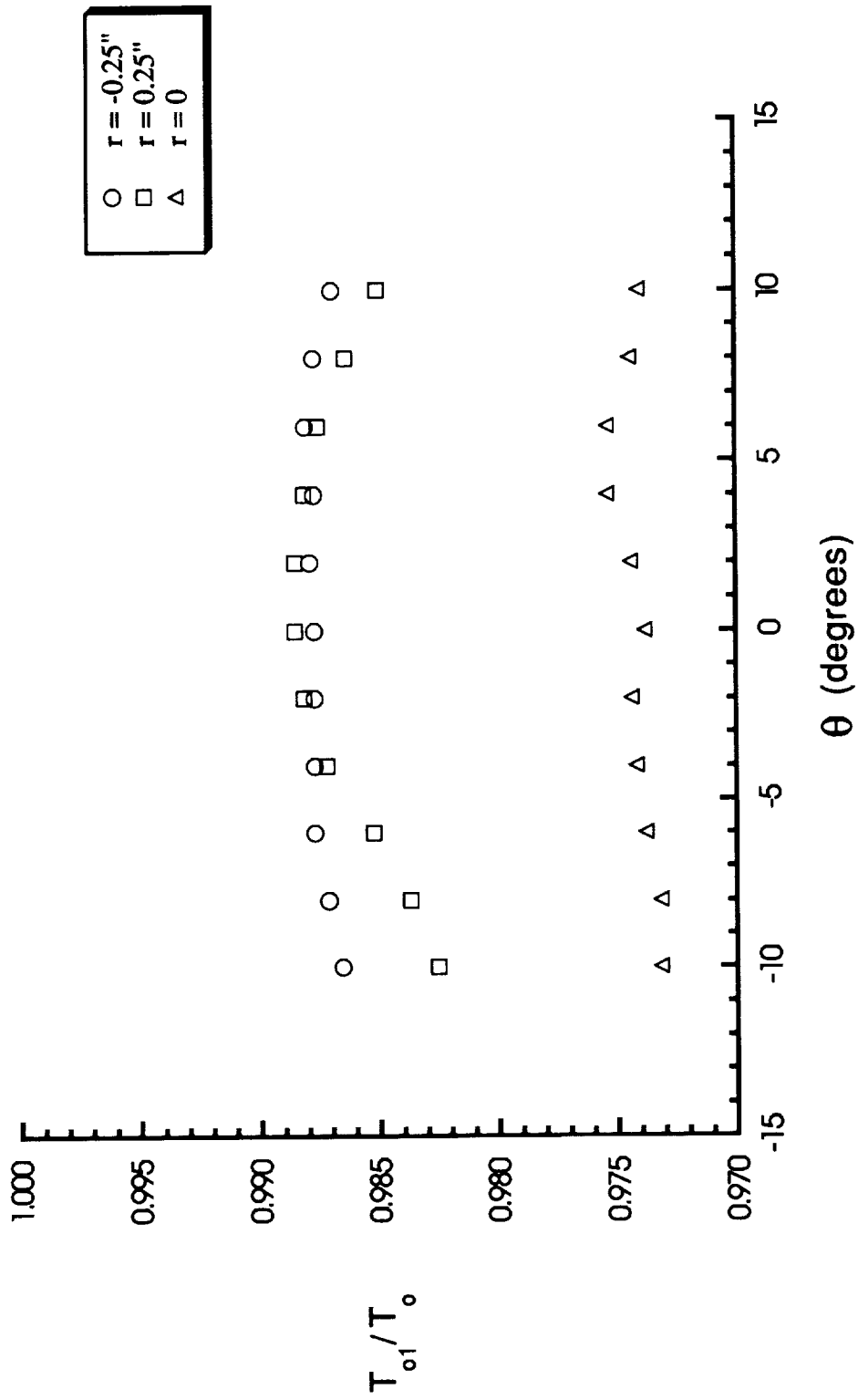


Figure 5.8: Total Temperature as a Function of Yaw Angle at Various Radial Distances for No Swirl

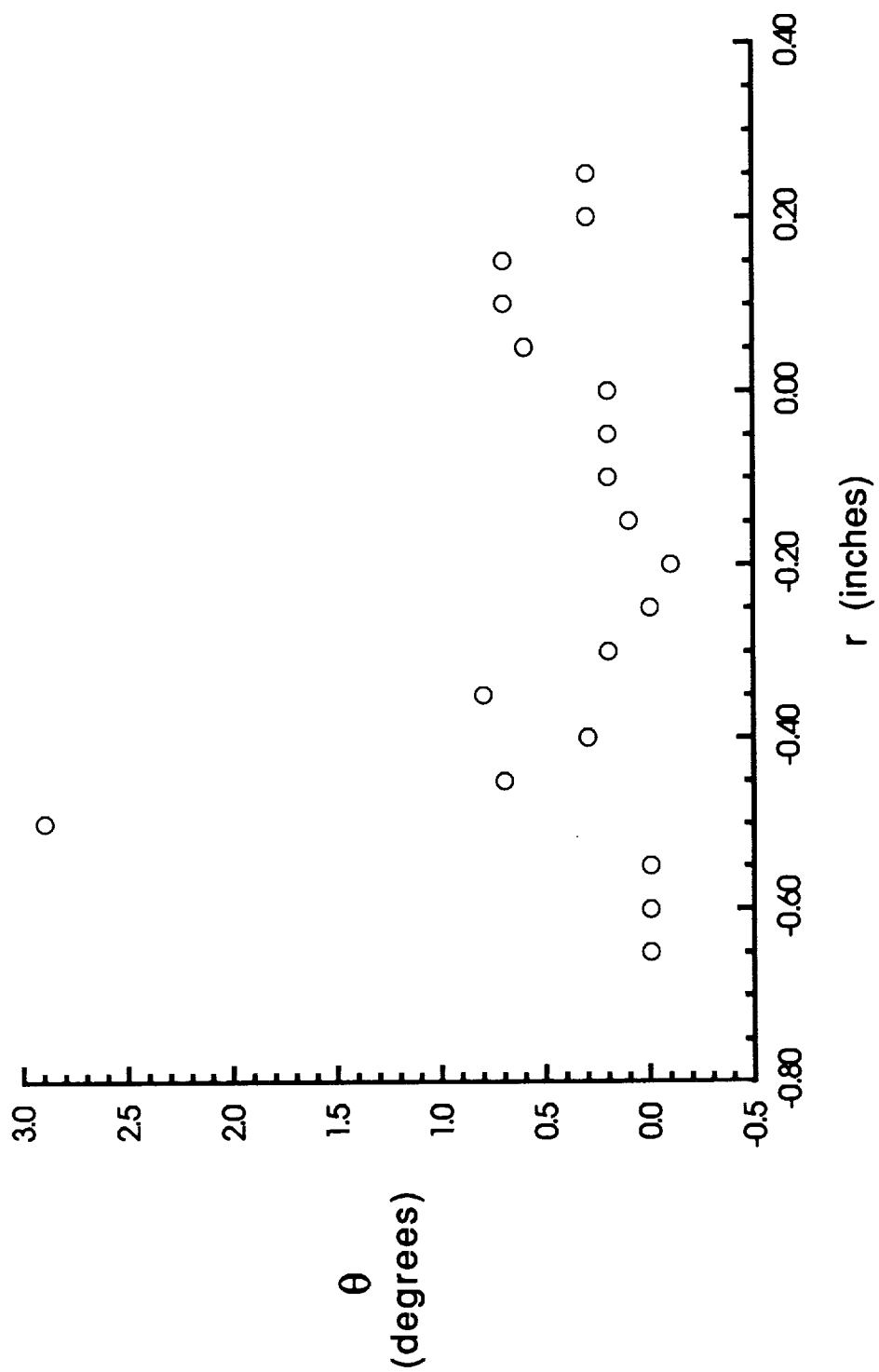


Figure 5.9: Helix Angle as a Function of Radial Distance for No Swirl

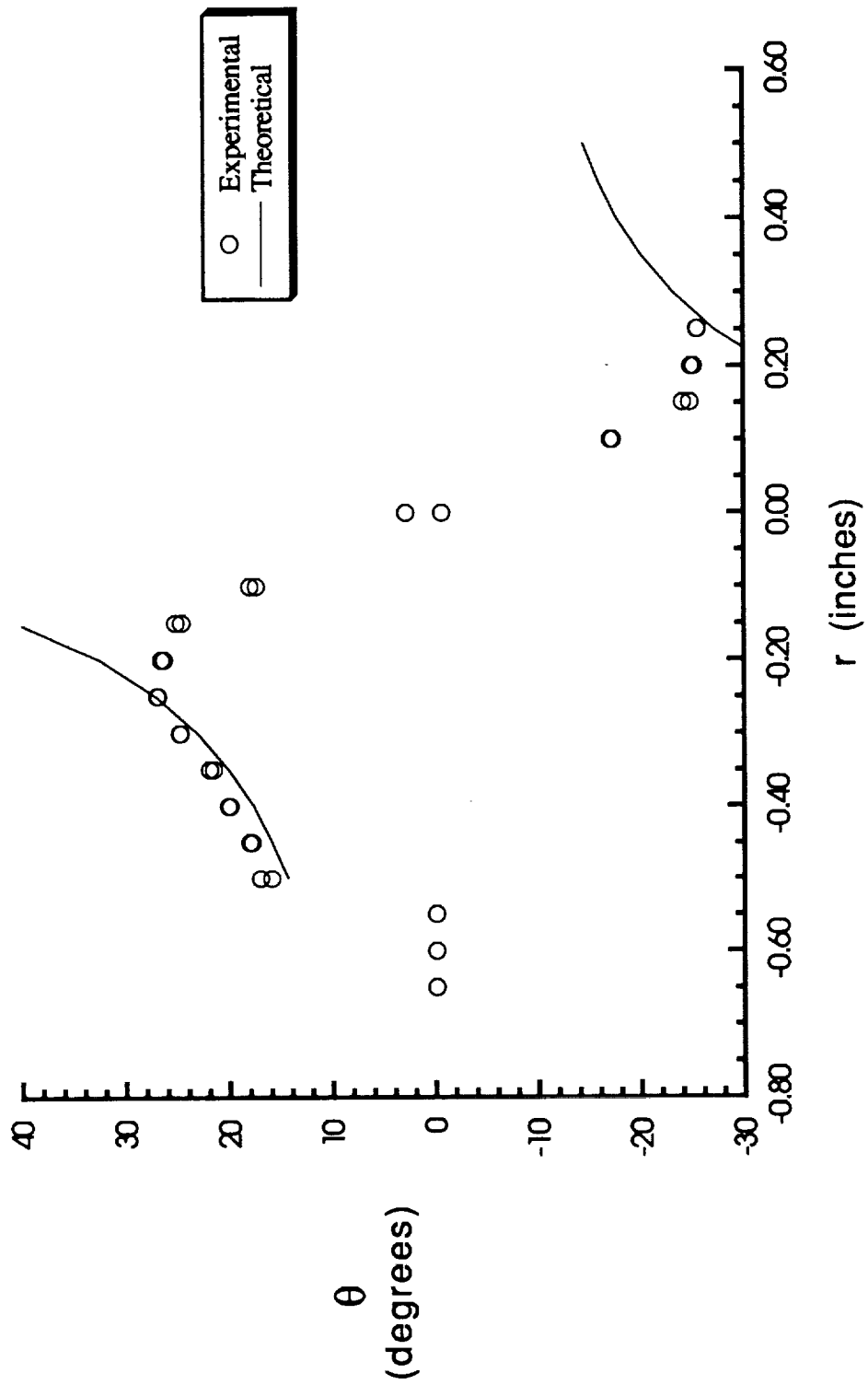


Figure 5.10: Helix Angle as a Function of Radial Distance for Low Swirl

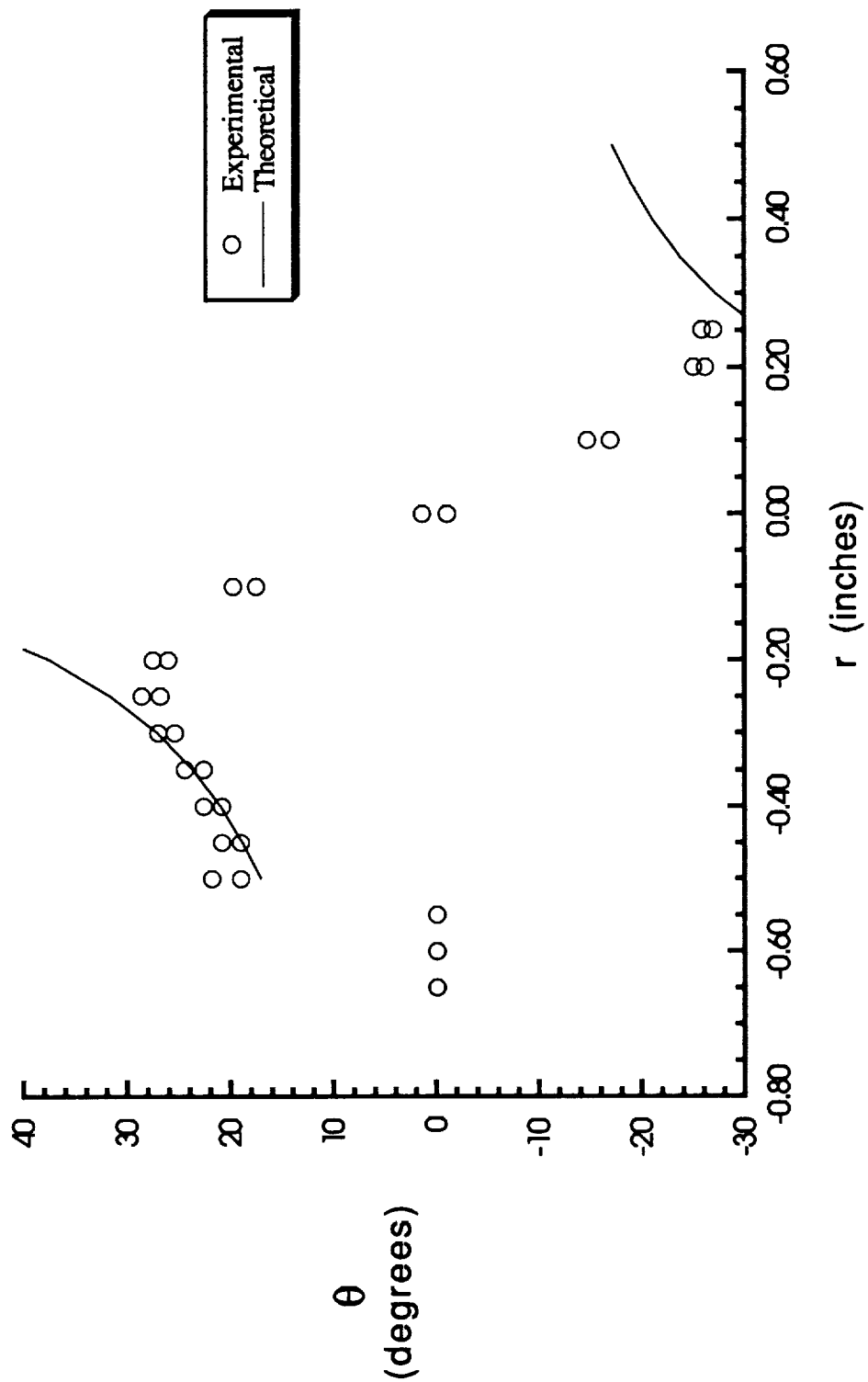


Figure 5.11: Helix Angle as a Function of Radial Distance for Medium Swirl

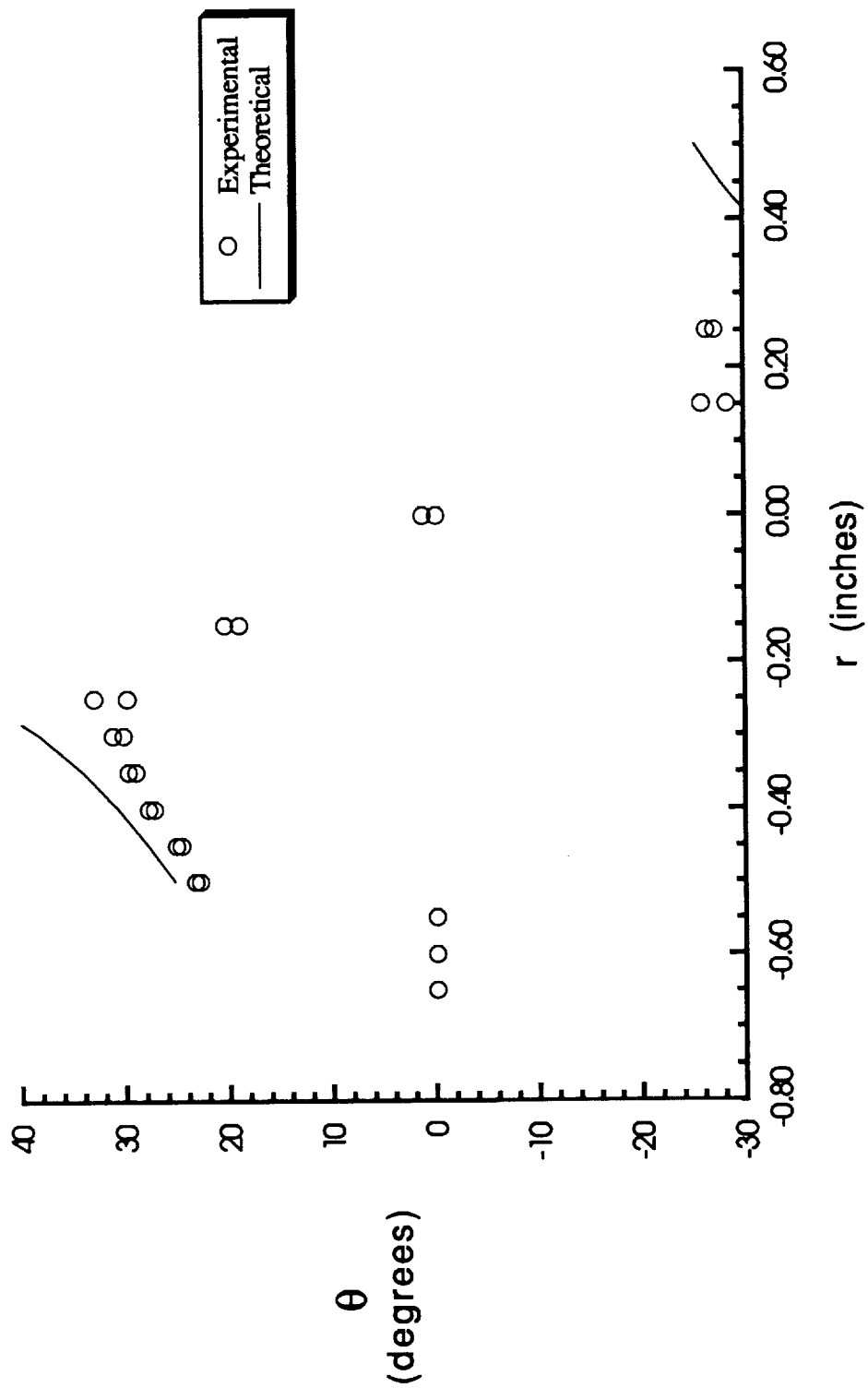


Figure 5.12: Helix Angle as a Function of Radial Distance for High Swirl

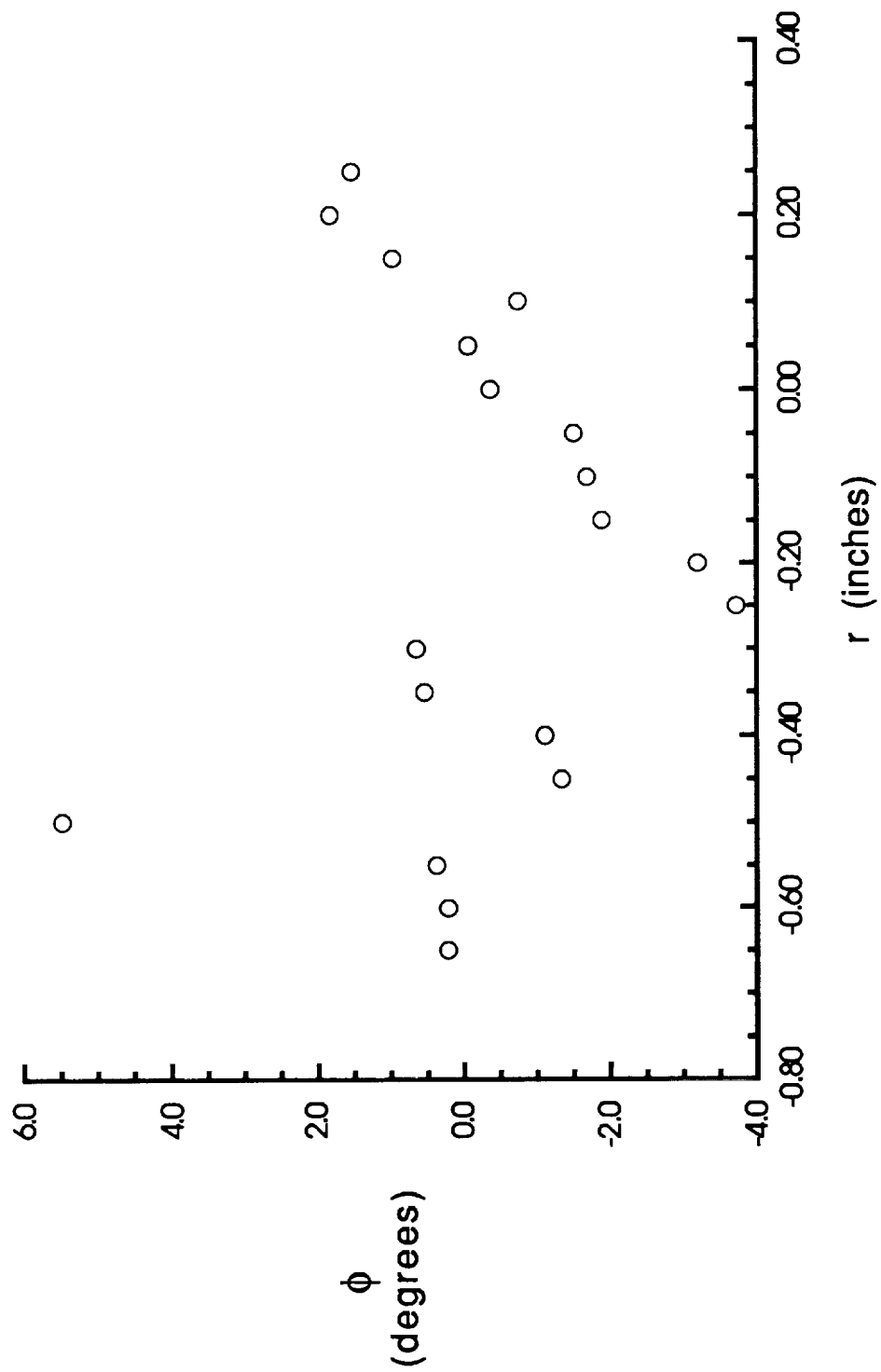


Figure 5.13: Radial Angle as a Function of Radial Distance for No Swirl

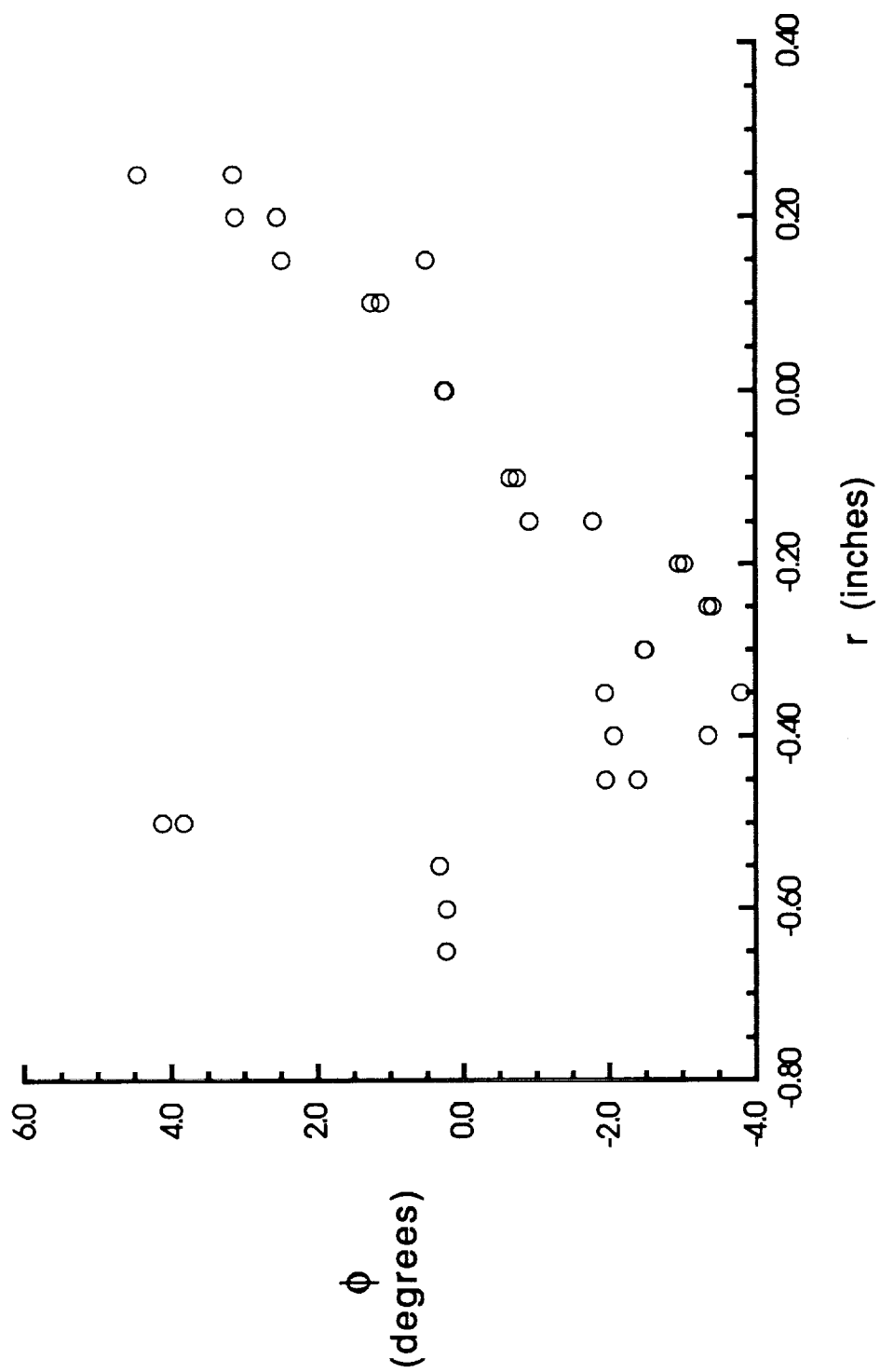


Figure 5.14: Radial Angle as a Function of Radial Distance for Low Swirl

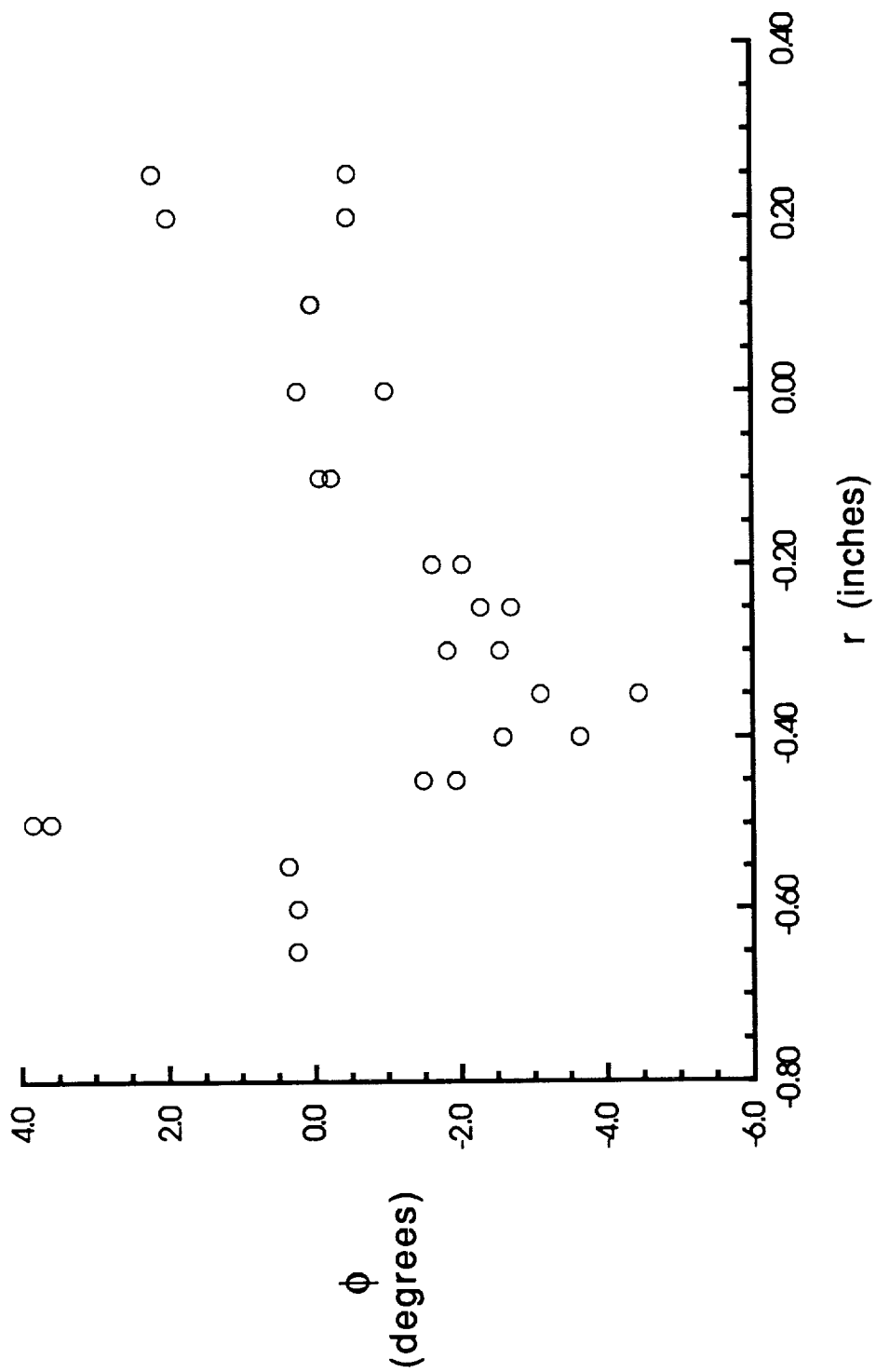


Figure 5.15: Radial Angle as a Function of Radial Distance for Medium Swirl

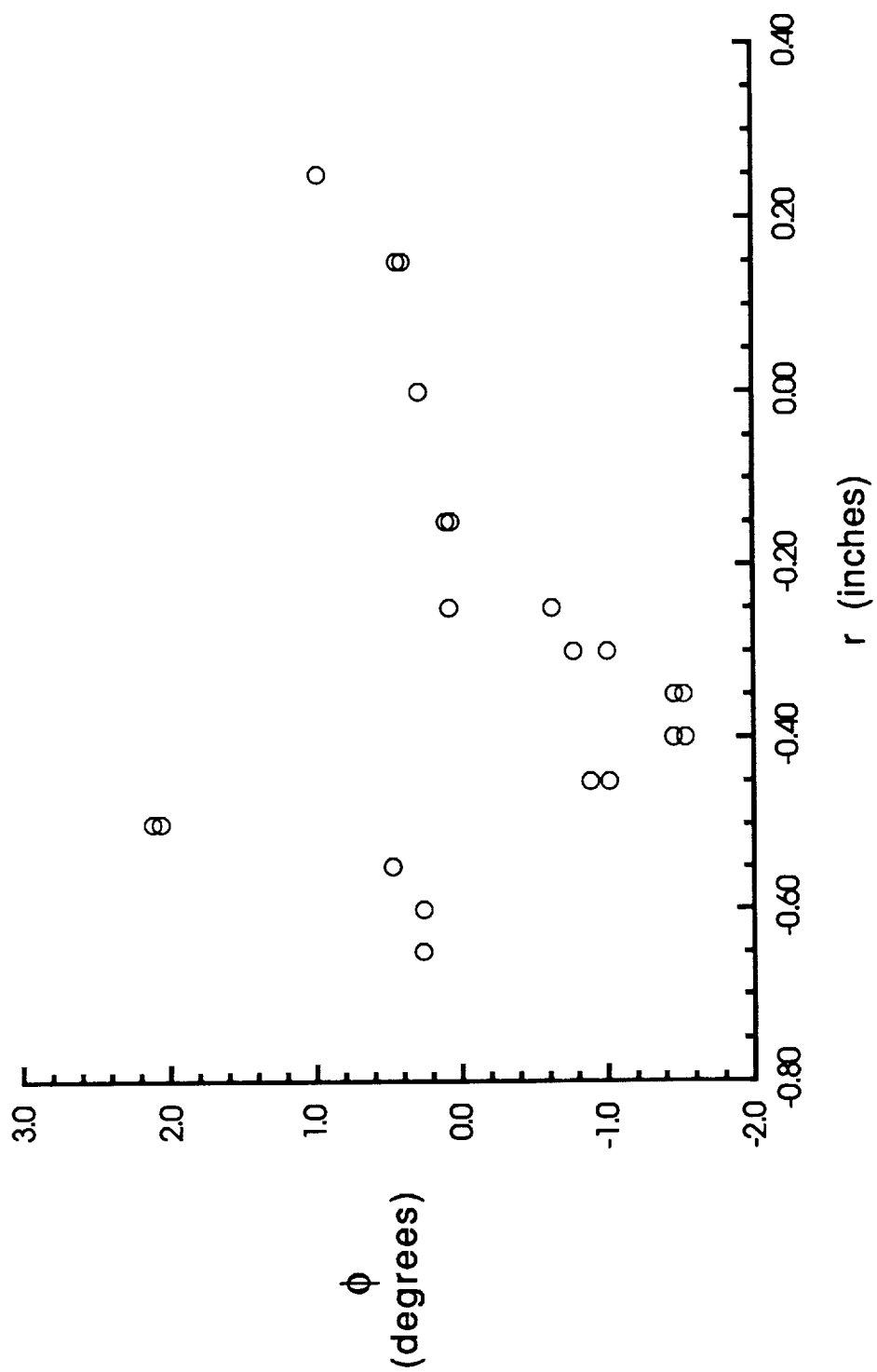


Figure 5.16: Radial Angle as a Function of Radial Distance for High Swirl

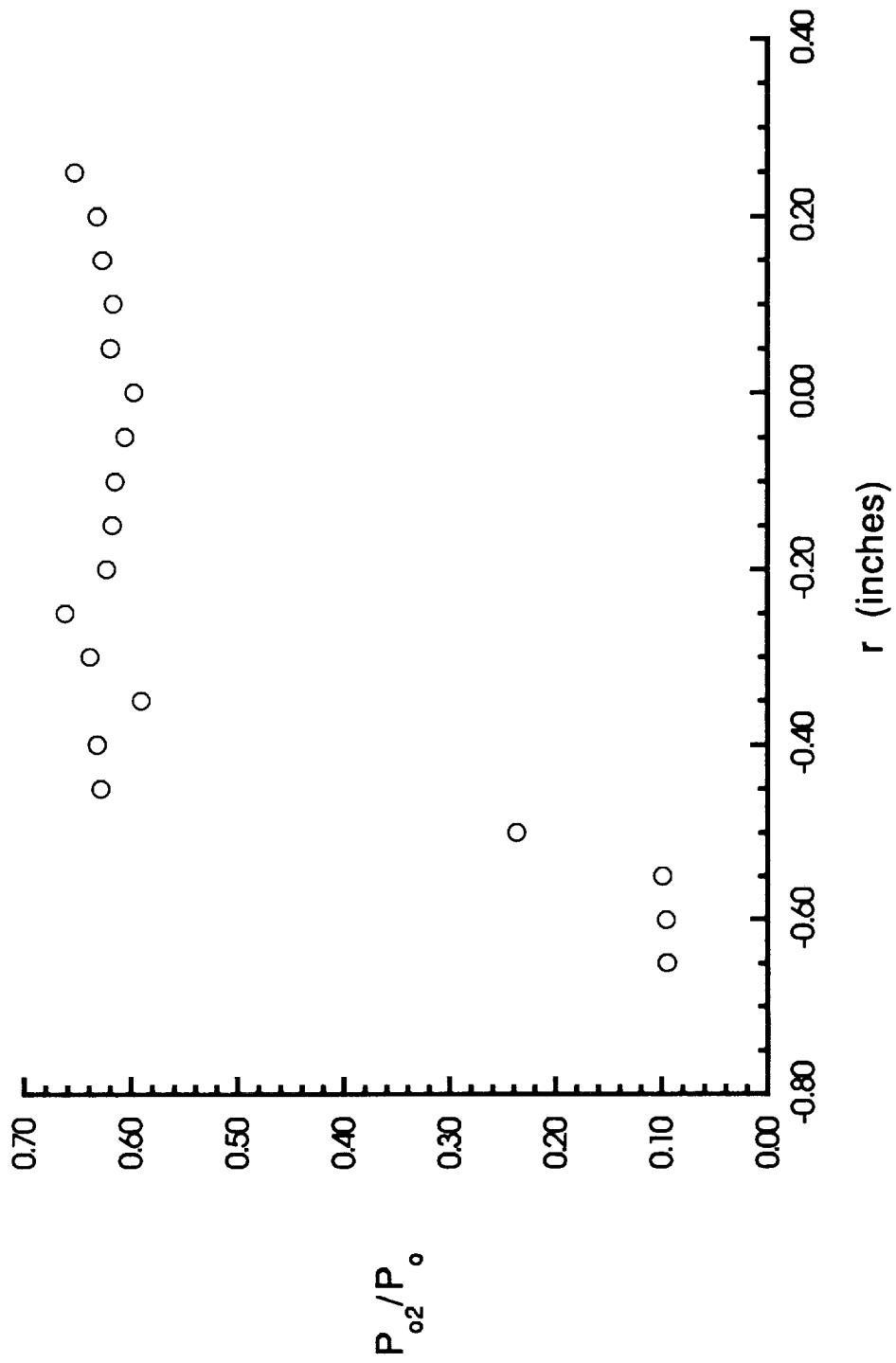


Figure 5.17: Pitot Pressure as a Function of Radial Distance for No Swirl

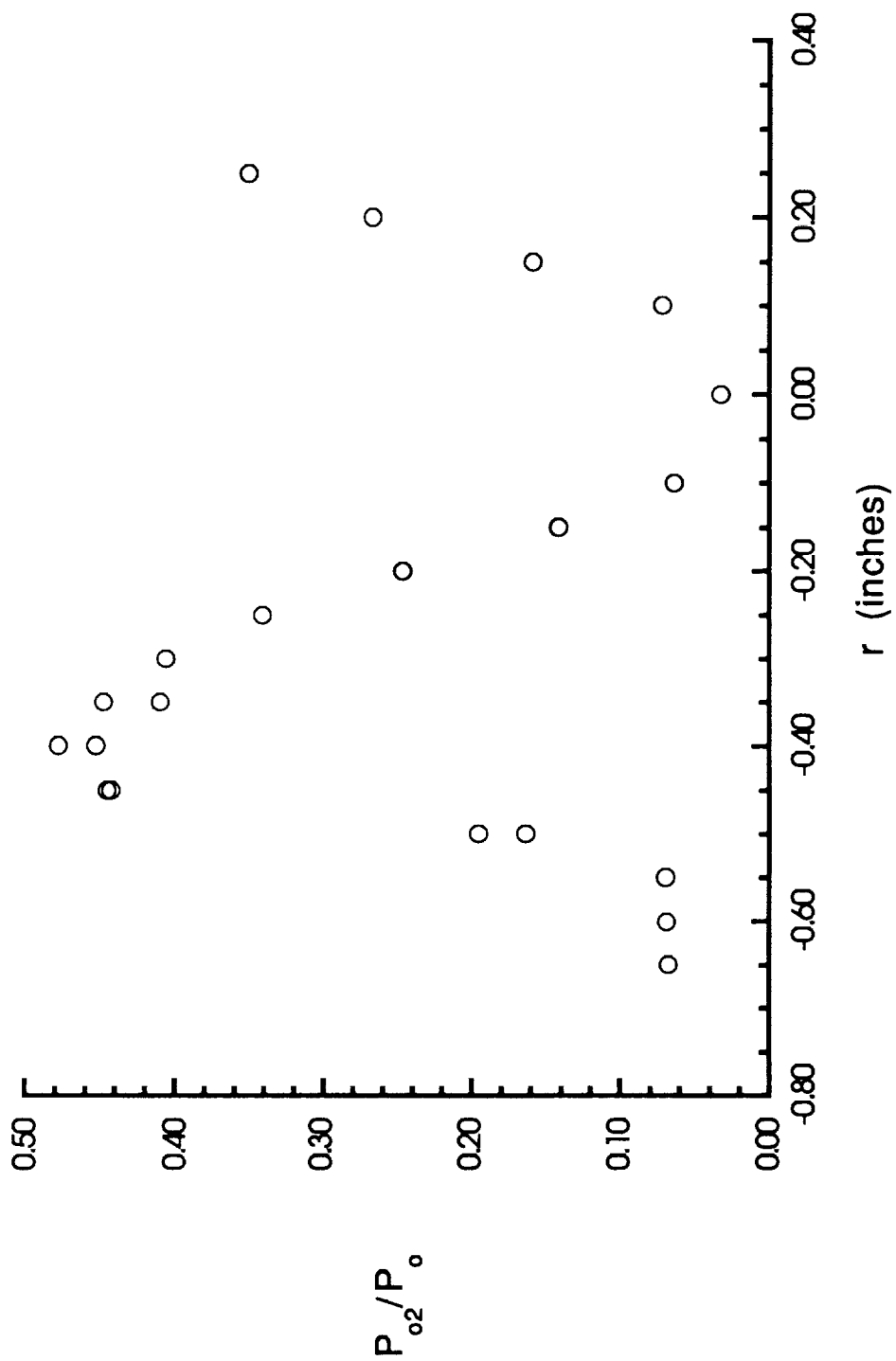


Figure 5.18: Pitot Pressure as a Function of Radial Distance for Low Swirl

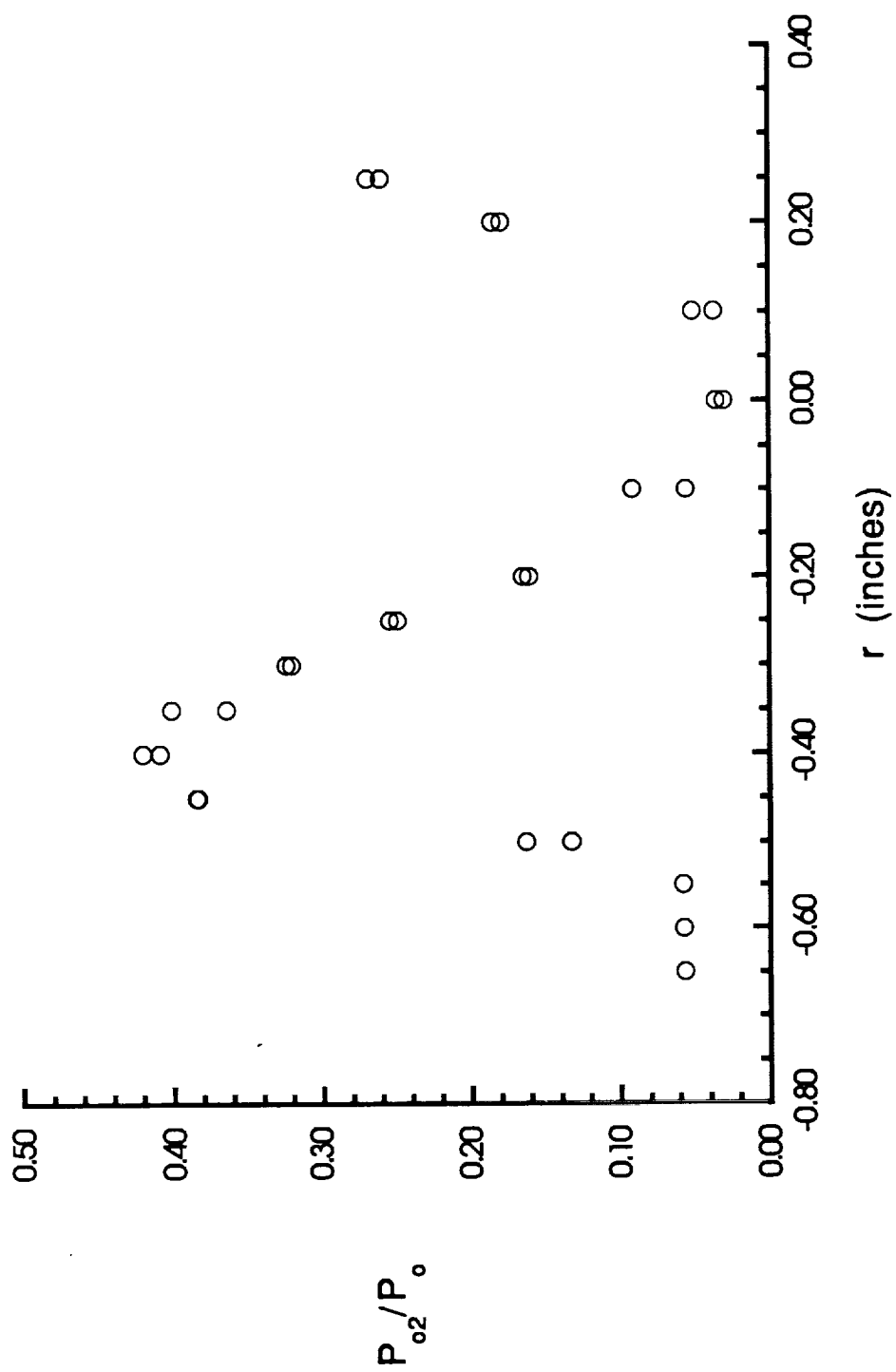


Figure 5.19: Pitot Pressure as a Function of Radial Distance for Medium Swirl

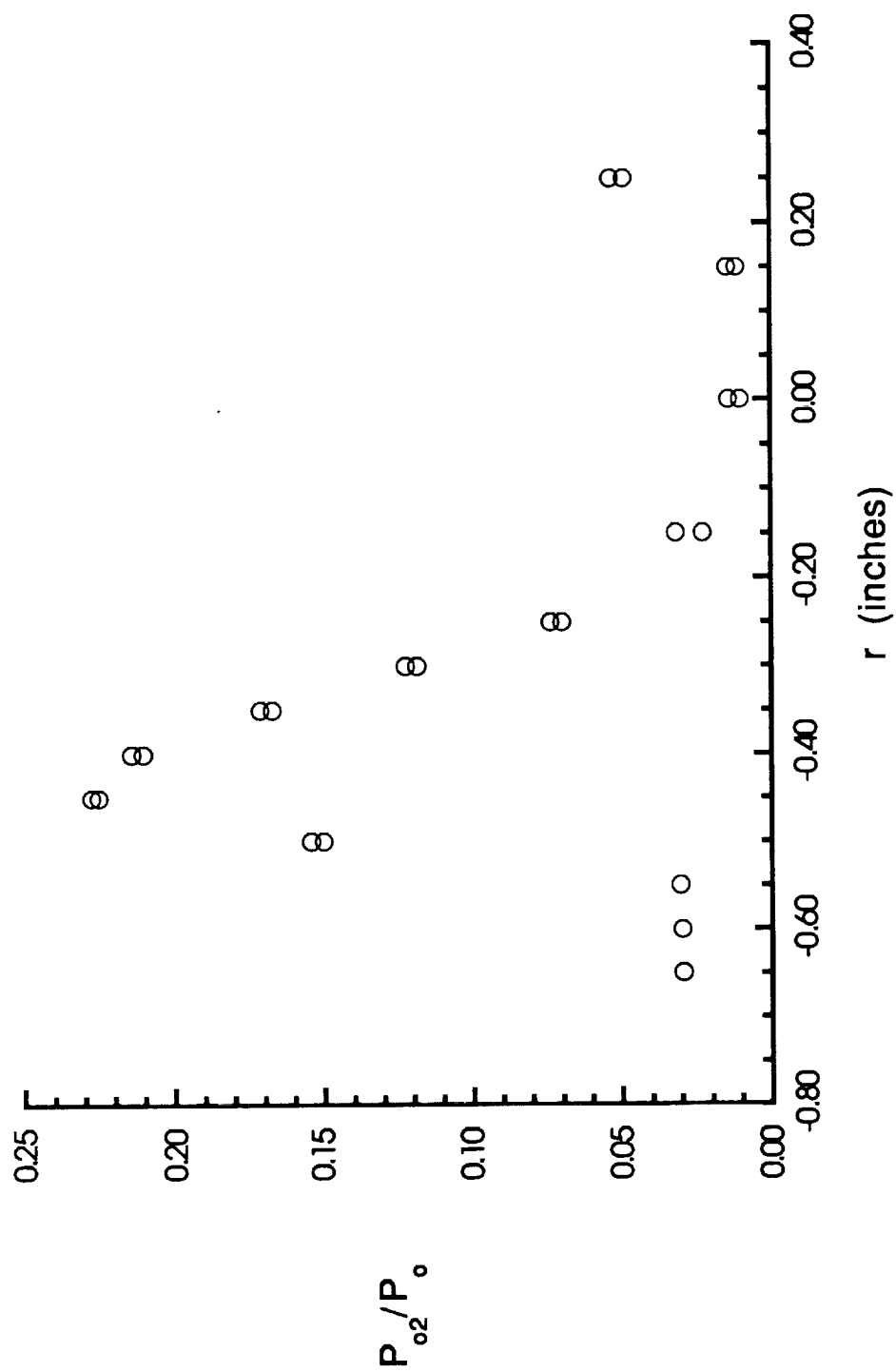


Figure 5.20: Pitot Pressure as a Function of Radial Distance for High Swirl

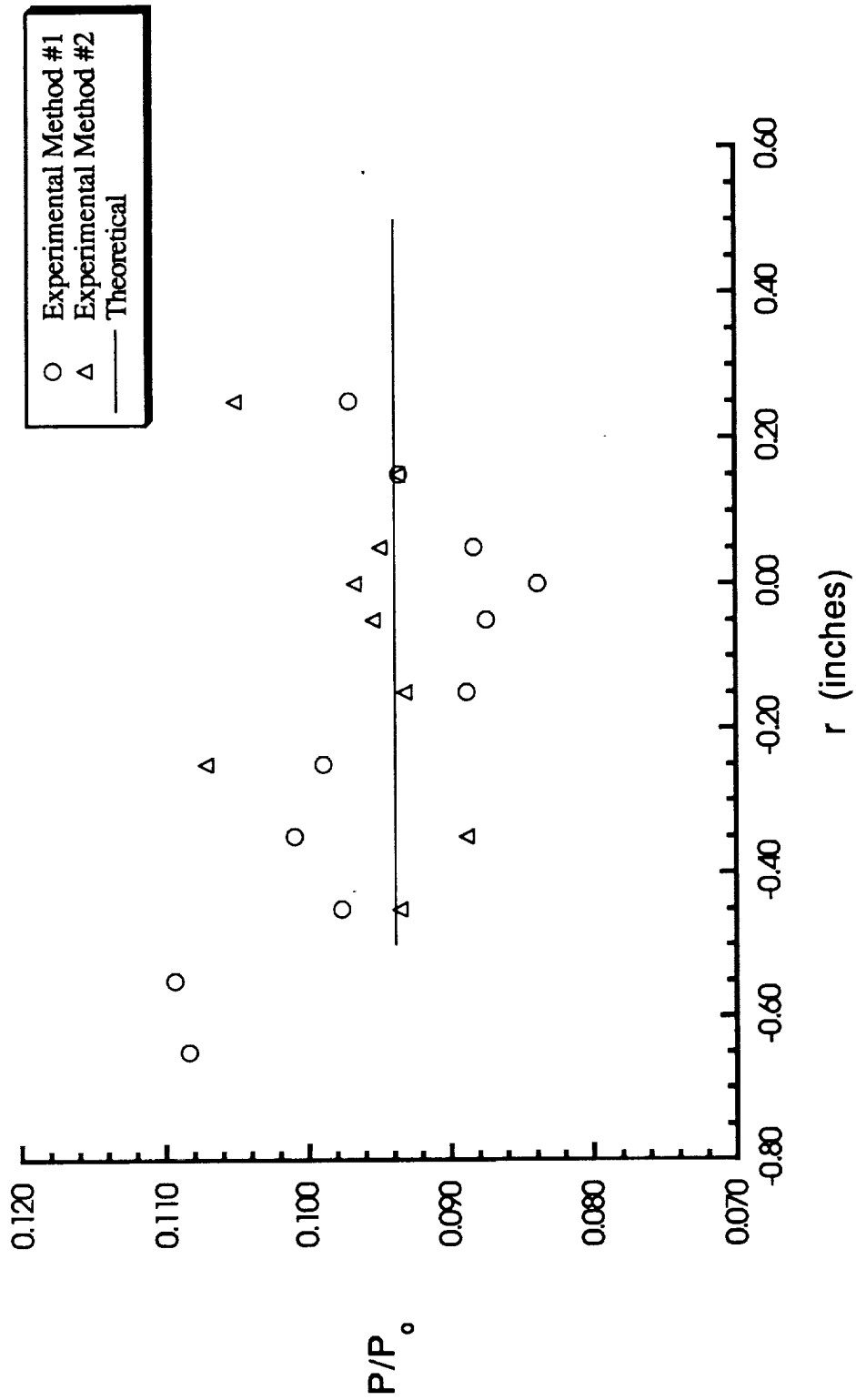


Figure 5.21: Static Pressure as a Function of Radial Distance for No Swirl

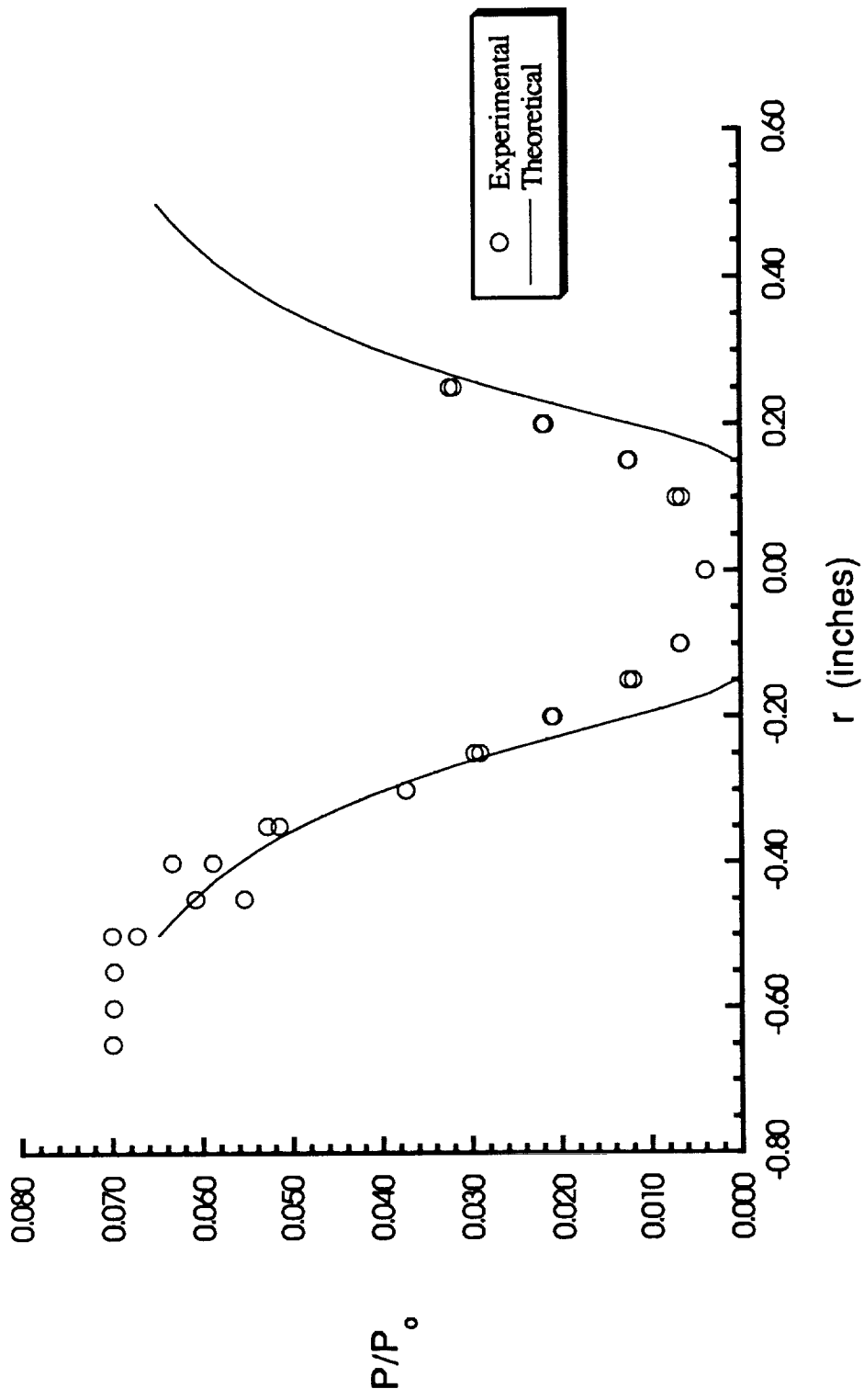


Figure 5.22: Static Pressure as a Function of Radial Distance for Low Swirl

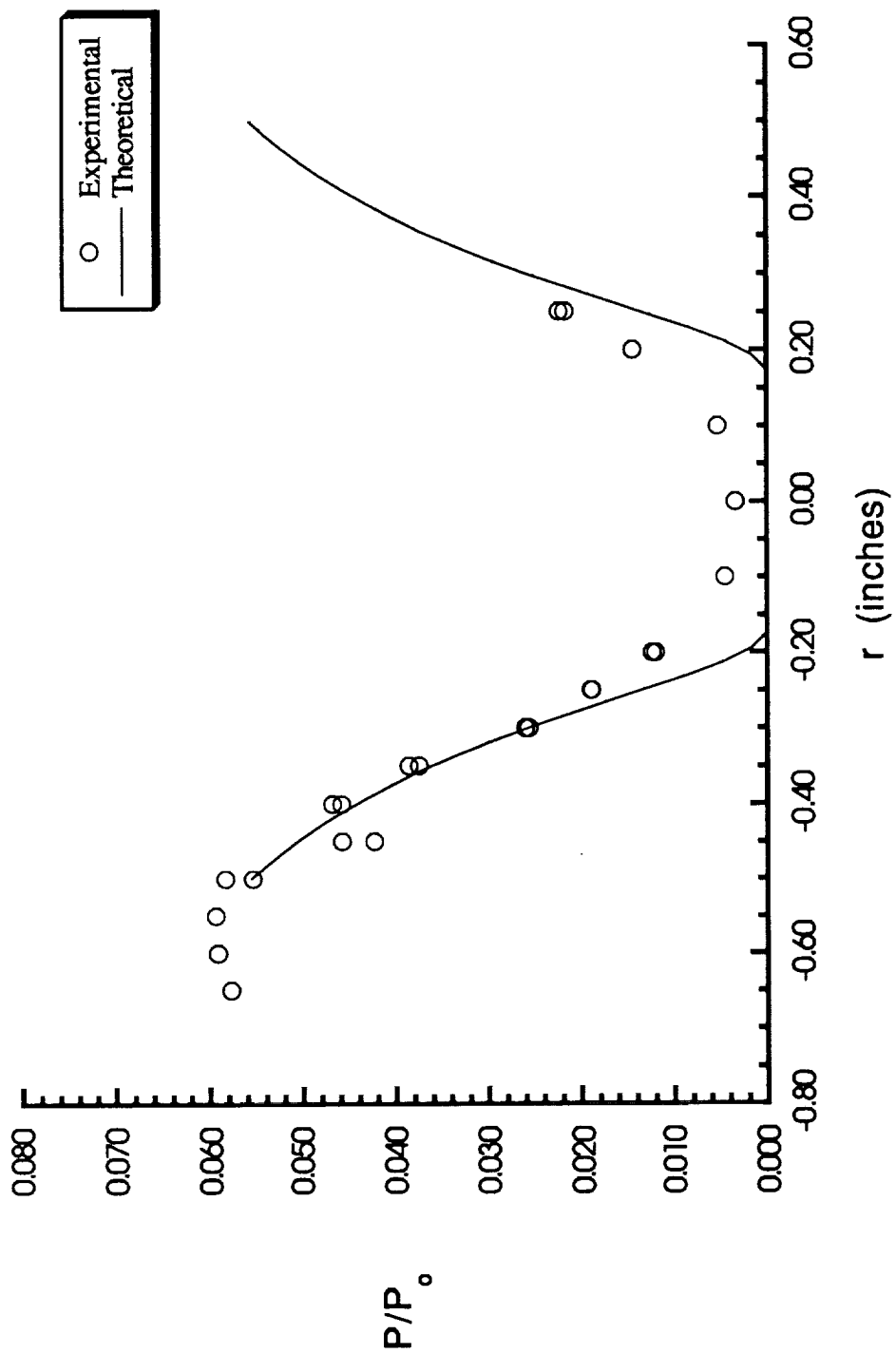


Figure 5.23: Static Pressure as a Function of Radial Distance for Medium Swirl

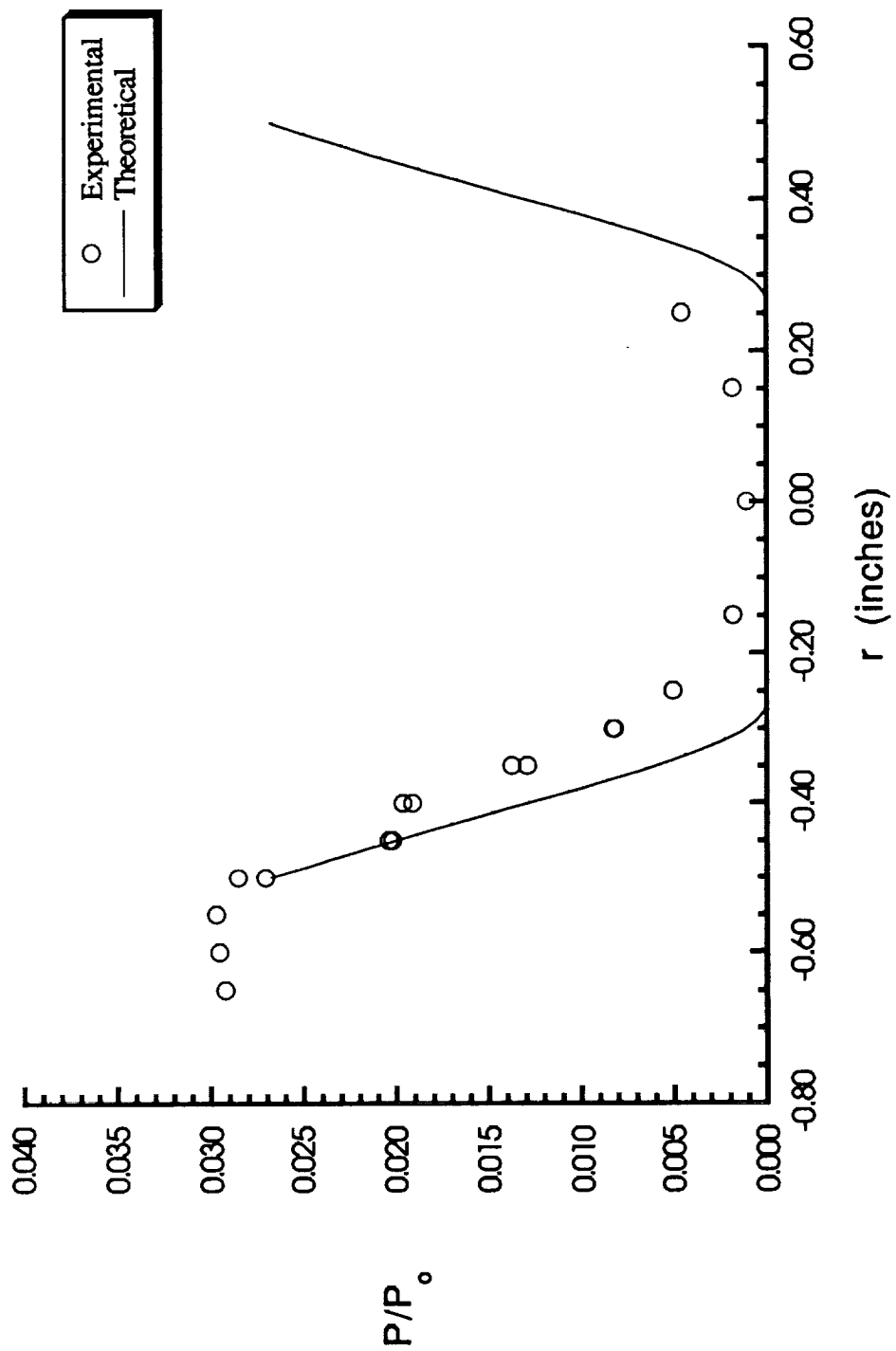


Figure 5.24: Static Pressure as a Function of Radial Distance for High Swirl

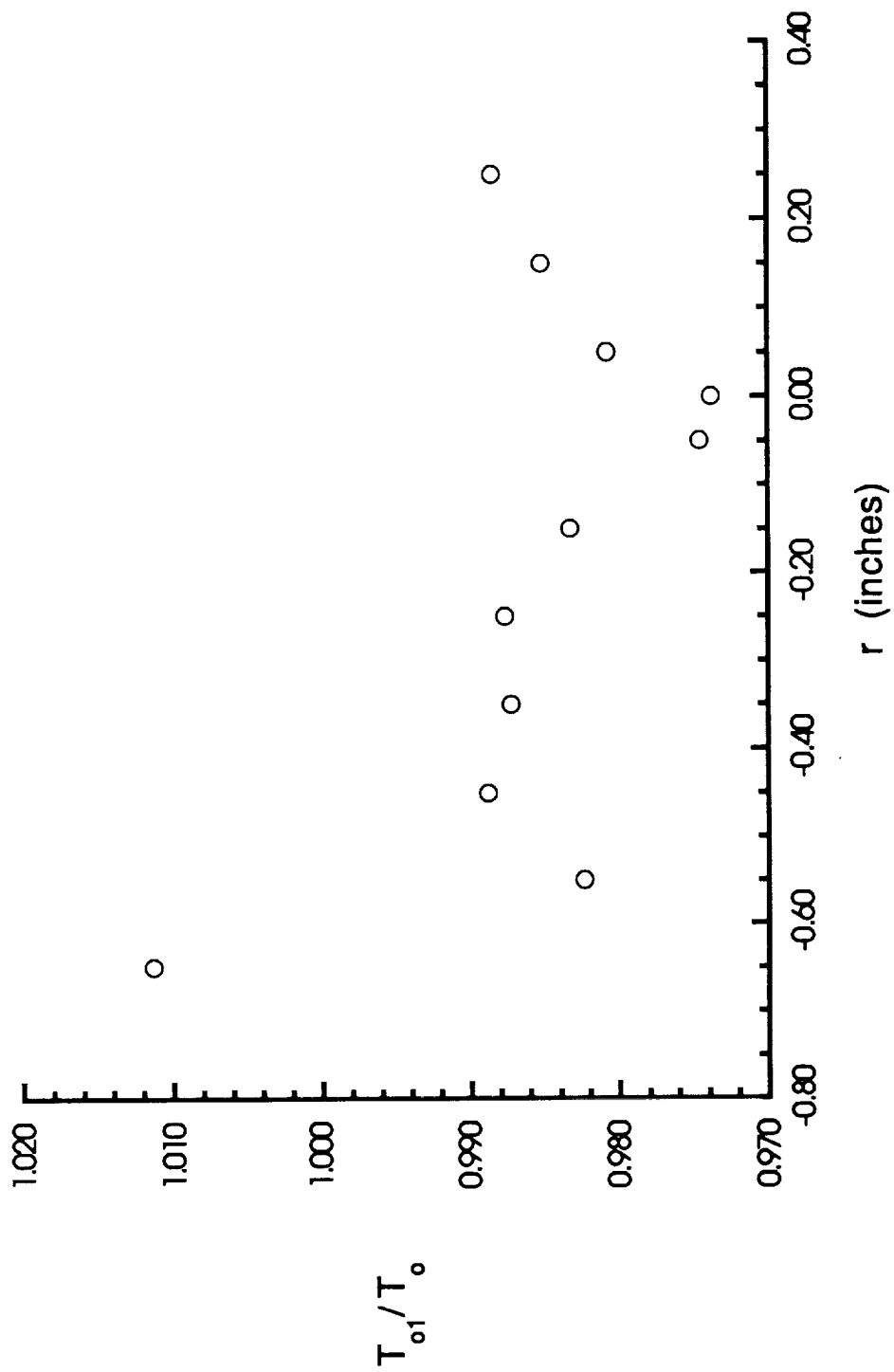


Figure 5.25: Total Temperature as a Function of Radial Distance for No Swirl

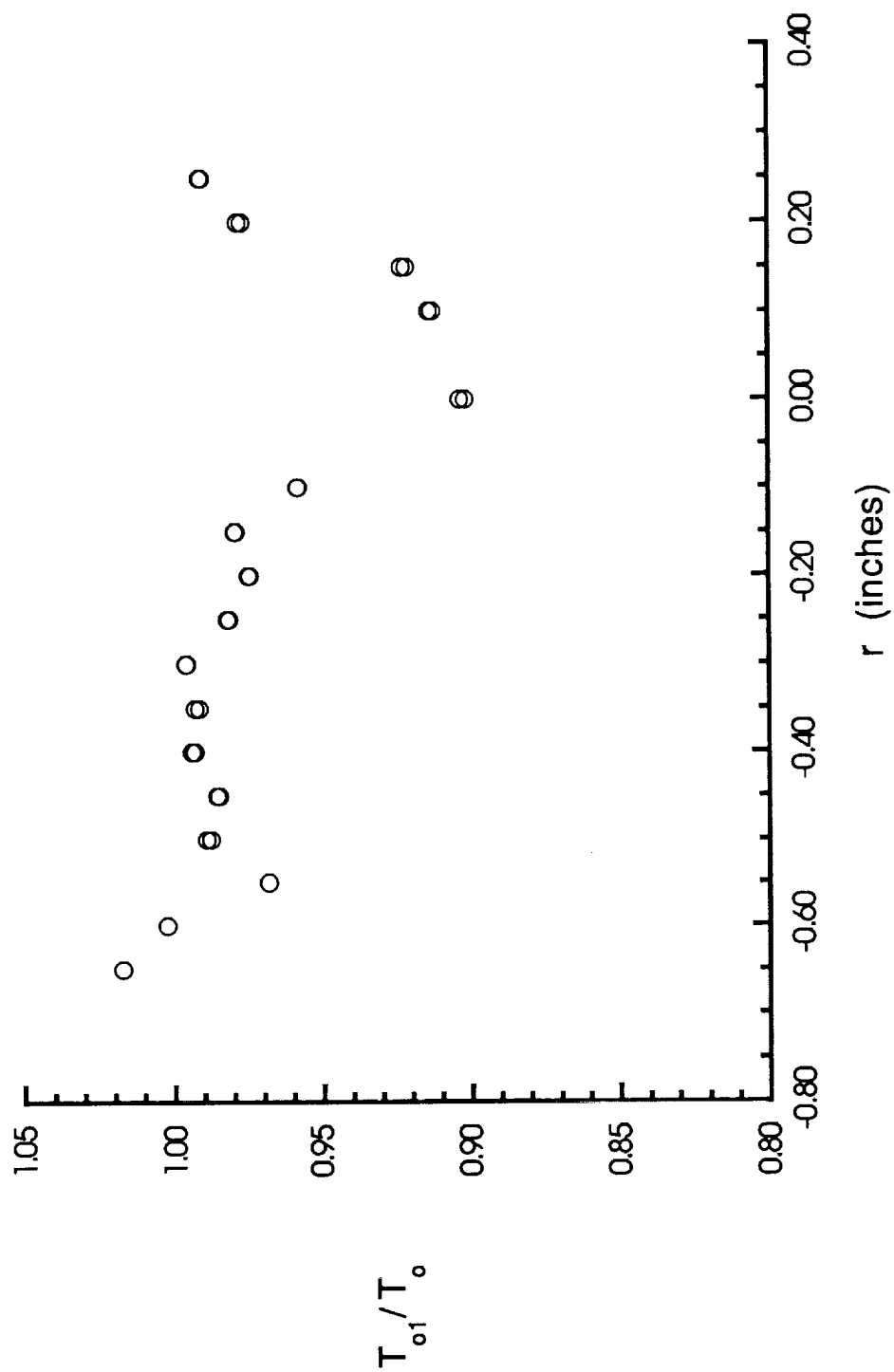


Figure 5.26: Total Temperature as a Function of Radial Distance for Low Swirl

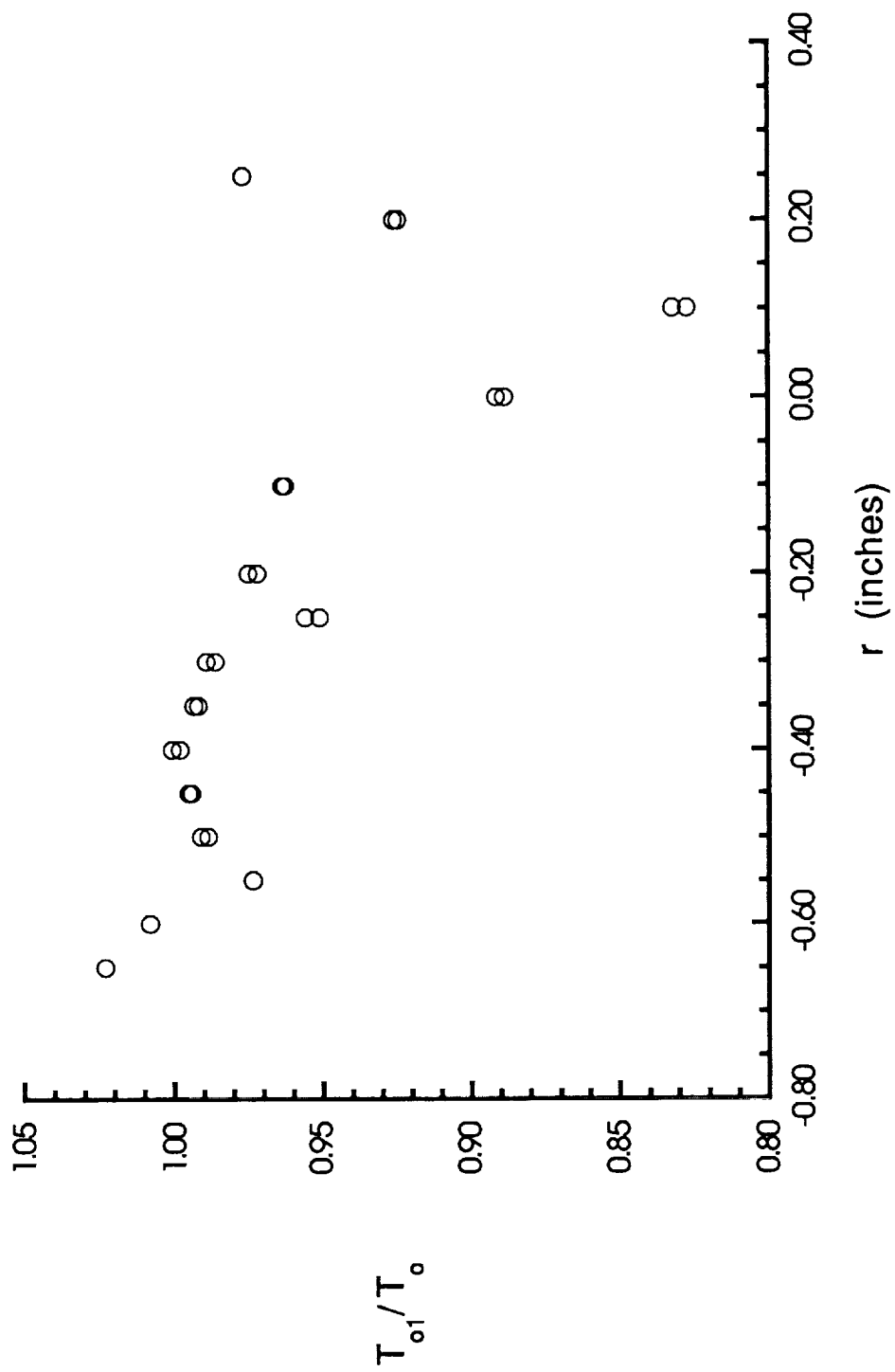


Figure 5.27: Total Temperature as a Function of Radial Distance for Medium Swirl

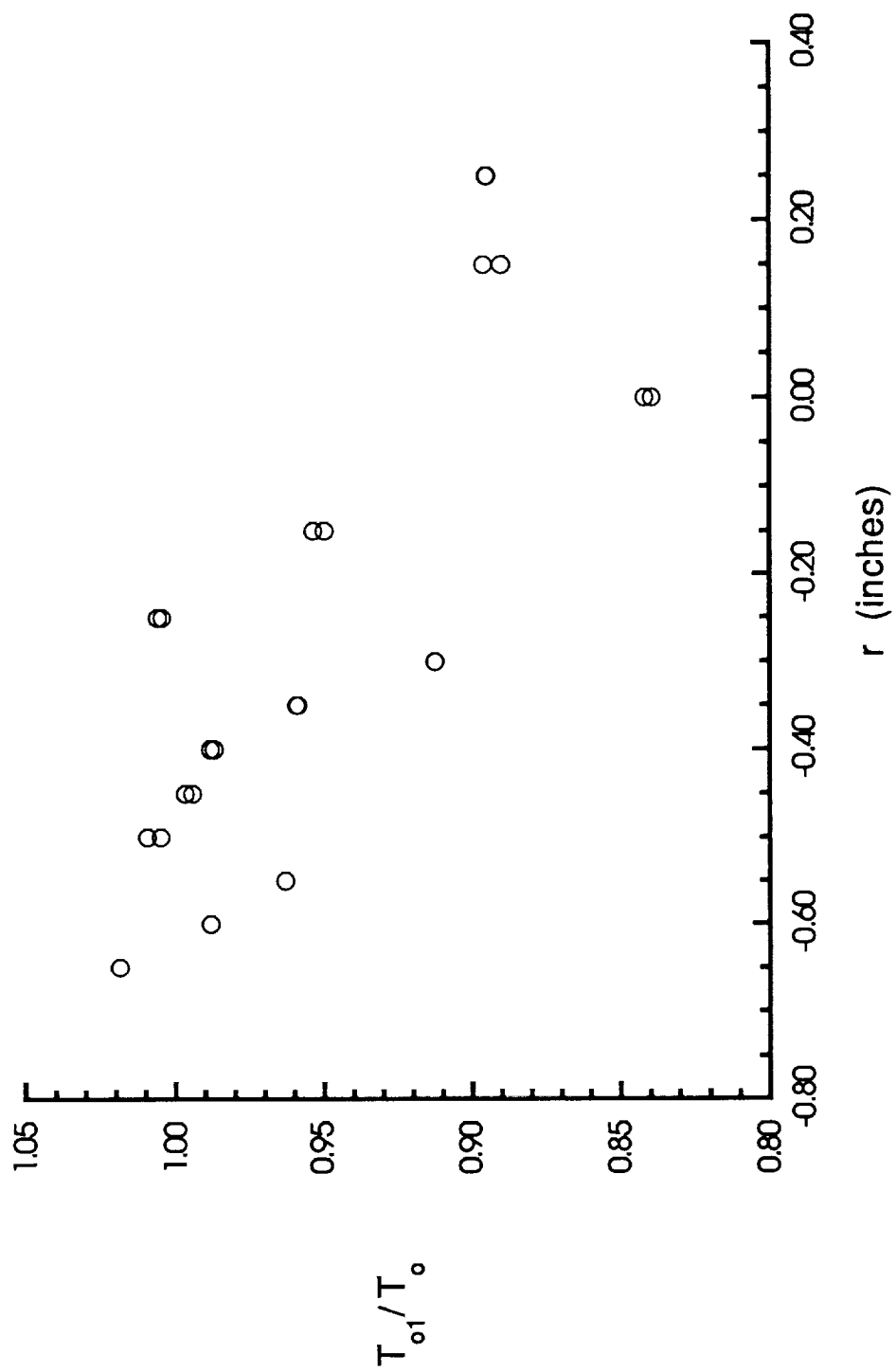


Figure 5.28: Total Temperature as a Function of Radial Distance for High Swirl

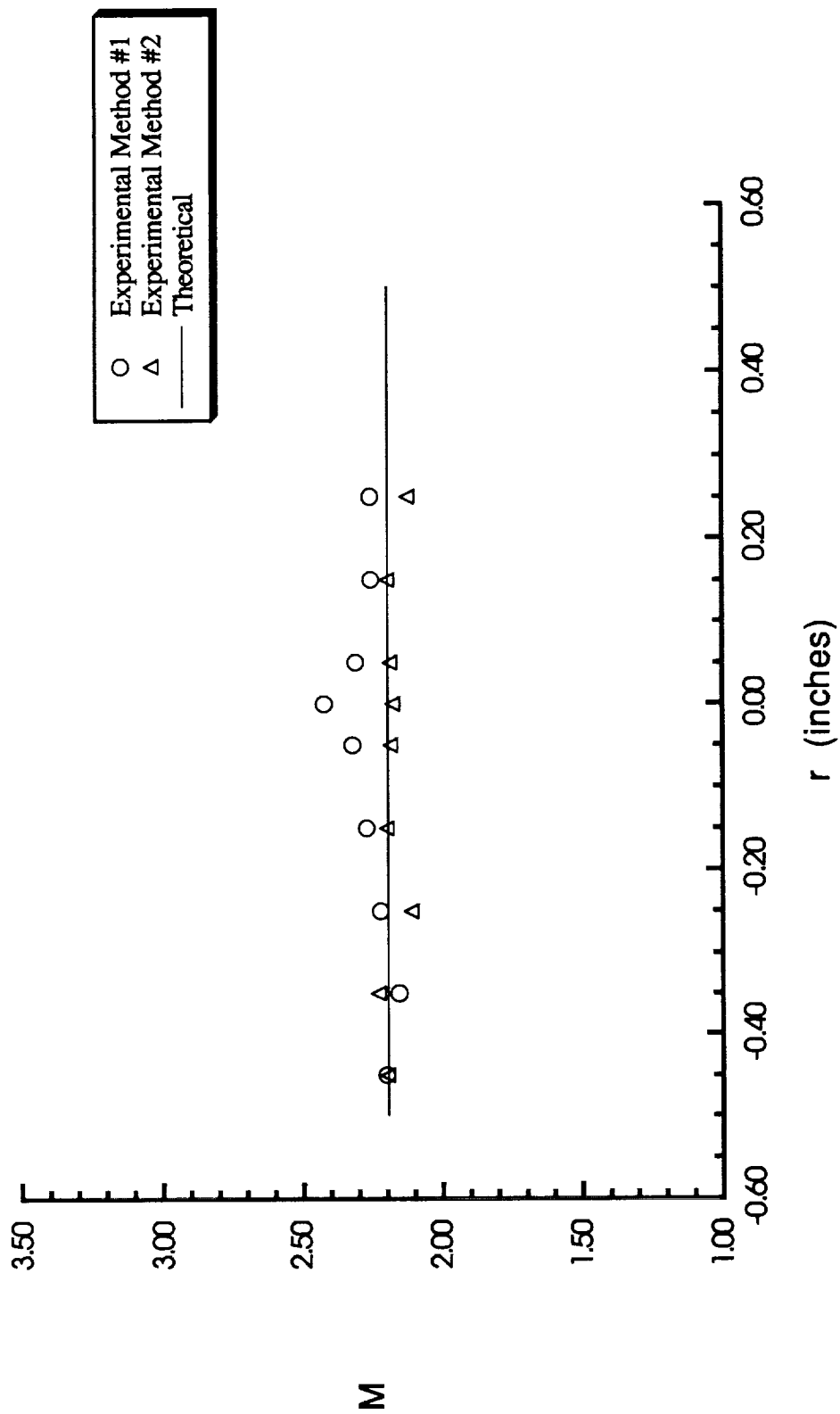


Figure 5.29: Mach Number as a Function of Radial Distance for No Swirl

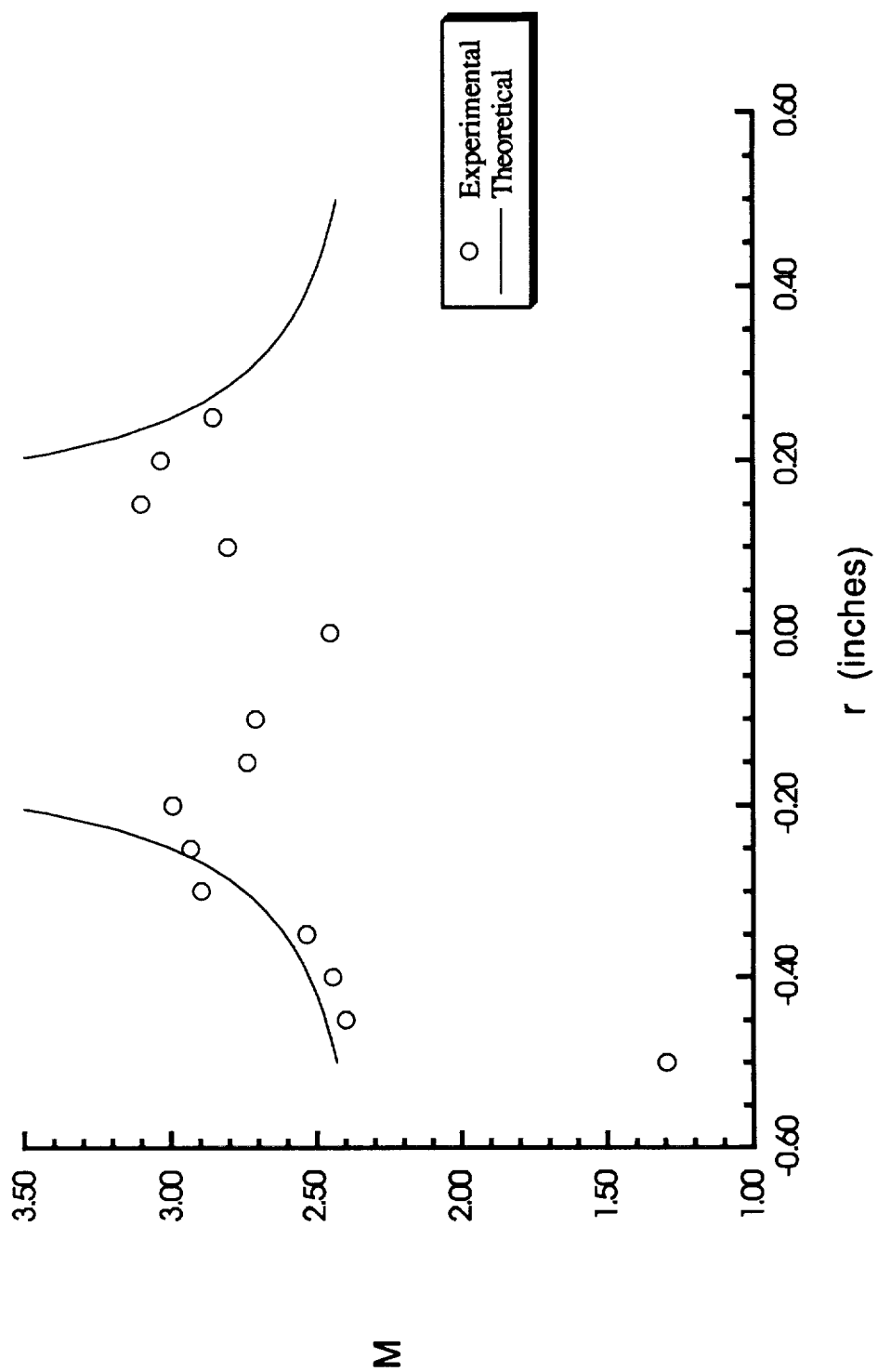


Figure 5.30: Mach Number as a Function of Radial Distance for Low Swirl

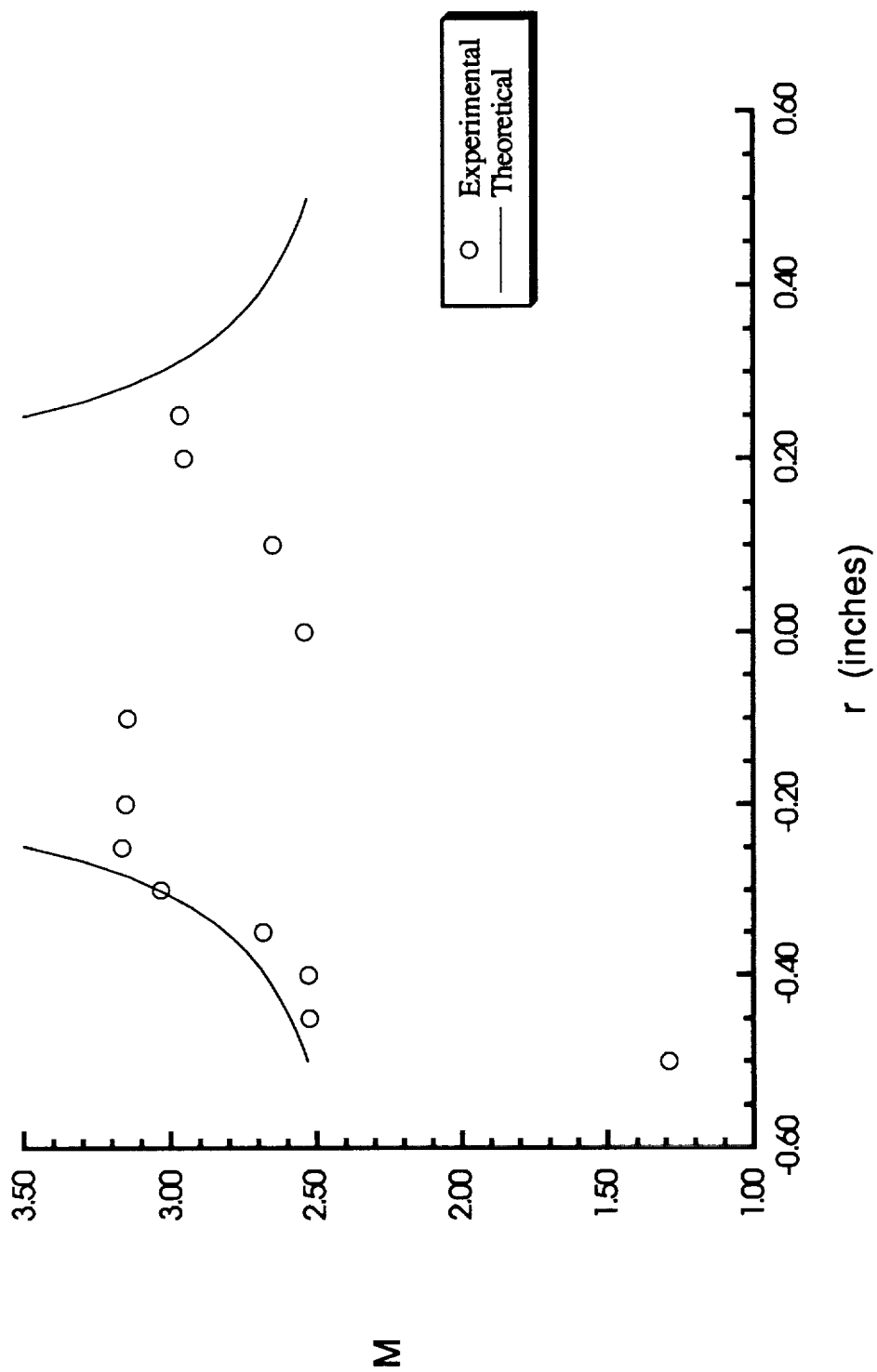


Figure 5.31: Mach Number as a Function of Radial Distance for Medium Swirl

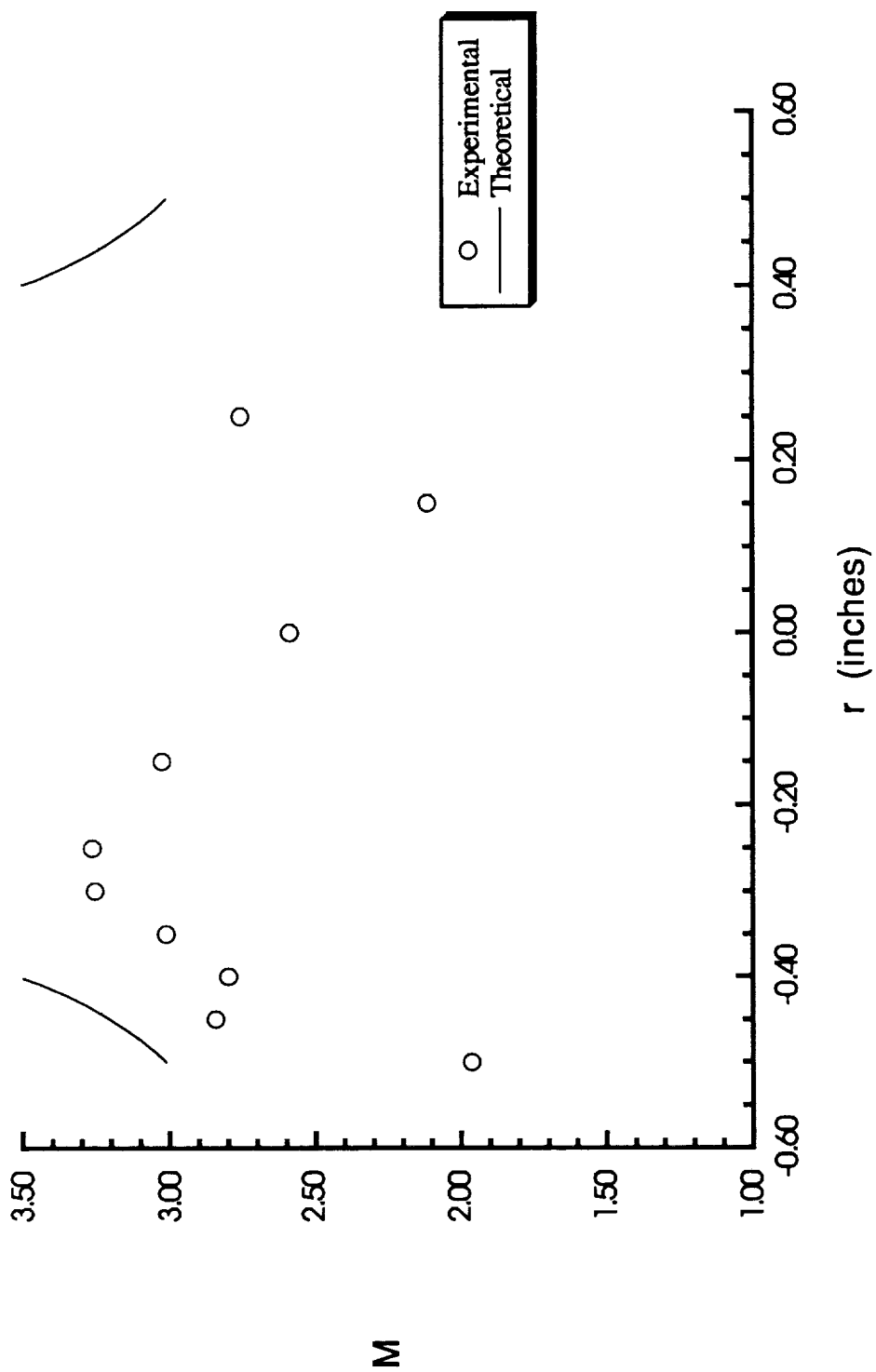


Figure 5.32: Mach Number as a Function of Radial Distance for High Swirl

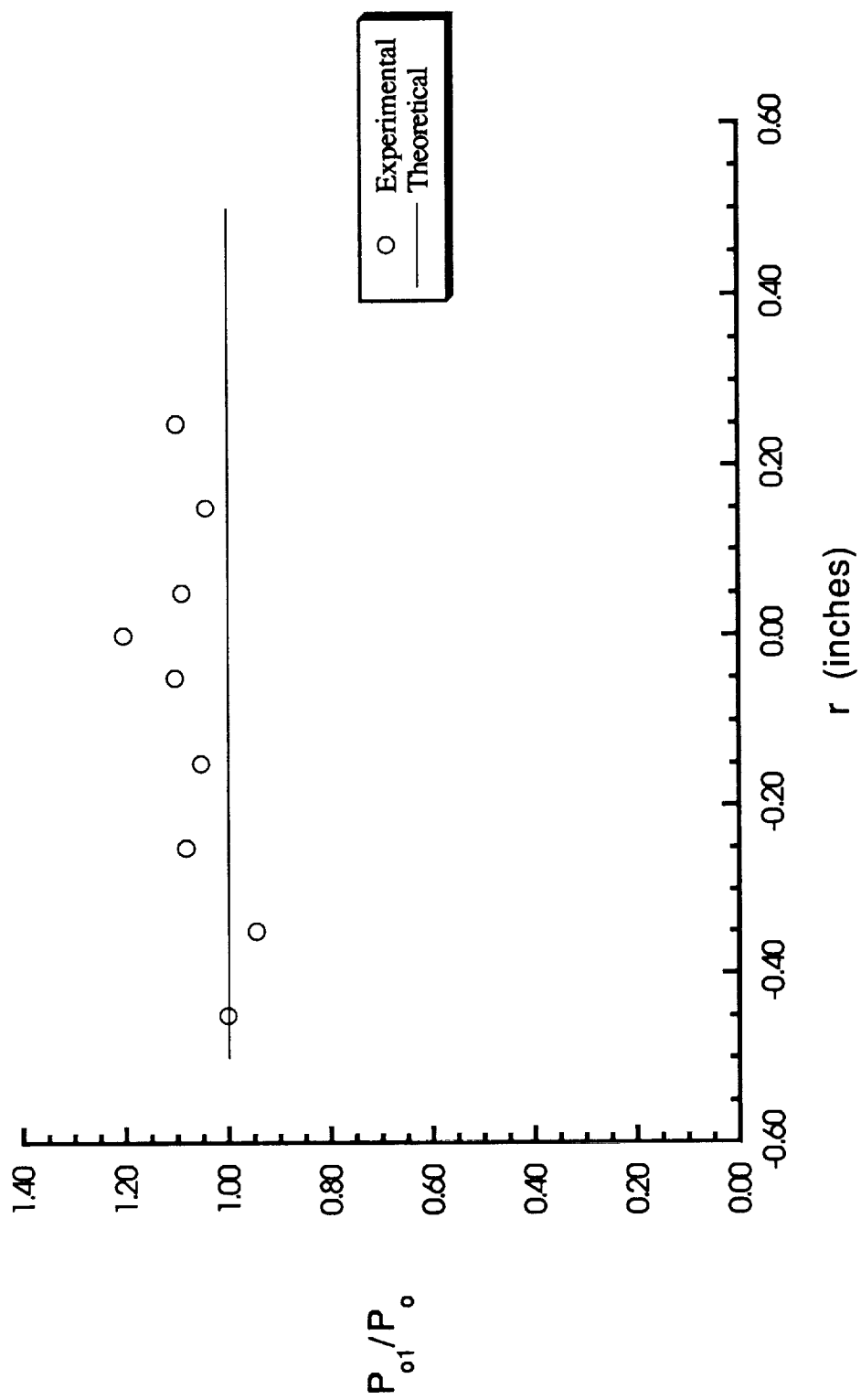


Figure 5.33: Total Pressure as a Function of Radial Distance for No Swirl

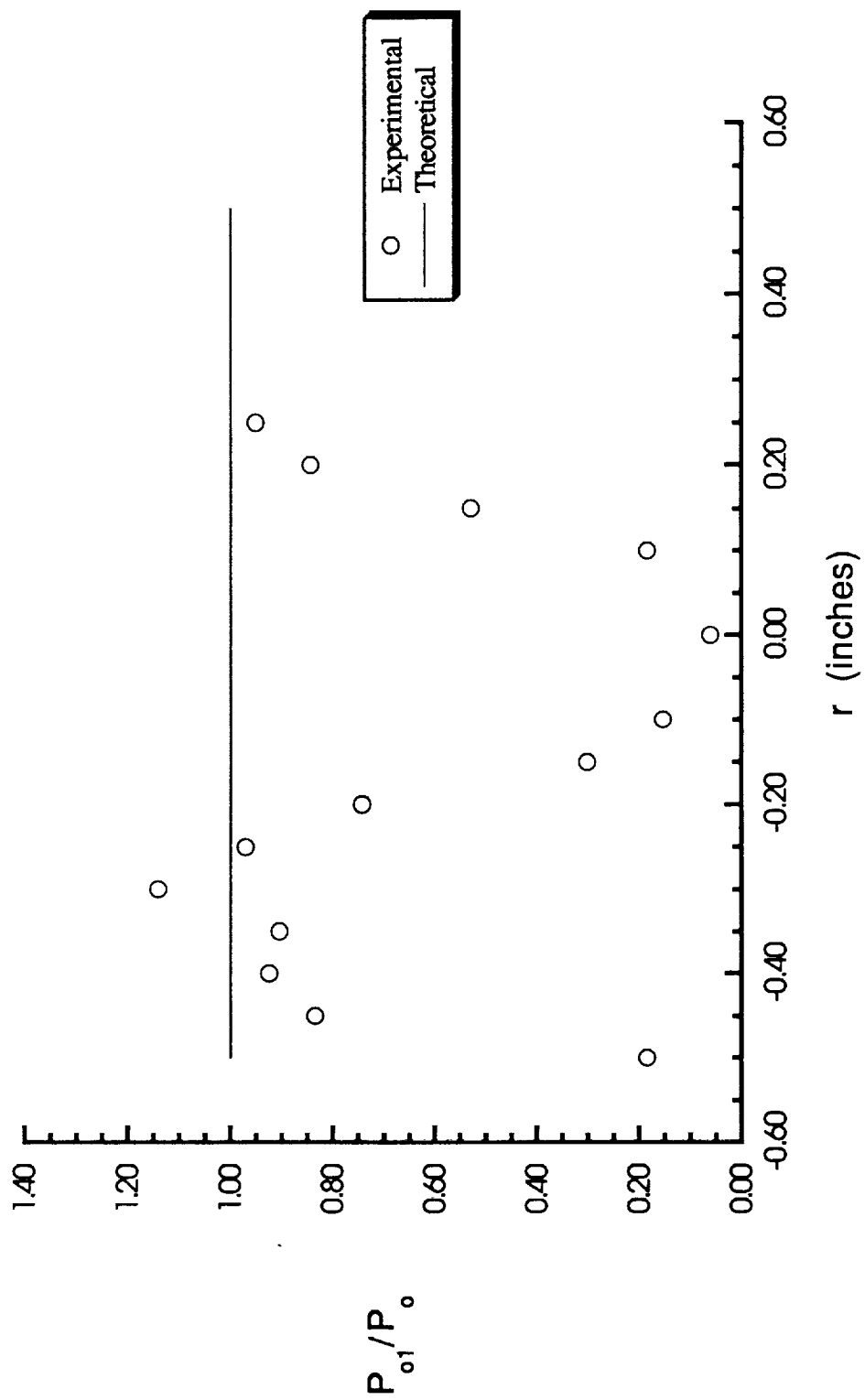


Figure 5.34: Total Pressure as a Function of Radial Distance for Low Swirl

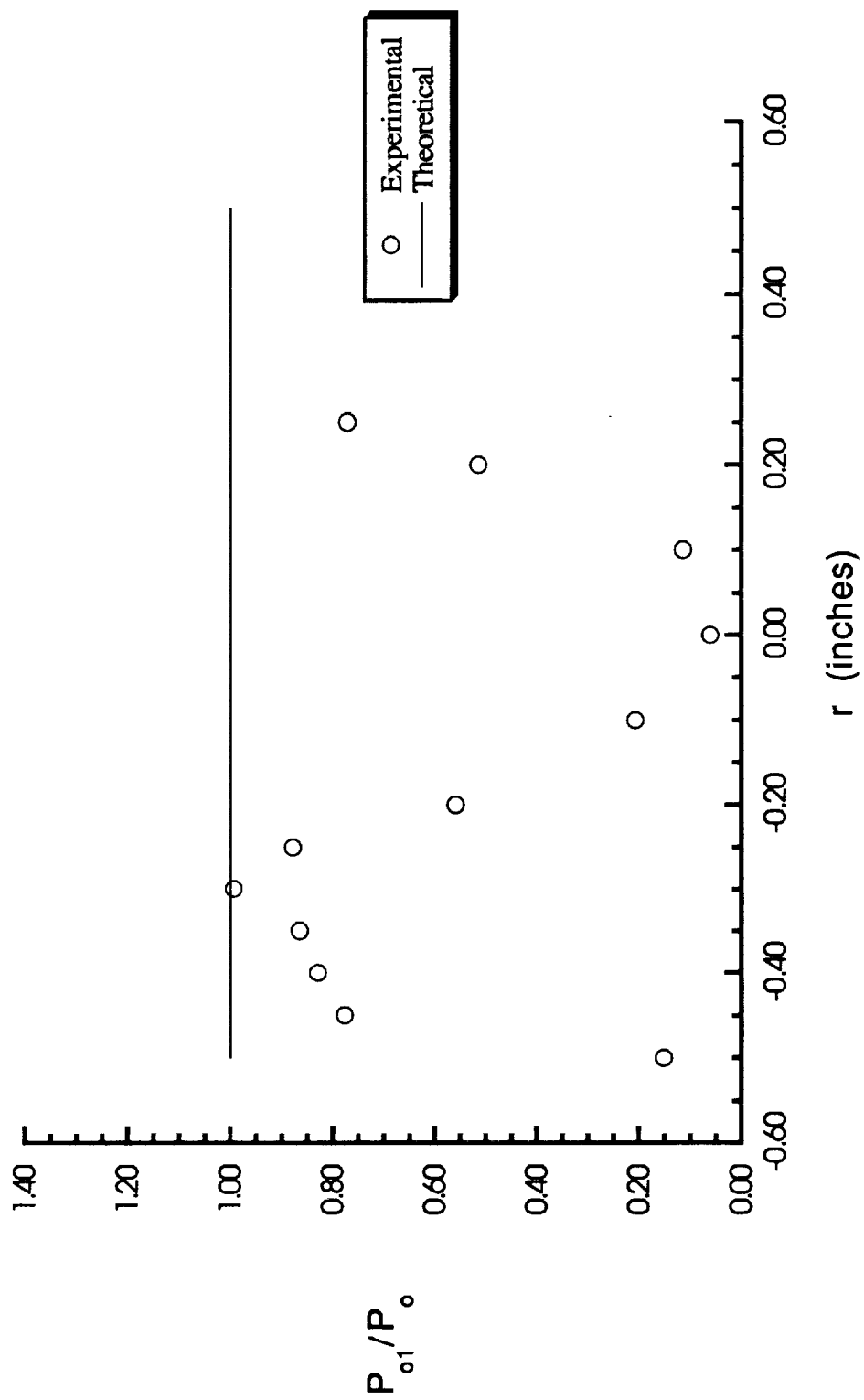


Figure 5.35: Total Pressure as a Function of Radial Distance for Medium Swirl

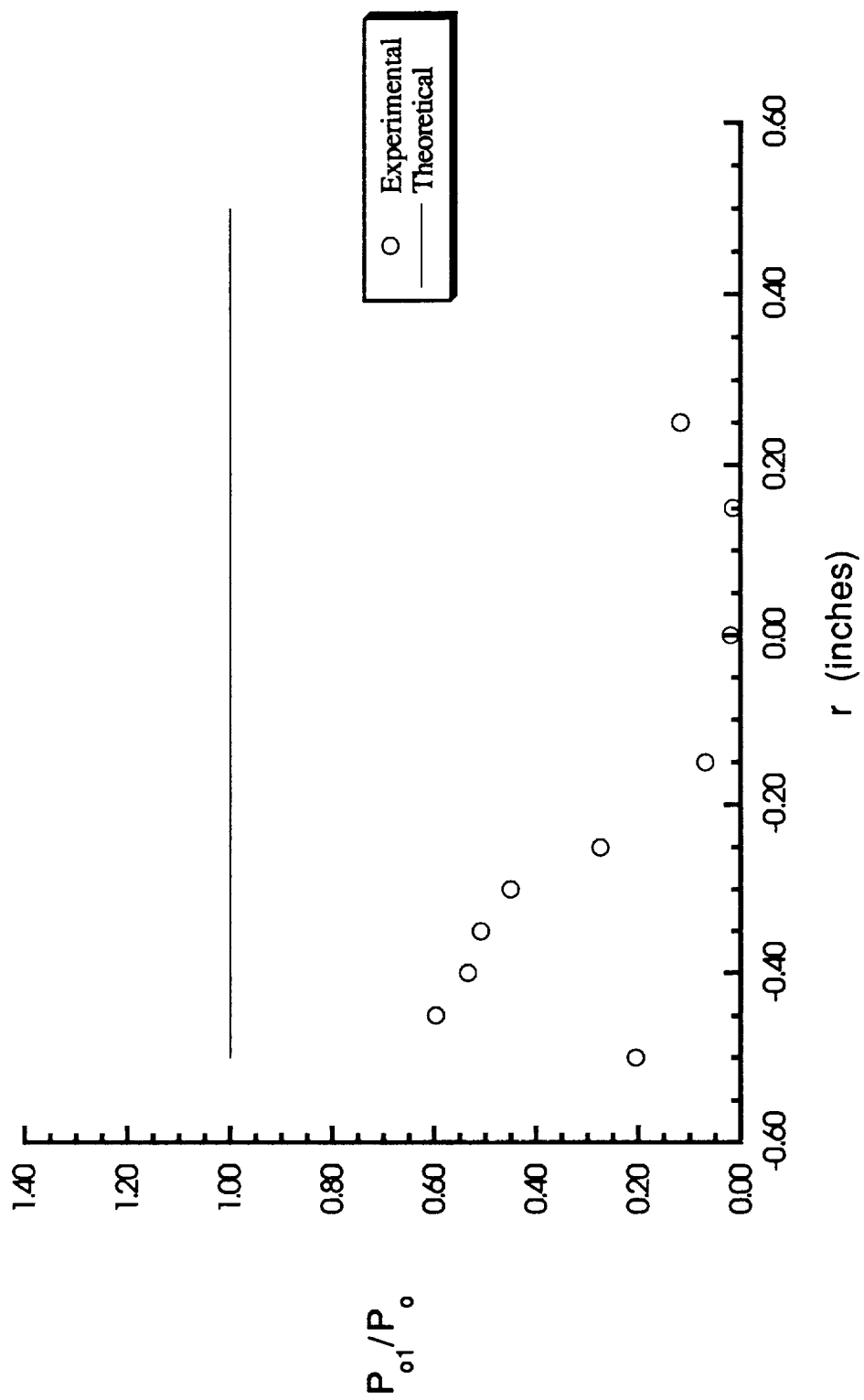


Figure 5.36: Total Pressure as a Function of Radial Distance for High Swirl

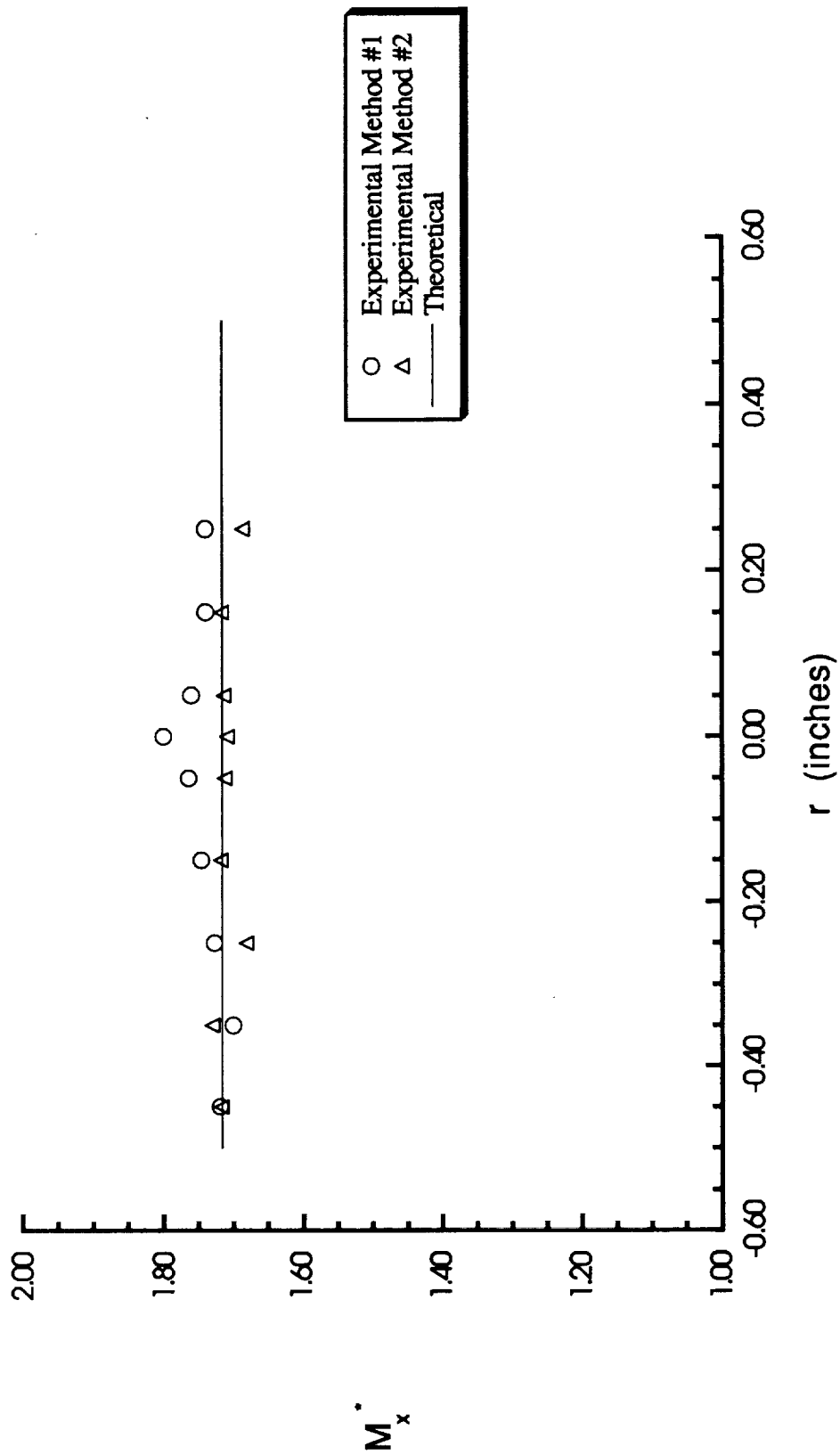


Figure 5.37: Axial Velocity as a Function of Radial Distance for No Swirl

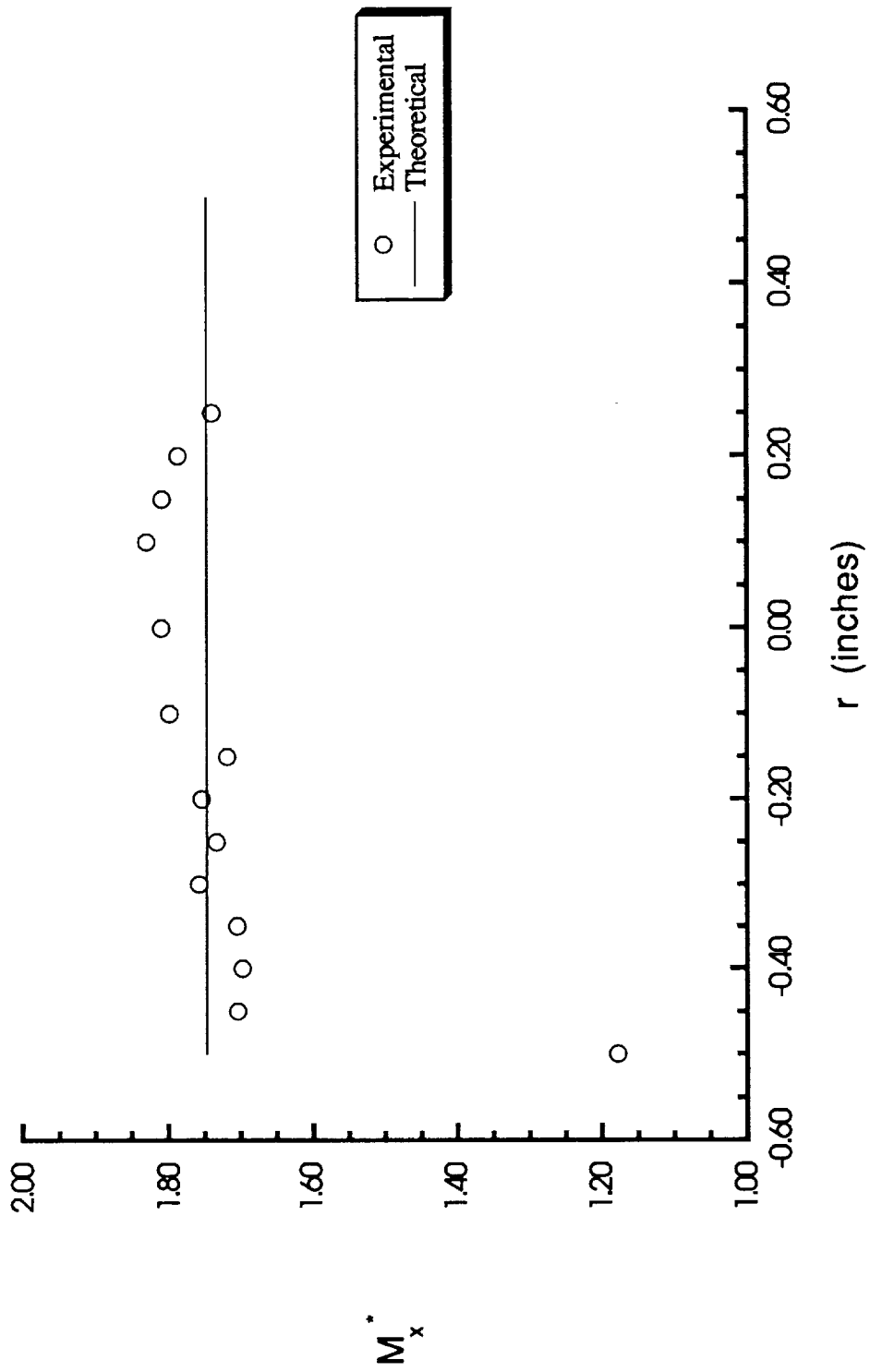


Figure 5.38: Axial Velocity as a Function of Radial Distance for Low Swirl

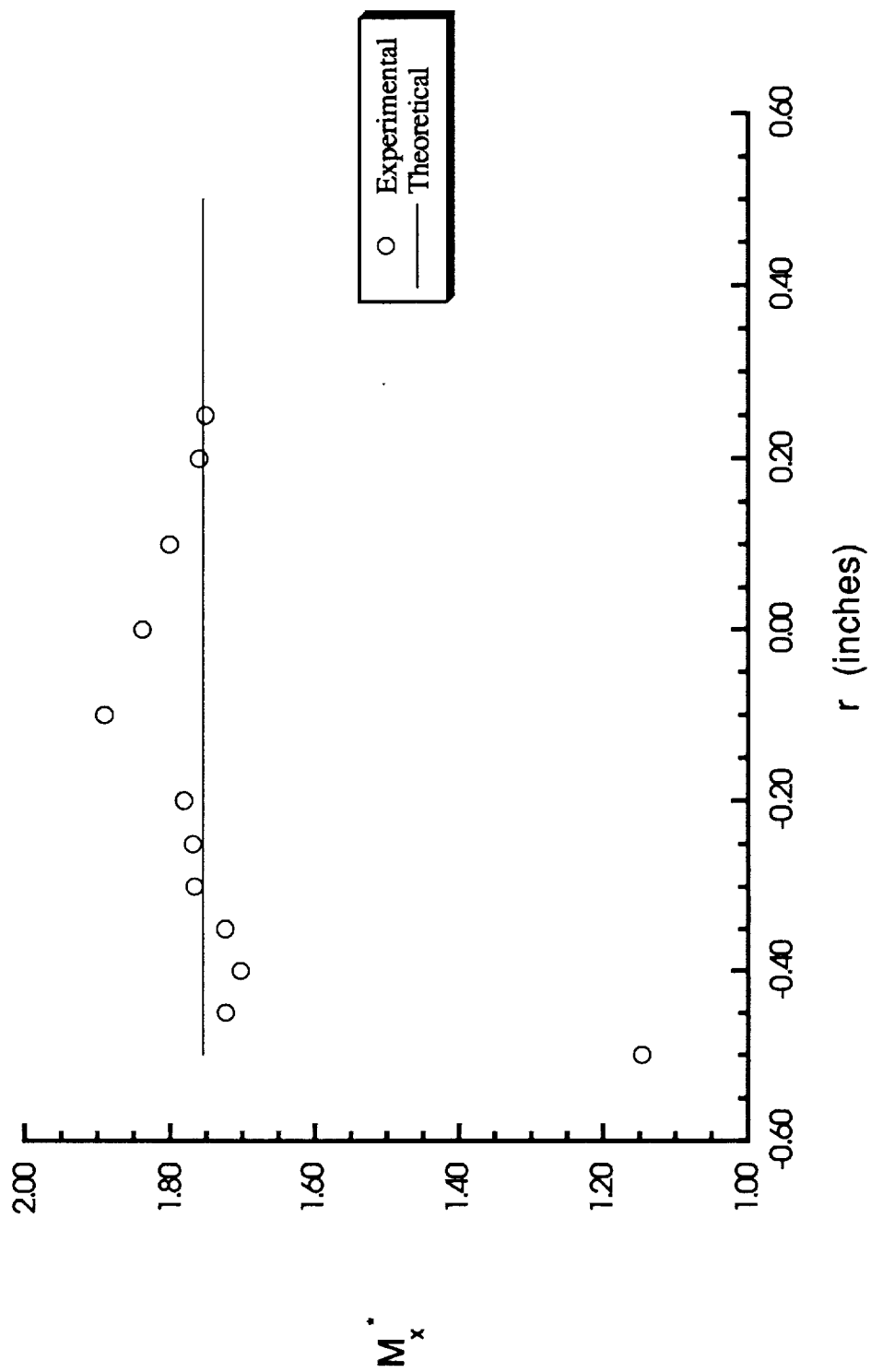


Figure 5.39: Axial Velocity as a Function of Radial Distance for Medium Swirl

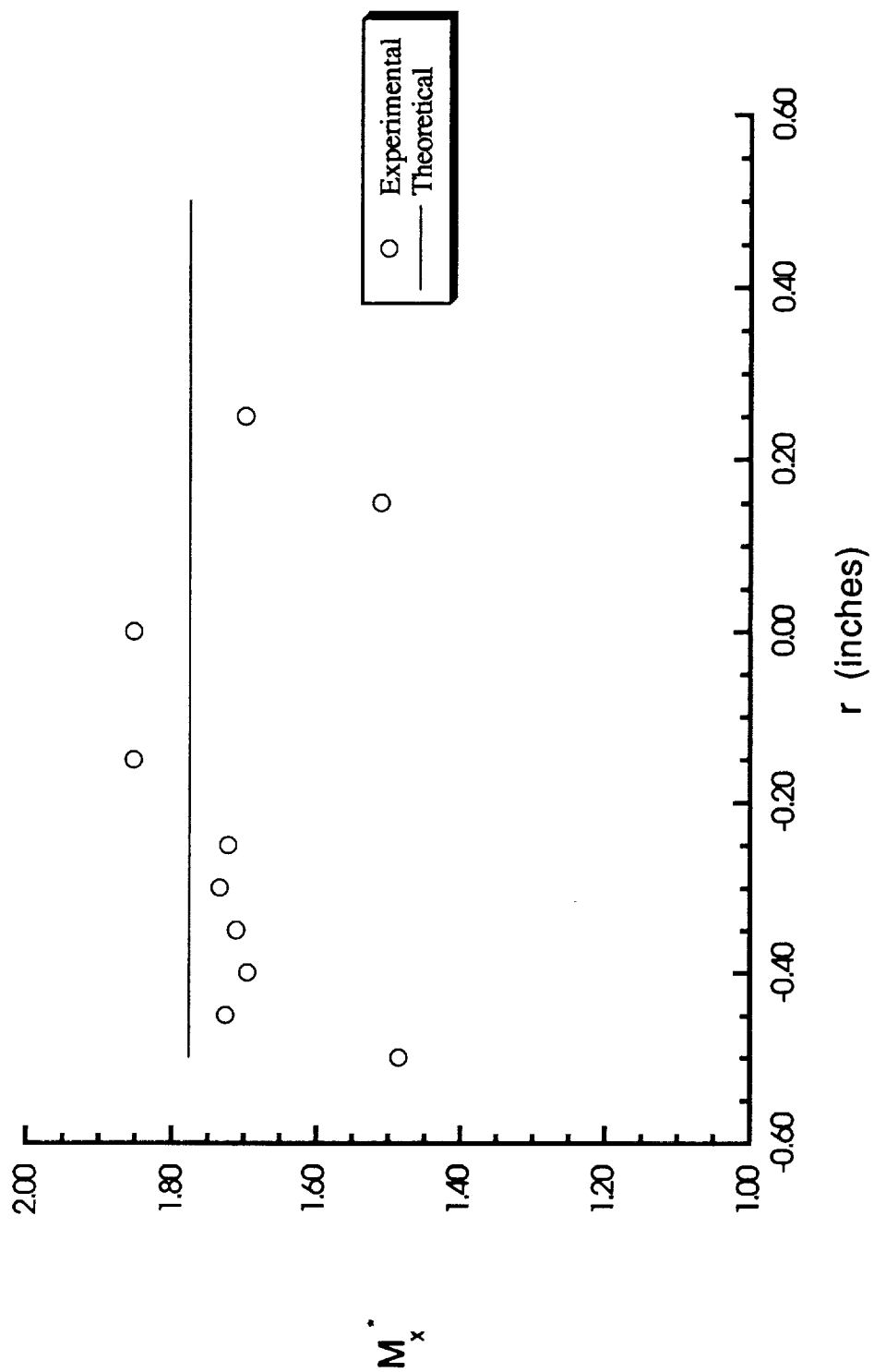


Figure 5.40: Axial Velocity as a Function of Radial Distance for High Swirl

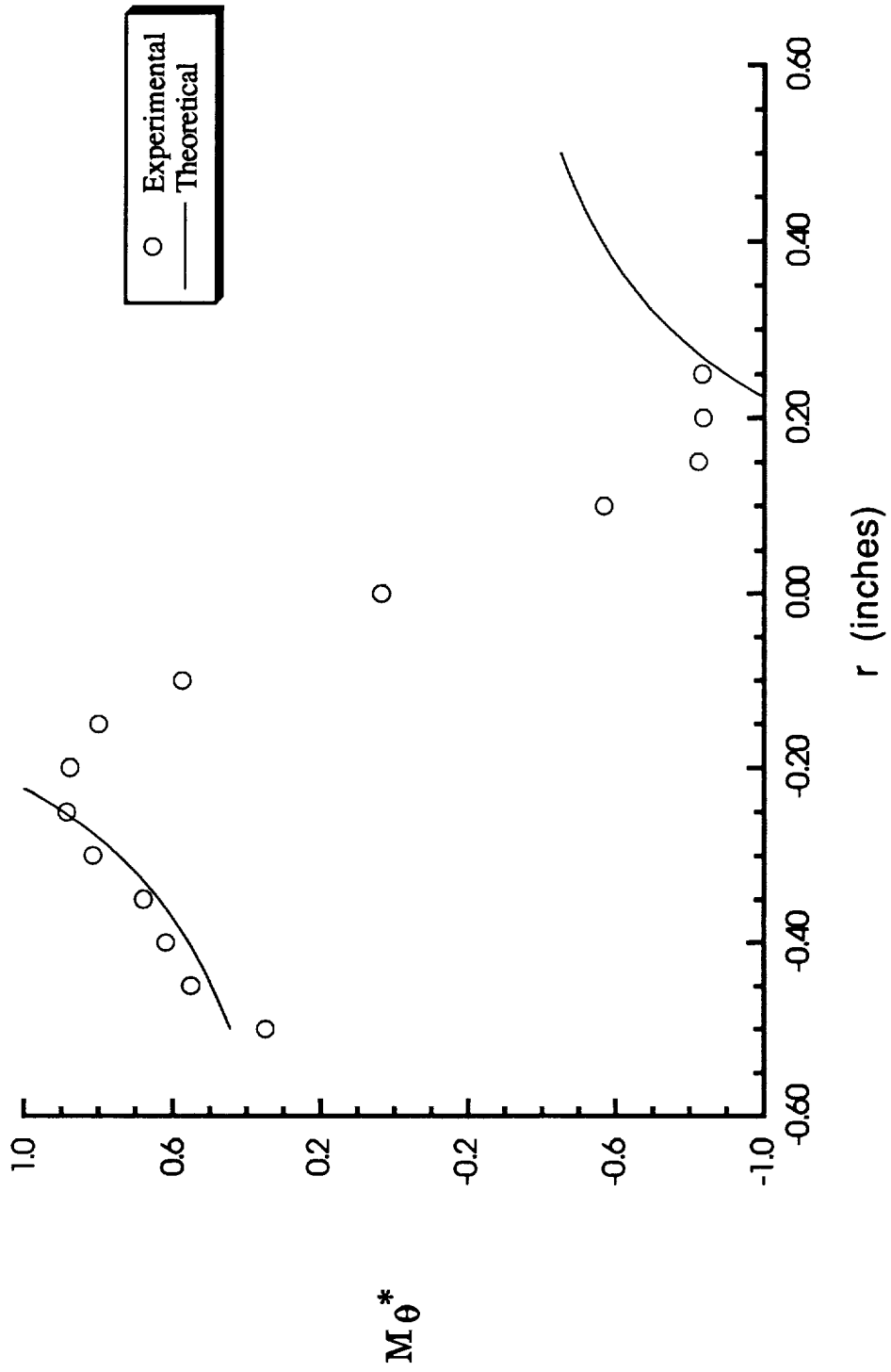


Figure 5.41: Tangential Velocity as a Function of Radial Distance for Low Swirl

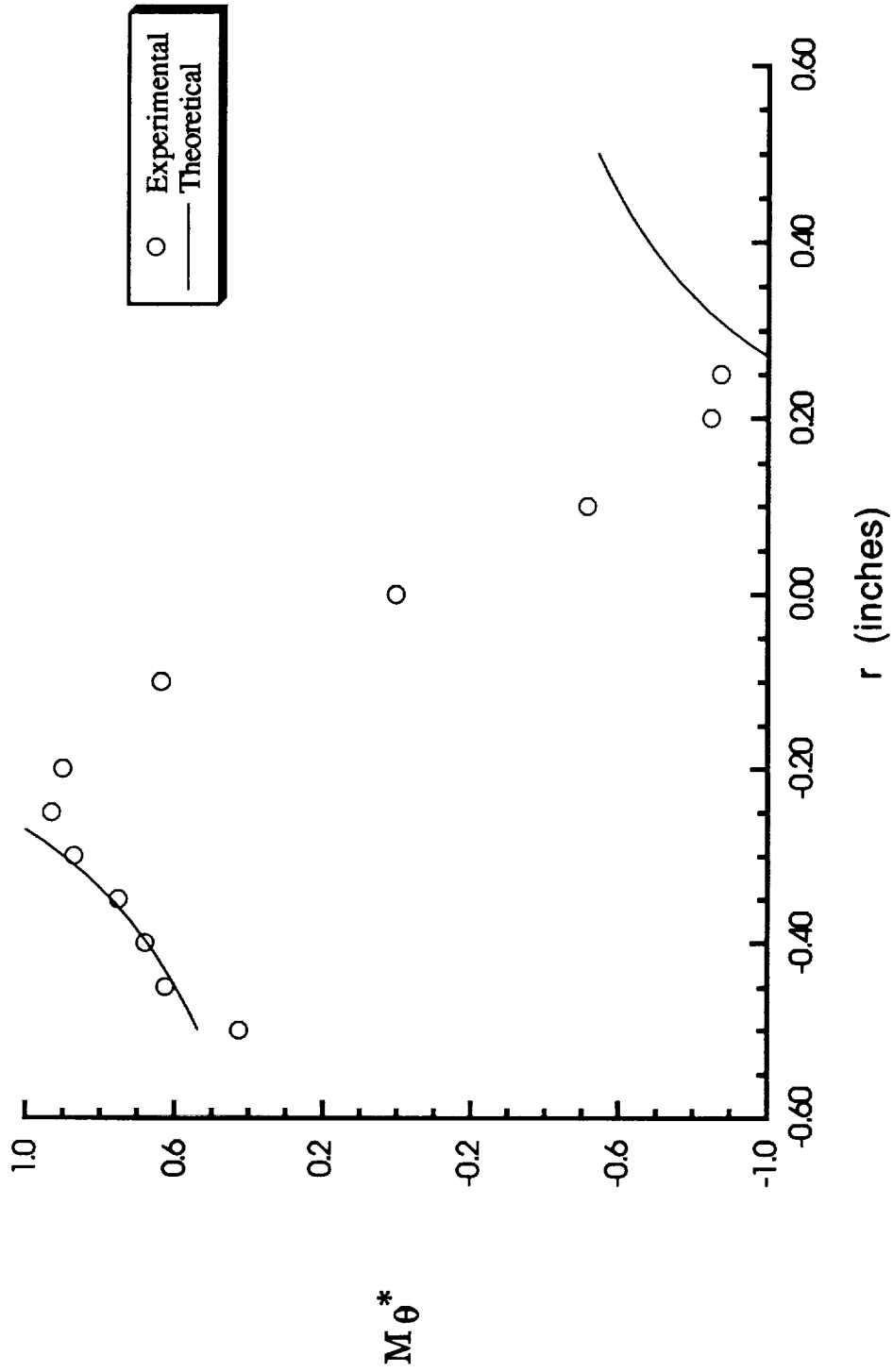


Figure 5.42: Tangential Velocity as a Function of Radial Distance for Medium Swirl

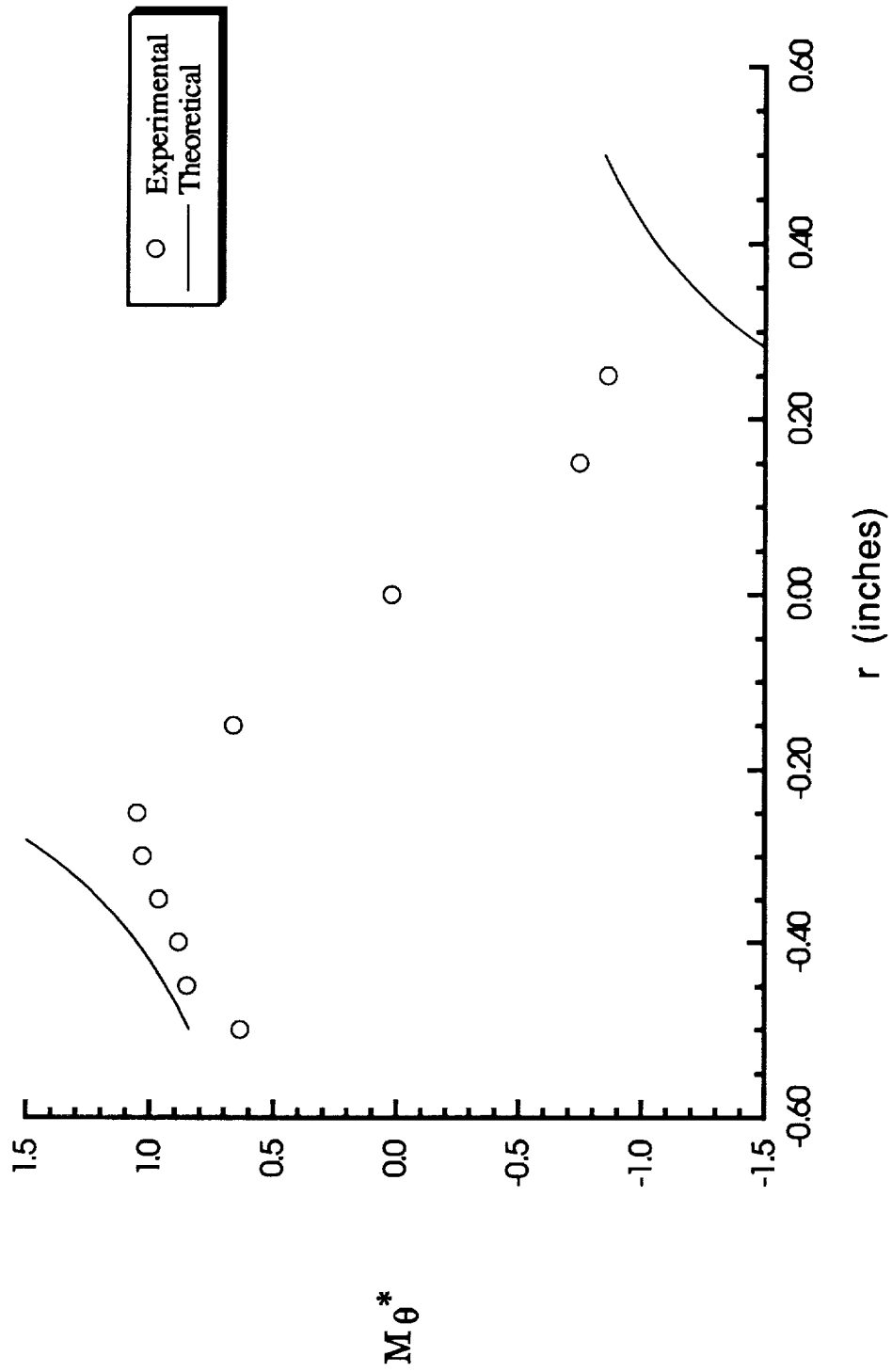


Figure 5.43: Tangential Velocity as a Function of Radial Distance for High Swirl

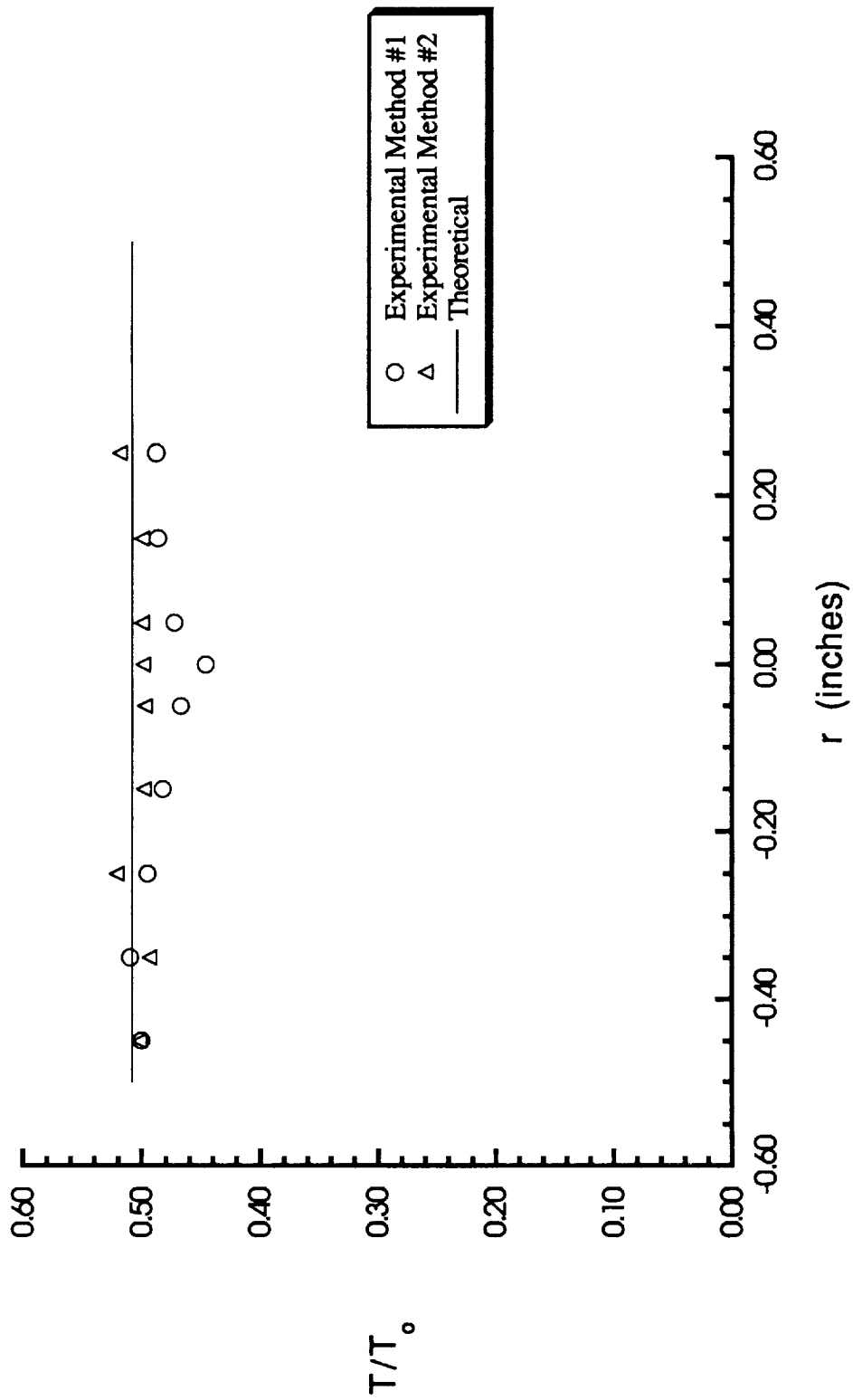


Figure 5.44: Static Temperature as a Function of Radial Distance for No Swirl

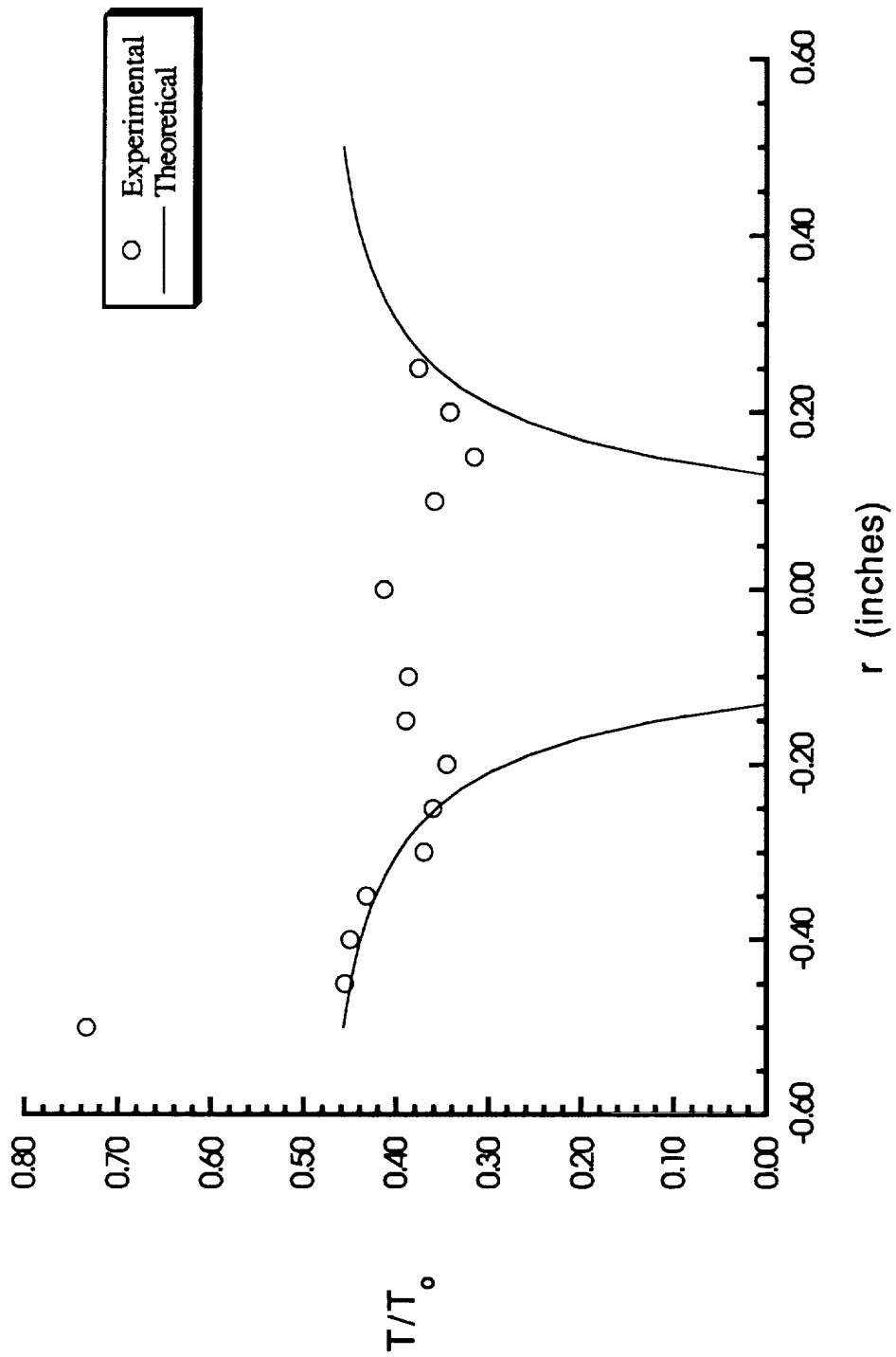


Figure 5.45: Static Temperature as a Function of Radial Distance for Low Swirl

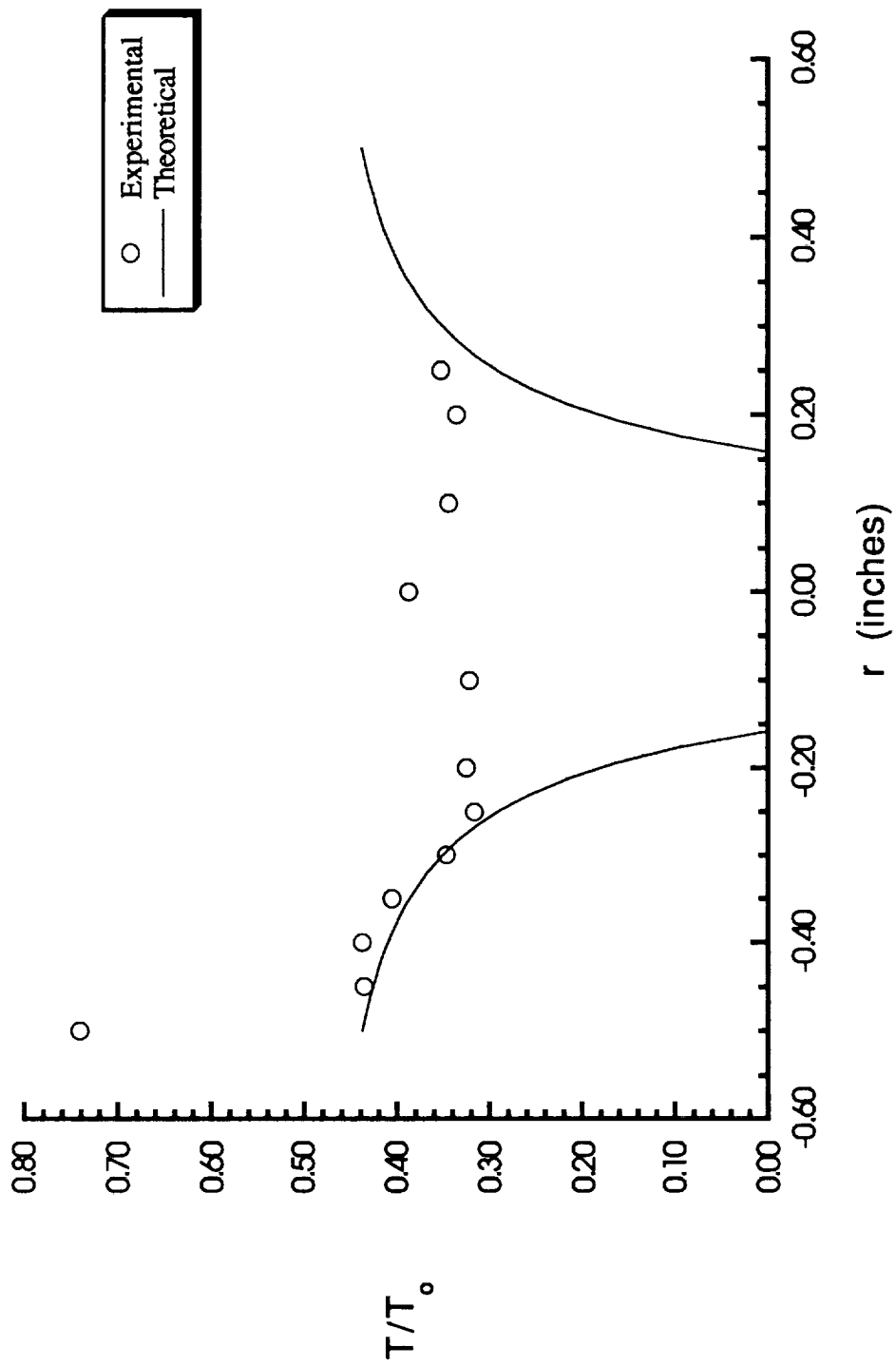


Figure 5.46: Static Temperature as a Function of Radial Distance for Medium Swirl

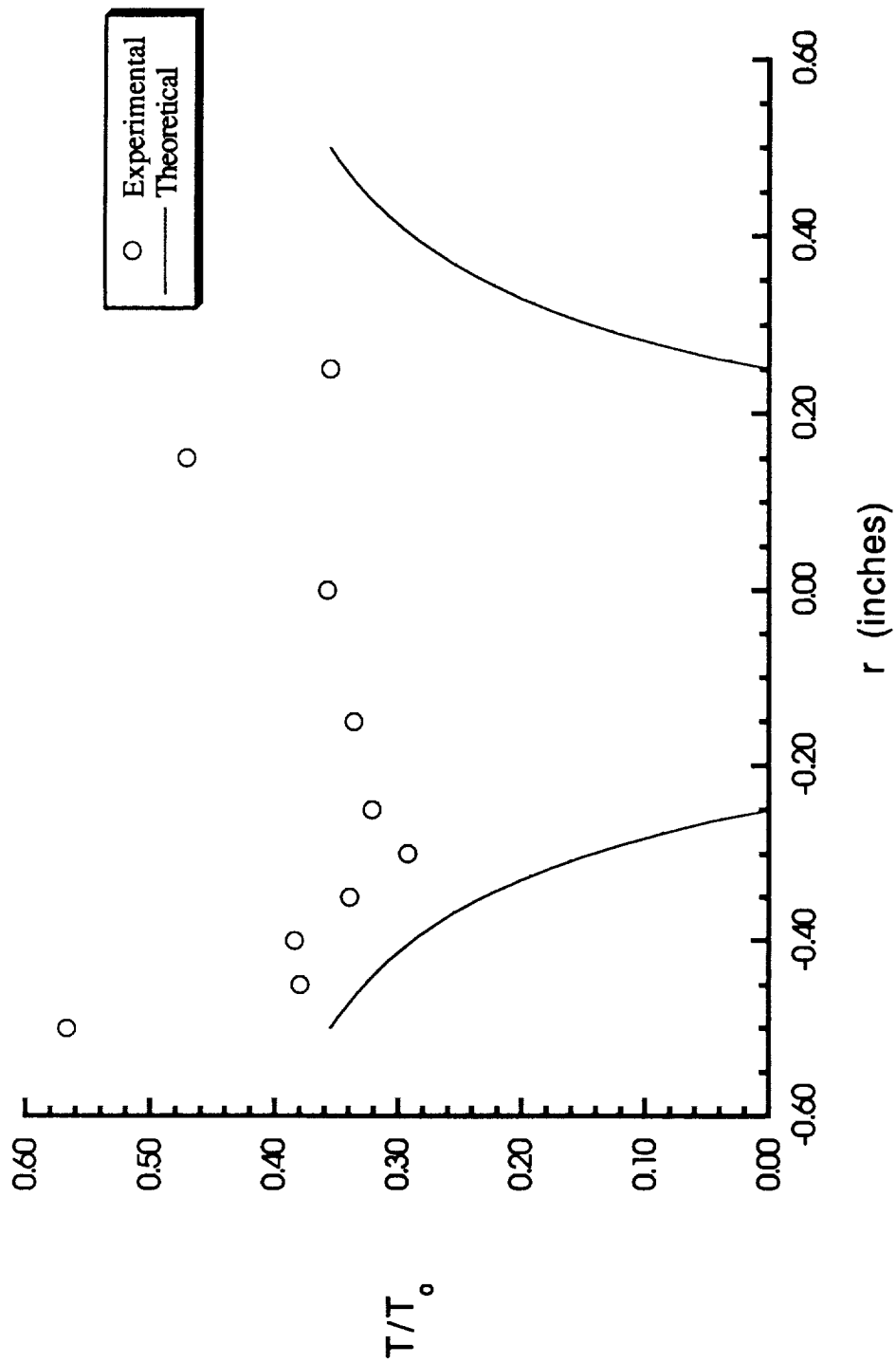


Figure 5.47: Static Temperature as a Function of Radial Distance for High Swirl

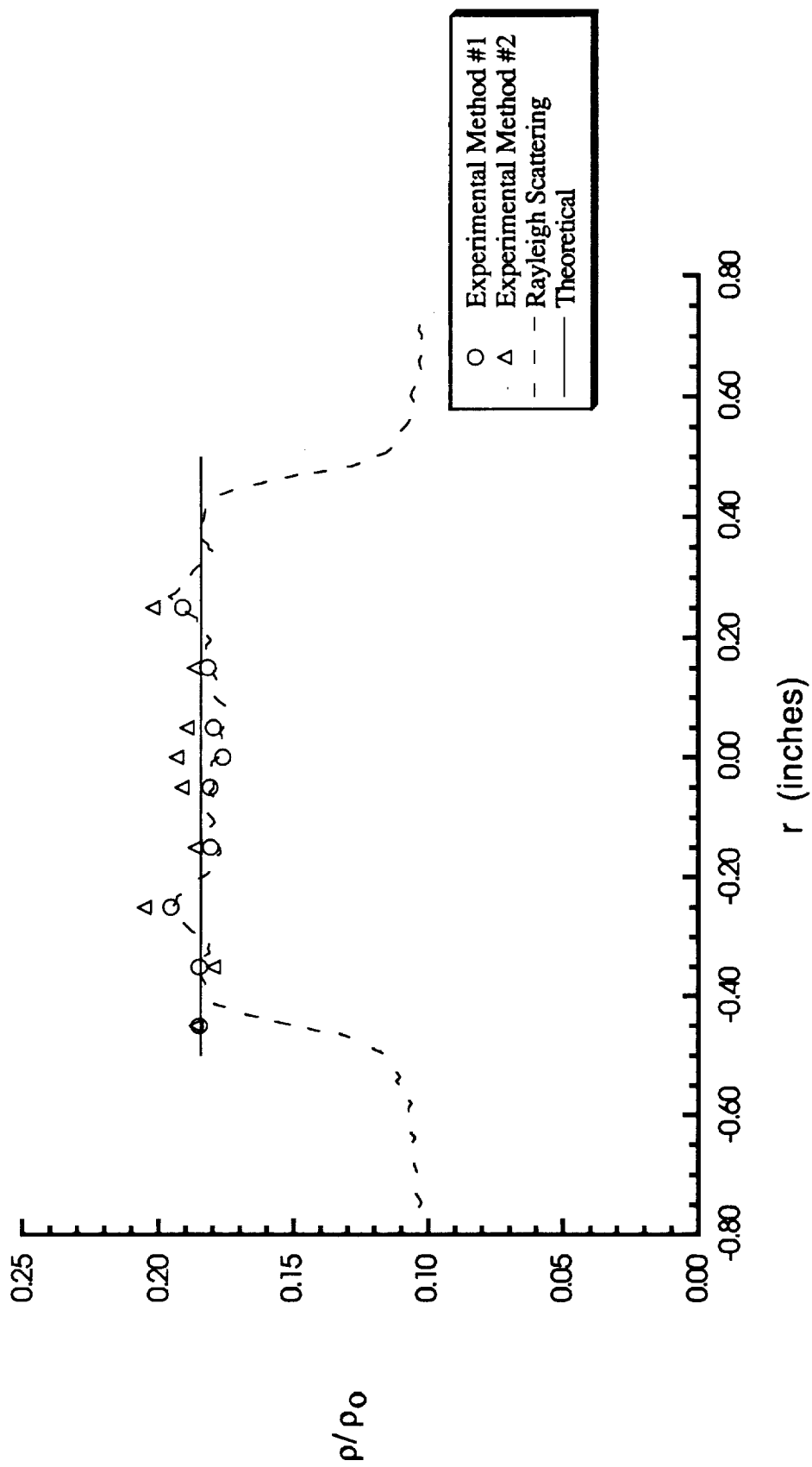


Figure 5.48: Static Density as a Function of Radial Distance for No Swirl

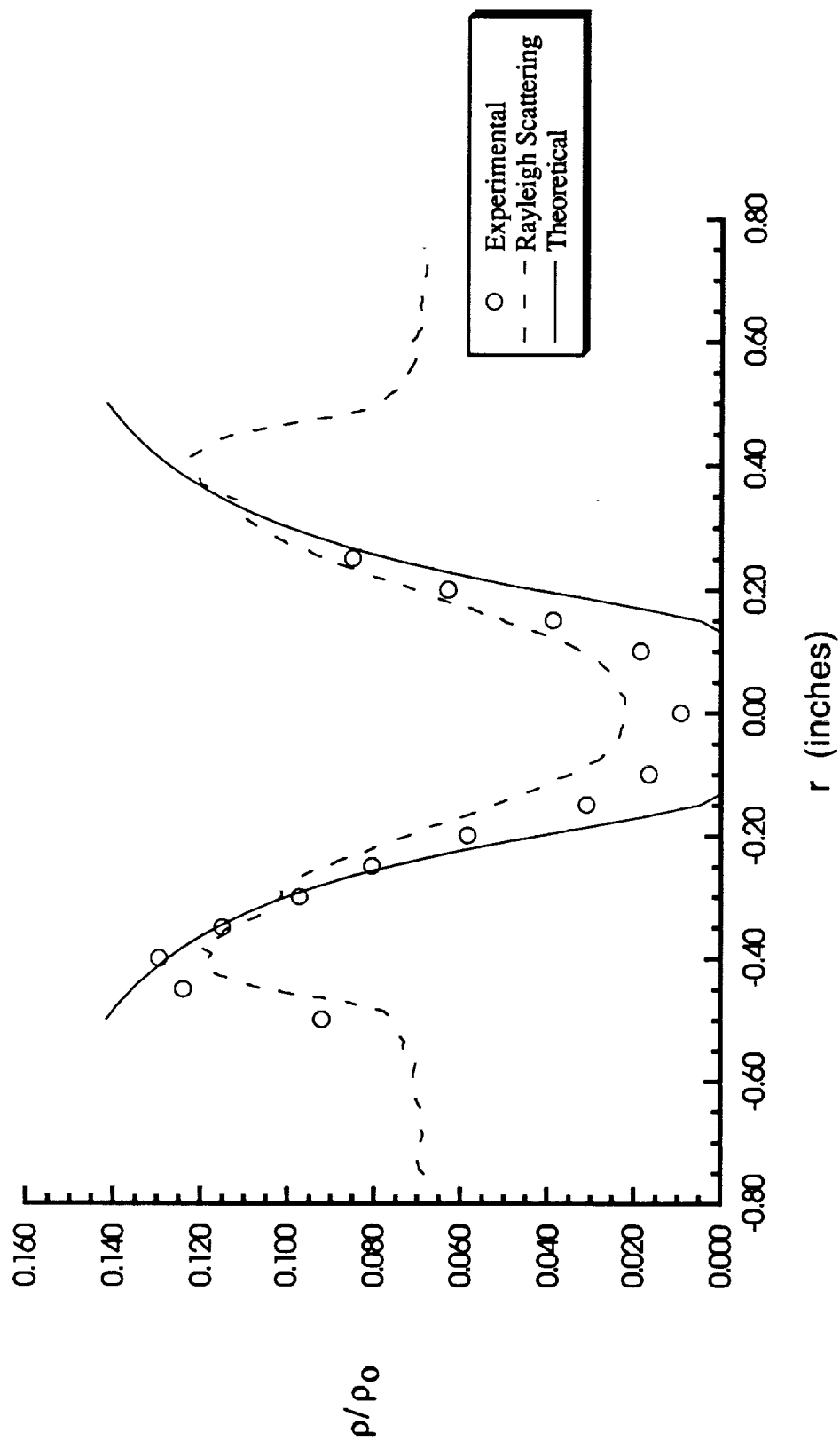


Figure 5.49: Static Density as a Function of Radial Distance for Low Swirl

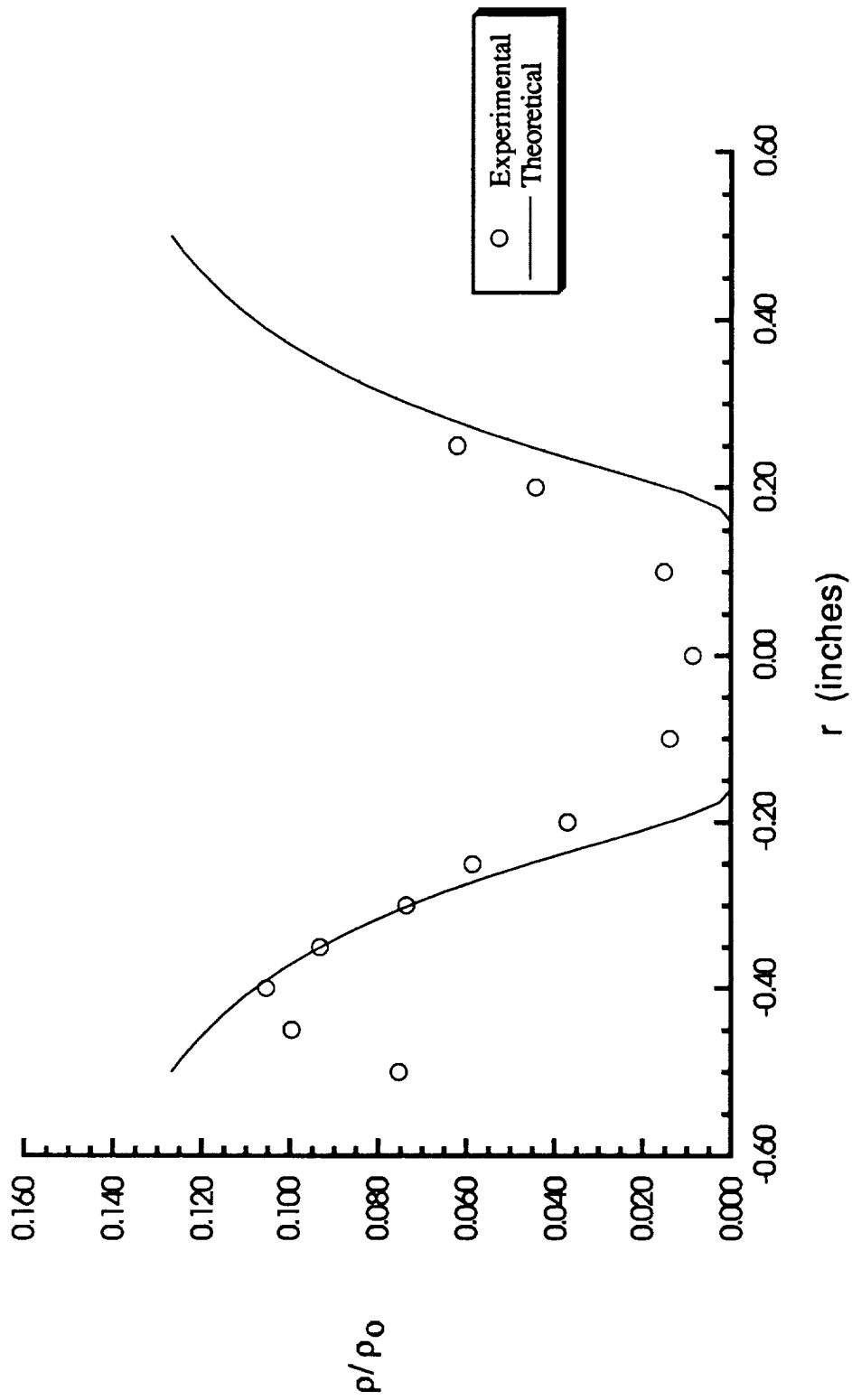


Figure 5.50: Static Density as a Function of Radial Distance for Medium Swirl

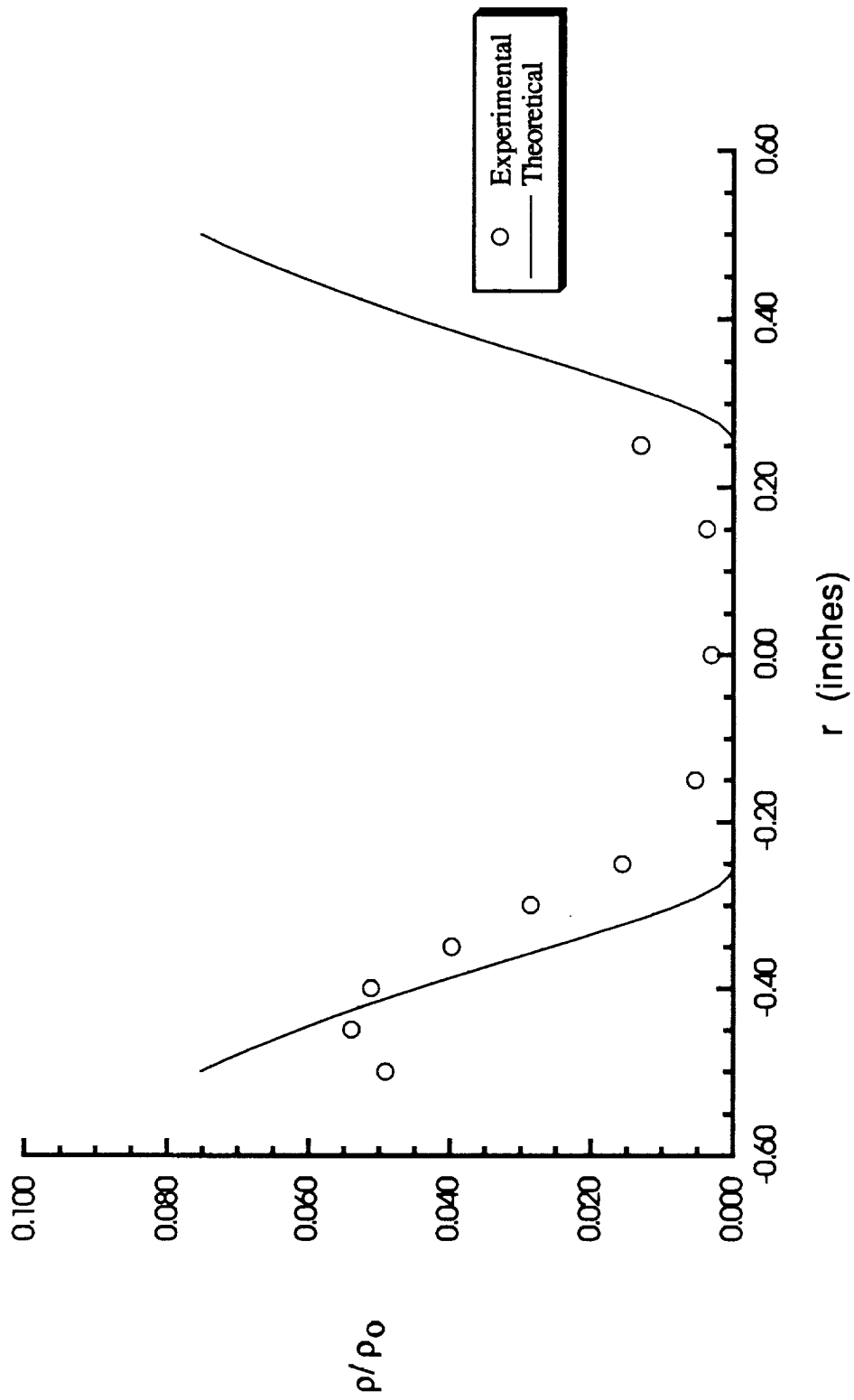


Figure 5.51: Static Density as a Function of Radial Distance for High Swirl

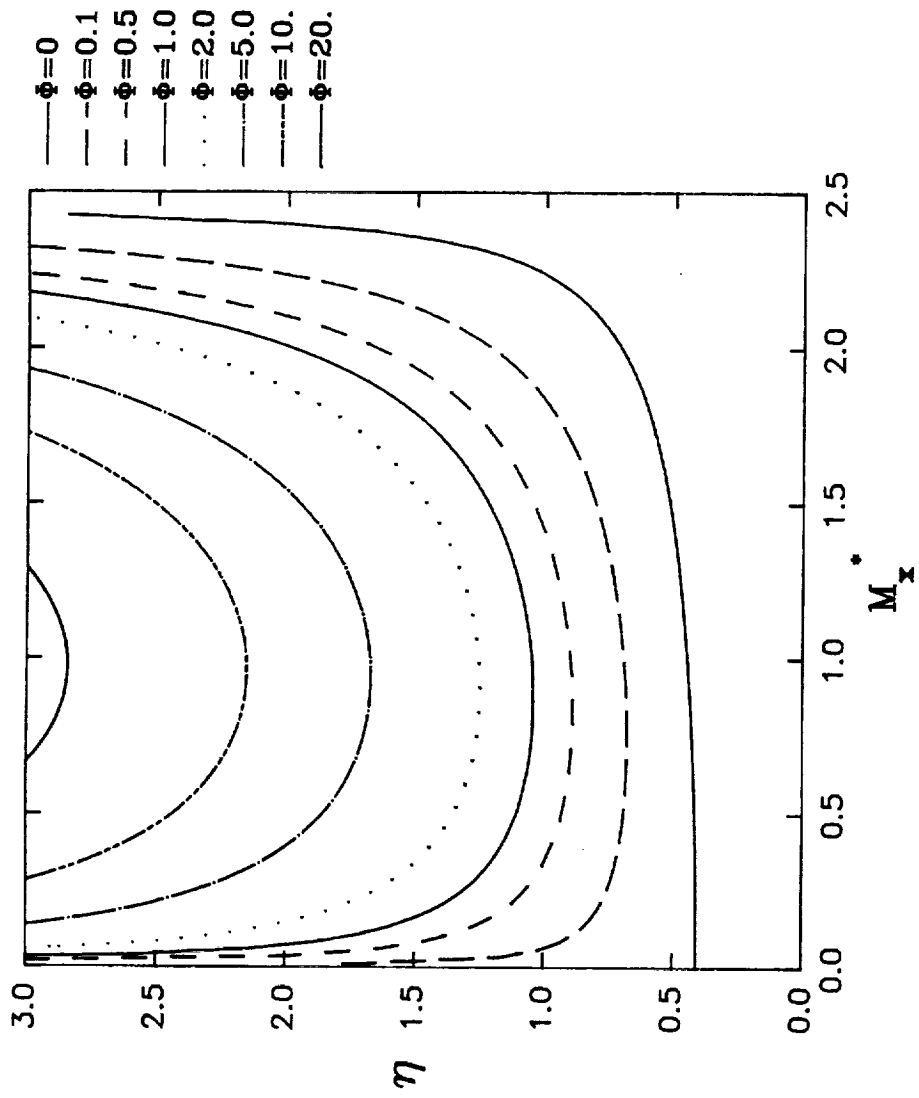


Figure A.1: Calculated Vortex Streamtube Diameter as a Function of Axial Velocity

	No Swirl	Low Swirl	Medium Swirl	High Swirl
L (inches)		4.500	3.000	0.750
A_j (inches ²)		1.178	0.785	0.196
r^*		0.224	0.270	0.422
Φ		4.267	2.350	0.372
$M_{x,t}^*$	1.000	0.927	0.903	0.806
$M_{x,e}^*$	1.717	1.747	1.755	1.777
P_{s1}/P_0	1.000	0.991	0.986	0.967
$P_{w,t}/P_0$	0.528	0.438	0.395	0.227
$P_{w,e}/P_0$	0.094	0.065	0.056	0.027
$(V/U)_{w,e}$	0	0.256	0.307	0.475

Table 3.1: Geometric and Calculated Flow Parameters of the Nozzle for the Investigated Swirl Cases

	No Swirl	Low Swirl	Medium Swirl	High Swirl
Total Pressure (lbs/in ²)	145	210	250	470
Total Temperature (°R)	520	520	520	520

Table 5.1: Average Total Property Values at the Plenum Chamber